UNIVERSITEIT VAN PRETORIA
UNIVERSITY OF PRETORIA
YUNIBESITHI YA PRETORIA

Textures of titaniferous magnetite of the Bushveld Igneous Complex, South Africa

Faculty of Natural and Agricultural Sciences

University of Pretoria

Research project submitted in partial fulfilment of the requirements for the degree of:

MSc (Master of Science)

In

Geology

By: Kyle Lusted

Student Number: 12075991

Supervisor: Dr R.J. Roberts

26 March 2019

DECLARATION OF ORIGINALITY
UNIVERSITY OF PRETORIA

I, the undersigned, declare that:

1. I understand what plagiarism is and am aware of the University's policy in this regard.
2. I declare that this research project is my original work. Where other people's work has been used (from either: a printed source, internet source or any other source), has been properly acknowledged and referenced by Departmental requirements.
3. I have not used work previously produced by another student or any other person to hand in as my own.
4. I have not allowed, and will not allow anyone, to copy my work with the intention of passing it off as his or her own work.

SIGNATURE

……..…….

K. Lusted

12075991

Acknowledgements

I want to acknowledge the help and support I received from my supervisor, Dr R.J. Roberts. He deserves a huge thank you for all his assistance on difficult and new topics, his willingness to assist with solutions to seemingly endless problems and for his support throughout the year. I would also like to thank the Metallurgical Department at the University of Pretoria, for the use of their lab and the support of the lab staff, for their help and time on their equipment and access to their labs. A special thank you must also go to Dr R Cromarty for his willingness to assist in the making of the polished sections used in this project. I would also like to thank my family for their love, support and patience throughout the year, always pushing me to achieve more. I want to thank the Geology Department of the University of Pretoria for the opportunity to take part in this experience and for always offering advice and new ideas. Lastly, I would like to thank Francois Lötter and Nicholas Fraser for their support, camaraderie and scintillating conversations throughout the year, you boys made it a year to remember.

ABSTRACT

Magnetite is a major constituent of the Upper Zone of the Bushveld Complex in South Africa. Magnetite occurs first as an intercumulus mineral, then as a cumulus mineral, then as massive monomineralic layers within the succession of gabbroic rocks. This study focuses on the textural intergrowths with the magnetite of the Upper Zone. Intergrowths of ilmenite occur within magnetite and exist between two extremes, namely the cloth microtexture and the trellis microtexture (with a "sandwich" variant). The cloth intergrowth is also characteristic of the ulvöspinel exsolutions in the magnetite. These lamellae usually lie on {100}, with inter-lamellar magnetite-rich blocks. The exsolution microstructure only develops on a small scale, due to the slow rate of the kinetic processes involved in unmixing at the solvus temperature. Within the ulvöspinel cloth microtexture, it is the coarse {100} lamellae pattern which gives the grain the appearance of cloth. Magnetite appears as extremely small blocks between the exsolved lamellae of ulvöspinel. The {100} lamellae of the cloth microtexture generated by exsolution of ulvöspinel occur at a temperature below the magnetite-ulvöspinel solvus. The ulvöspinel completely transforms into ilmenite micro-lamellae through in situ oxidation. Martitization occurs under moderate-temperature, hydrothermal oxidation, resulting in a volume change when hematite replaces magnetite. The calculated volume change increase is around 1.7%; this volume change results in expansion fractures throughout the replaced grains. The magnetite grains are preferentially martitized along grain boundaries and octahedral planes {111} leaving unaltered cores except in few places where it is martitized throughout the grain. Possible processes involved in the formation of the various textures include: (1) Pulses of Fe-Ti rich magmas occur, injecting large amounts of liquid into the Upper Zone. Dense immiscible droplets form and settle out of suspension, accumulating and forming stratified layers. The initial temperature of the liquid is approximately 1150ºC. (2) Upon cooling, titaniferous-magnetite precipitation occurs at around 865ºC, with low oxygen fugacity across the chamber. At this stage, ilmenite is not abundant, due to the presence of Ti as a component of ulvöspinel at high temperatures, rather than ilmenite. (3) At some point during cooling of the solid solution, spinodal decomposition occurs. This starts to produce ulvöspinel lamellae within magnetite grains. At the same time, the stratified layers begin to oxidise, forming ilmenite as a product of ulvöspinel decomposition. (4) External granular diffusion results in ilmenite constituents, diffusing across the grain boundary. When the rates of diffusion decrease, the ilmenite cannot leave the titaniferous-magnetite grain and exsolve. Ilmenite is dependent on the ulvöspinel content, which in turn is dependent on the temperature and oxygen fugacity during cooling. This would indicate why some polished sections showed ilmenite exsolution whilst others do not. (5) The layers cool to a point where spinodal decomposition is no longer favoured and the system shifts from cloth-texture exsolution to trellis-exsolution. The ilmenite component begins to form thin, multi-directional lenses often surrounded by box structures. (6) During oxidation, some magnetite subjected to martitization, is subsequently replaced by martite. The replacement involves an expansion and fracturing of martitized grains. During expansion, syntaxial veins form along grain boundaries, subsequently filled by surrounding Fe-Ti liquid. Depending on the growth rate of the crystals within the vein, either blocky syntaxial veins or blade-like syntaxial veins form. (7) During continued cooling, annealing of euhedral magnetite grains occurs. The annealing process runs concurrently with other processes occurring within the magnetite layers.

Table of Contents

List of Figures

List of Tables

Chapter 1: Introduction

One of the most studied, yet least understood topics of studies are monomineralic oxide layers found within layered mafic intrusions. The focus of many studies has been around the possible formational conditions that produce these monomineralic layers. Possibly the most famous of these layered mafic intrusions is the Bushveld Igneous Complex, located in the northeastern portion of South Africa. The vastness of the Bushveld Igneous Complex, encompassing some of the world's largest economic deposits, attracts many inquisitive researchers. Many experimental studies aimed to estimate formational conditions such as oxygen fugacity, temperature, pressure and starting compositions. However, an area of oxide study that has lacked attention is the various textures that occur within these layers. Certain textures such as exsolution features frequently occur within the various oxide layers of the Bushveld Igneous Complex.

The various compositions of Fe-Ti oxides are divided into three major solid solution series, namely; the titanomagnetite series (solid solution between magnetite and ulvöspinel), the titanohematite series (solid solution between hematite and ilmenite), and the 'ferropseudobrookite'-pseudobrookite series (Pearce et al., 2010). The Fe-Ti oxides of the Bushveld Igneous Complex form part of the titanomagnetite series with a minor component of the titanohematite series (Von Gruenewaldt et al., 1985). Although most of the magnetite occurs as stratified layers, some also occur as plugs or pipes depending on the viewpoint of the researcher. The Fe-Ti oxides concentrated as magnetite plugs occur in both the Main Zone and Upper Zone of the Bushveld Igneous Complex (Scoon and Mitchell, 2012; Molyneux, 1974; Von Gruenewaldt, 1973). Geological relationships of Ti-magnetitite layers with their host rocks suggest that the layers form an integral part of the Bushveld Igneous Complex itself (Reynolds, 1985a).

The analytical methods used in this study are largely qualitative within minor quantitative techniques. Reflected light microscopy provided photomicrographs and preliminary descriptions of each sample, while the Scanning Electron Microscope (SEM) provided scaled images, point analyses as well as an insight into the various textures and mineral relationships occurring within each sample.

The purpose of this study is to describe the various sampled oxide layers and plug textures, to compare the textures identified with other layers of magnetite and to compare the textures with those found in the literature. Several exsolution textures occur, each with distinctly different mineralogy to other exsolution textures within the intrusion. Identified within literature are various exsolution textures native to iron oxides. These textures include the trellis- and cloth-texture exsolutions, seen within this dissertation. These lamellae usually lie on {100}, with inter-lamellar magnetite-rich blocks (Price, 1980). The exsolution microstructure only develops on a small scale, due to the slow rate of the kinetic processes involved in unmixing at the solvus temperature. Within the ulvöspinel cloth microtexture, it is the coarse {100} lamellae pattern which gives the grain the appearance of cloth (Ramdohr, 1953). The {111} ilmenite lamellae form a distinctly thicker network with regular multidirectional growth. When an aluminium-rich spinel is present, like that found within this study, these ilmenite lamellae are dotted with spinel micro-crystals. A radiating, needle-like texture appeared within certain sections. Since there is no existing literature that explains this

texture, comparisons between other minerals displaying similar crystal morphologies may provide clues to their formation. An overall formational model aims to compile possible stages in the formation of each of the structures seen in this study.

Chapter 2: Literature Review

Bushveld Igneous Complex

The Bushveld Igneous Complex (BIC) is the world's largest layered mafic intrusion, covering a total area of approximately 65 000 km^2 (Cawthorn & Webb, 2001; Tegner et al., 2006). The emplacement of the BIC occurred at approximately 2060 Ma (Buick et al., 2001; Tegner et al., 2006). According to Clarke et al. (2009), the BIC intrudes into the sedimentary rocks of the Transvaal Supergroup. The BIC, situated within the northern section of South Africa, outcrops as three major limbs, namely, the western, northern and eastern limbs as seen in Figure 1 below. The stratigraphy varies across all three limbs; however, the eastern and western limbs show the most comprehensive set of stratigraphic units, even with lateral variations (Cawthorn & Webb, 2001).

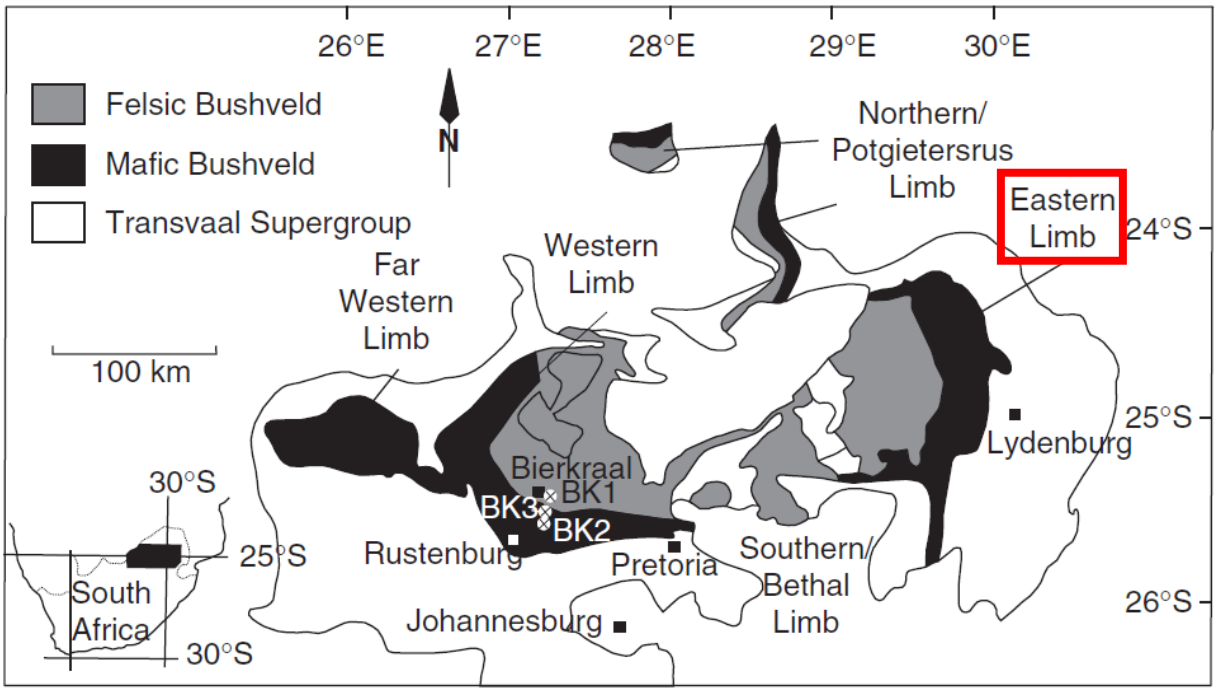

Figure 1. Image showing the layout of the Bushveld Igneous Complex, as well as the various limbs constituting the complex. The focus of this dissertation is on the eastern limb, highlighted by the red box. Tegner et al (2006) – modified after Lundgaard et al (2006).

Stratigraphic Units and Relationships

The BIC is composed of several groups and suites, namely, the Rooiberg Group, the Lebowa Granite Suite, the Rashoop Granophyre Suite and the Rustenburg Layered Suite. Systematically subdivided into five distinct zones, the Rustenburg Layered Suite (RLS) forms the largest portion of the BIC. These zones are, in order of ascending stratigraphic height, the Marginal Zone, the Lower Zone, the Critical Zone, the Main Zone and the Upper Zone as seen in Figure 2 below. These zones are a series of ultramafic to mafic intrusions subdivided by their chemical, isotopic and mineralogical differences (Cawthorn & Ashwal, 2009). The Rooiberg Group, although part of the Transvaal Supergroup, is petrogenetically associated with rocks of the BIC (VanTongeren et al., 2016; VanTongeren et al., 2010). Isotopic ages of the Rooiberg Group rocks, ranging from approximately 2061 ± 2 Ma to 2052 ± 48 Ma, suggest that the formational events of the two units (RLS and the Rooiberg Group) overlapped (Mathez & VanTongeren, 2013; Walraven, 1997).

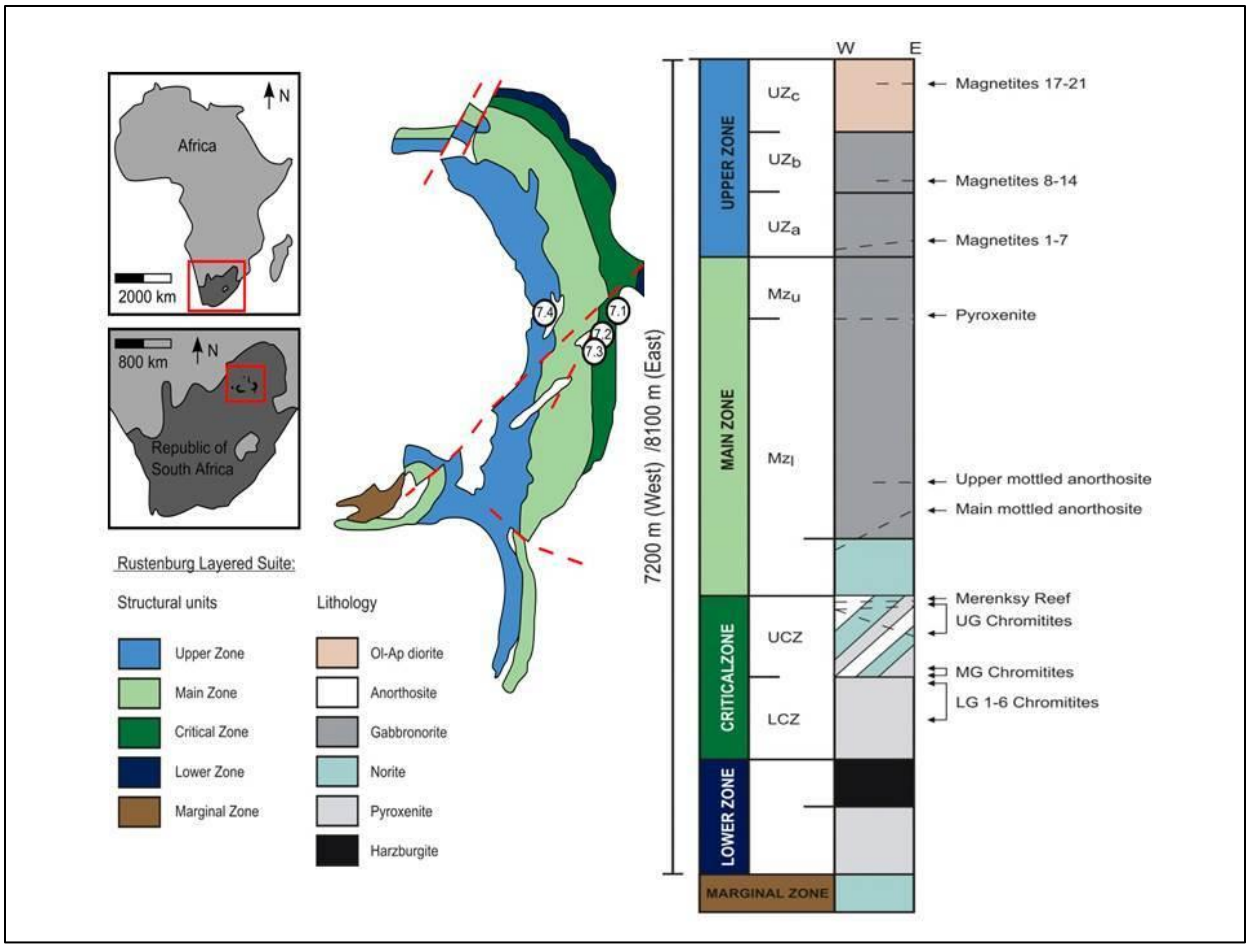

Figure 2. Image showing a simplified map of the eastern limb of the Bushveld Igneous Complex, as well as a simplified stratigraphic column. The stratigraphic column is subdivided into the various zones. The Upper Zone is marked with various magnetite layers at different points within the stratigraphy. Voordouw et al. (2009).

Rustenburg Layered Suite

The classification of the RLS is dependent on the first appearance of specific minerals marking subdivisions within the suite (Cawthorn & Ashwal, 2009). The first appearance of cumulus olivine and orthopyroxene identifies the Lower Zone. Plagioclase, orthopyroxene and chromite appear within the Critical Zone. The first appearance of Ca-rich and Ca-poor pyroxene, as well as plagioclase, classifies the Main Zone, whereas the first appearance of cumulus olivine, plagioclase, magnetite, pyroxene and apatite, characterises the Upper Zone (Cawthorn & Ashwal, 2009; Atkins, 1969).

According to Cawthorn et al. (2006), the Marginal Zone is the lowest most stratigraphic unit of the RLS with a thickness that ranges from 0-800m. The Marginal Zone consists of medium-grained norites with variations in mineral proportions of quartz, hornblende, biotite and clinopyroxene (Cawthorn & Walraven, 1998; Cawthorn et al., 2006). According to Cawthorn et al. (2006), the Marginal Zone represents a rapid crystallisation of differentiated and contaminated magmas that are variably voluminous and intrusive.

The Lower Zone, which overlies the Marginal Zone, ranges in thickness from 0-1300m (Cawthorn et al., 2006). The distribution and continuity of the BIC floor structure constrain the thickness of the Lower Zone (Maila, 2015; Cawthorn et al., 2006). The Lower Zone comprises layers of harzburgite, pyroxenite and dunite, which are most likely the products of magma addition according to Cawthorn & Walraven (1998).

The Critical Zone overlies the Marginal Zone with a thickness that ranges up to 1500m (Eales & Cawthorn, 1995; Cawthorn & Walraven, 1998). The Critical Zone, subdivided into an upper and lower sub-zone based on mineralogy, hosts world-renowned Platinum Group Element (PGE) deposits. These deposits, situated within the UG2, Platreef and Merensky Reef deposits, help to distinguish layering within the Critical Zone. The Upper Critical Zone, comprised of units of pyroxenite, chromitite, norite and anorthosite, displays more defined layering compared to that of the Lower Critical Zone (Cawthorn & Walraven, 1998).

The Main Zone with a thickness of between 2200-3000m forms a substantial volume of the RLS (Kruger et al., 1987). According to Kruger et al. (1987), the Main Zone's lower boundary is at or near the Merensky Reef of the Critical Zone. However, a definitive boundary is challenging to identify. Extreme layering within the Main Zone, attributed to the addition of fresh magma throughout the emplacement of the RLS, contain varying proportions of clinopyroxene, orthopyroxene and plagioclase (Kruger et al., 1987).

The last stratigraphic unit of the RLS is the Upper Zone. The Upper Zone, with a thickness of approximately 2270m, is characterised by the first appearance of cumulus magnetite. This cumulus magnetite marks the boundary between the Main Zone and Upper Zone. The Upper Zone represents the final crystallisation phase of the RLS. Many theoretical studies such as Tegner et al. (2006) after Kruger et al. (1987) suggested that the Upper Zone formed via a single pulse of magma, whereas others such as Scoon and Mitchell (2012) suggested that a magma recharge event from a homogeneous magma chamber, took place. VanTongeren et al. (2013) suggested multiple injections of magma at the base of the Upper Zone. Figure 3 below shows a relatively detailed stratigraphy of the Upper Zone.

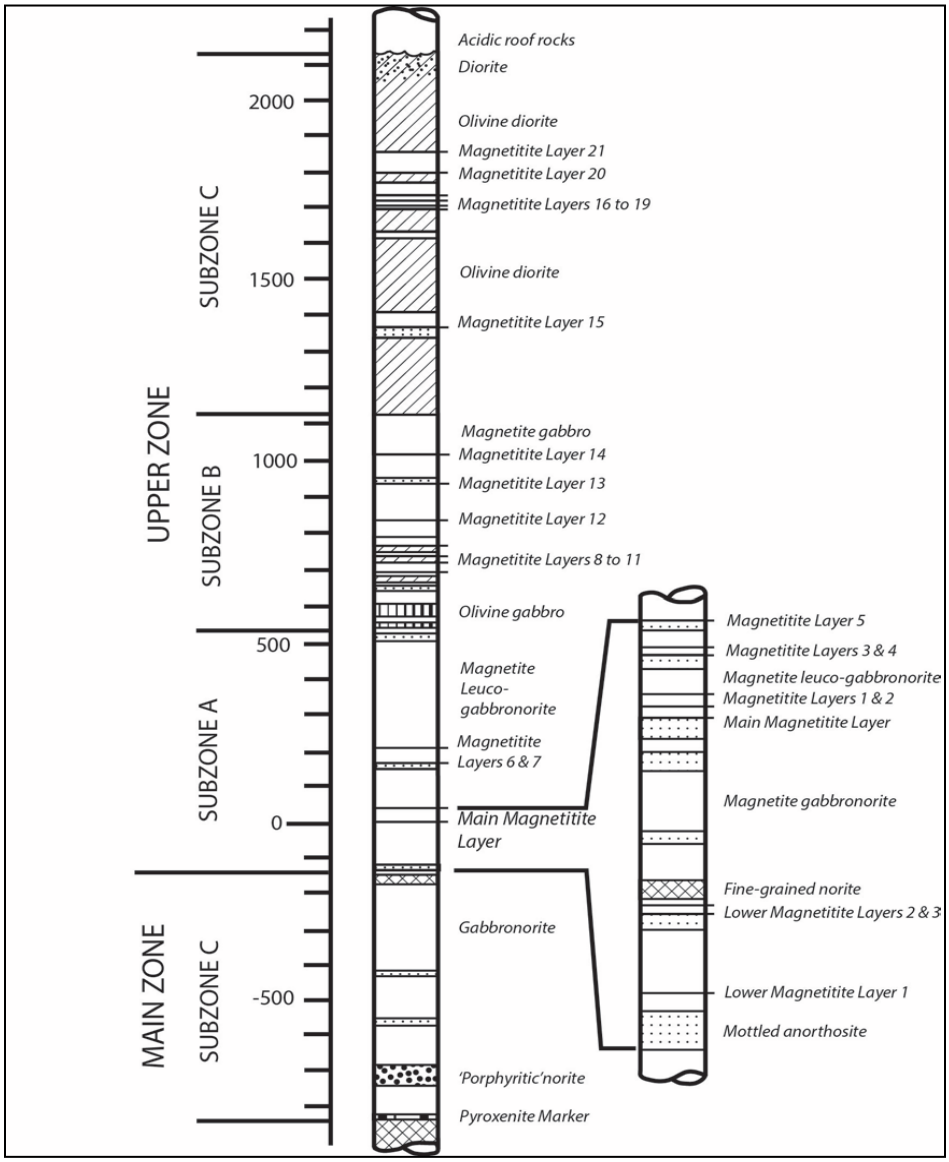

Figure 3. A stratigraphic column of the Upper Zone, showing the various subzones and markers. The first appearance of magnetite characterizes the start of the Upper Zone. Harney and Von Gruenewaldt (1995).

Upper Zone

One of the distinguishable features of the Upper Zone is the occurrence of multiple magnetite layers throughout the sequence. Twenty-five magnetite layers are identifiable within the Upper Zone of the Eastern Limb. Three layers are found below the Main Magnetite Layer, with the remaining layers (Layer 1 to Layer 21) situated above (Harney et al., 1995; Scoon & Mitchell, 2012). The Upper Zone, although dominated by anorthosite, contains varying amounts of apatite, magnetite, pyroxene and olivine (Cawthorn et al., 2006). The top of the Upper Zone sequence suggests an overall increase in ilmenite and decrease in magnetite proportions.

Magnetite layers within the Upper Zone generally show sharp, distinct, lower contacts and gradational upper contacts with the respective surrounding rock types (Reynolds, 1985a; Scoon & Mitchell, 2012). According to Maila (2015) after Tegner et al. (2006), the cumulative thickness of the magnetite layers is approximately 20m with individual layers ranging in thickness from 0.1-10m. The 2m thick Main Magnetite Layer, near the base of the Upper Zone (with a vanadium content of approximately 2%), is economically exploited for the production of alloys (Cawthorn & McCarthy, 1980; Cawthorn et al., 2006).

According to Wager and Brown (1968), the Upper Zone, although the uppermost unit of the RLS, is further subdivided into Subzone-A (UZa), Subzone-B (UZb) and Subzone-C (UZc). The initial appearance of specific cumulus minerals distinguishes each subzone. The initial appearance of magnetite marks the start of UZa; olivine marks the start of UZb and apatite marks the start of UZc (Cawthorn et al., 2009). The appearance of these minerals coincides with a variety of minor, non-cumulus minerals such as biotite, hornblende, ilmenite, alkali-feldspar and quartz (Von Gruenewaldt, 1973; Tegner et al., 2006; Cawthorn & Ashwal, 2009). Although each limb of the BIC differs, the stratigraphy of the Upper Zone, within the Eastern Limb, still shows the variation in rock types with stratigraphic height as seen in Figure 3.

Magnetite

Magnetite, with a general formula of $X^{2+}Y_2{}^{3+}O_4$, is a spinel group mineral. X-sites host divalent cations and Y-sites host trivalent cations. Magnetite forms part of the cubic (isometric) crystal system. X-sites host a range of elements such as (however, not limited to) Fe^{2+}, Mg^{+}, Ca^{2+} and Mn^{2+} (Dare et al., 2012). Y-sites host a range of elements such as (also not limited to) Si^{4+}, Al^{3+}, Ti^{4+}, Cr^{3+}, V^{5+}, and Fe^{3+}. According to Dare et al. (2012), the number of occupancies of different cations in different sites indicates different chemical environments of magnetite formation.

Existing studies by Dare et al. (2012) and Butcher and Merkle (1987) suggests that trace elements indicate the provenance of magnetite as well as formational conditions of associated ore-deposits. However, few studies acknowledge the fact that new generations of the same mineral may alter magnetite during subsequent hydrothermal processes. Previous hydrothermal studies of magnetite failed to address the effect on trace-element geochemistry, which is crucial in understanding the genesis and processes taking place during the formation of magnetite and related ore deposits.

Twenty-five magnetite layers are identifiable within the eastern limb of the BIC. Regarded as amalgamations, some of these numbered layers consist of two or more ore-rich layers separated by a narrow silicate layer. Most of the ore-rich layers are relatively thin, consisting of less than 30cm of titaniferous magnetite. Notable exceptions are the Main Magnetite Layer, as well as Layer 21 (Molyneux, 1970). The magnetitite layers show a remarkable lateral continuity. The MML best displays this lateral continuity, extending 100km in the eastern limb (Cawthorn, 1994; Cawthorn & McCarthy, 1980), 200km in the western limb and 100km in the northern limb (Reynolds, 1985a; Cawthorn & McCarthy, 1980). Throughout the UZ, sulphides are rare but may occur within magnetite layers (Von Gruenewaldt, 1976).

Von Gruenewaldt et al. (1985b) investigated the changes in the magnetite exsolution features within the Upper Zone of the eastern limb of the BIC. Compared to other layered intrusions, the TiO_2 content in the Upper Zone is rather low. Exsolution indicates that the TiO_2-content could have been part of a solid solution within the titaniferous magnetites at high temperatures. The observed textural features in titaniferous-magnetites are a result of two processes: the first is oxidation of the magnetite-ulvöspinel solid solution at temperatures above the magnetite-ulvöspinel solvus resulting in a process similar to exsolution, where most ilmenite exsolved from the titaniferous magnetite. The second, ulvöspinel exsolution is a true exsolution process that is a result of decreased solubility of one component within another as the temperature drops (Von Gruenewaldt et al., 1985b). The changes in the exsolution textures occur as either exsolution above the magnetite-ulvöspinel solvus, or exsolution below the magnetite-ulvöspinel solvus, essentially the backbone of this study.

Magnetite Layers and Plugs

The Main Magnetite Layer (MML) is traceable along strike for up to 100km within the Eastern Limb, with thicknesses averaging 2m in most areas (Scoon & Mitchell, 2012; Willemse, 1969). The Steelpoort River and its tributaries near Roossenekal, within the Eastern Limb of the BIC, exposes the MML at some outcrops (Scoon & Mitchell, 2012). According to Reynolds (1985a), the MML's magnetite is coarsely crystalline due to processes such as annealing and expulsion of interstitial silicate material. Etched into weathered grains are exsolved grains of ulvöspinel and ilmenite, with silvery grains of granular ilmenite often visible (Scoon & Mitchell, 2012).

According to Cawthorn and McCarthy (1980) and Reynolds (1985b), Layer 21 consists of multiple, relatively thin, ore-rich layers separated by narrow partings of olivine-bearing anorthosites. Within the Roossenekal area, Layer 21 is well exposed, and the attractiveness of this layer is its extreme collective thickness in comparison to the other layers in the sequence (Scoon & Mitchell, 2012). Generally, Layer 21 is more than 20m thick and varies from exposure to exposure. The content of V_2O_5 in Layer 21 is also very low (typically less than 0.1%), as may be expected of a magnetite layer located high up in the stratigraphic sequence (Scoon & Mitchell, 2012). The TiO_2 content is typically more than 25%. According to Scoon and Mitchell (2012), the combination of the economic viability of smelting such a Ti-rich ore, the scarcity of vanadium, and difficulties with extracting the Ti-oxide from the slag, has prevented the economic exploitation of this layer.

According to Harney and Von Gruenewaldt (1995) and Von Gruenewaldt (1973), mafic to ultramafic pegmatites are standard features in all zones of the RLS, with magnetite-rich, pipe-like pegmatites being most common in the Upper Zone. These bodies, located in the field, occur as large heaps of titaniferous-magnetite, a few tens of meters in diameter (Harney & Von Gruenewaldt, 1995). However, due to the extensive coverage of magnetite rubble, the immediate country rocks of these magnetite pipes are not well exposed. According to Scoon and Mitchell (1994), Willemse (1969) and Molyneux (1970), the discordant titaniferous-magnetite plugs reported in the Upper Zone are prominent within the Roossenekal area. Scoon and Mitchell (2012) described these titaniferous magnetite pipes as Fe-Ti oxide pegmatites. They did this in an attempt to emphasise the spatial and genetic relationships with the discordant bodies located lower in the RLS. According to Willemse (1969), the pipes revealed similar compositional trends to the magnetite layers, in that they become increasingly depleted in V_2O_5 and enriched in TiO_2 with increasing stratigraphic height. The vertical extents of these plugs and pipes are not well studied. Therefore, any field relationships involving these plug structures and lower or higher layers of magnetite within the Upper Zone sequence are unknown.

Chapter 3: Methodology

Sampling

Samples used in this study were taken from several locations within the eastern limb of the BIC, South Africa. The sampled material consists of six different samples taken either from layers or from a magnetite plug. The material was collected using a sledgehammer and sample bags. Samples collected include two Main Magnetite Layer samples (MML1 and MML2), a Layer 8 sample (UZ8/17), a Layer 21 sample from north of the Steelpoort Fault (UZ21) and a Layer 21 sample taken from south of the Steelpoort Fault (UZ21B) and a sample taken from a Magnetite Plug (MP1). The MML samples were taken from the Magnet Heights Dam area. The UZ21 sample was taken from an outcrop within Magnet Heights itself. The MP1 sample was taken from a quarry area south of Roossenekal. The UZ8/17 sample was taken along the dust-road near Luipershoek. The Layer 21 sample (UZ21B) was taken from a neighbouring farm of Bonamanzi Lodge and Conference Centre, situated along the Steelpoort River. The selected samples used in this study, were chosen due to accessibility, since most locations are near to or along access roads.

Figure 4. A Google Earth image showing the sample locations of both the UZ8/17 and the UZ21(B) samples. The samples are taken from the Luipershoek area near the farm of Bonamanzi Lodge.

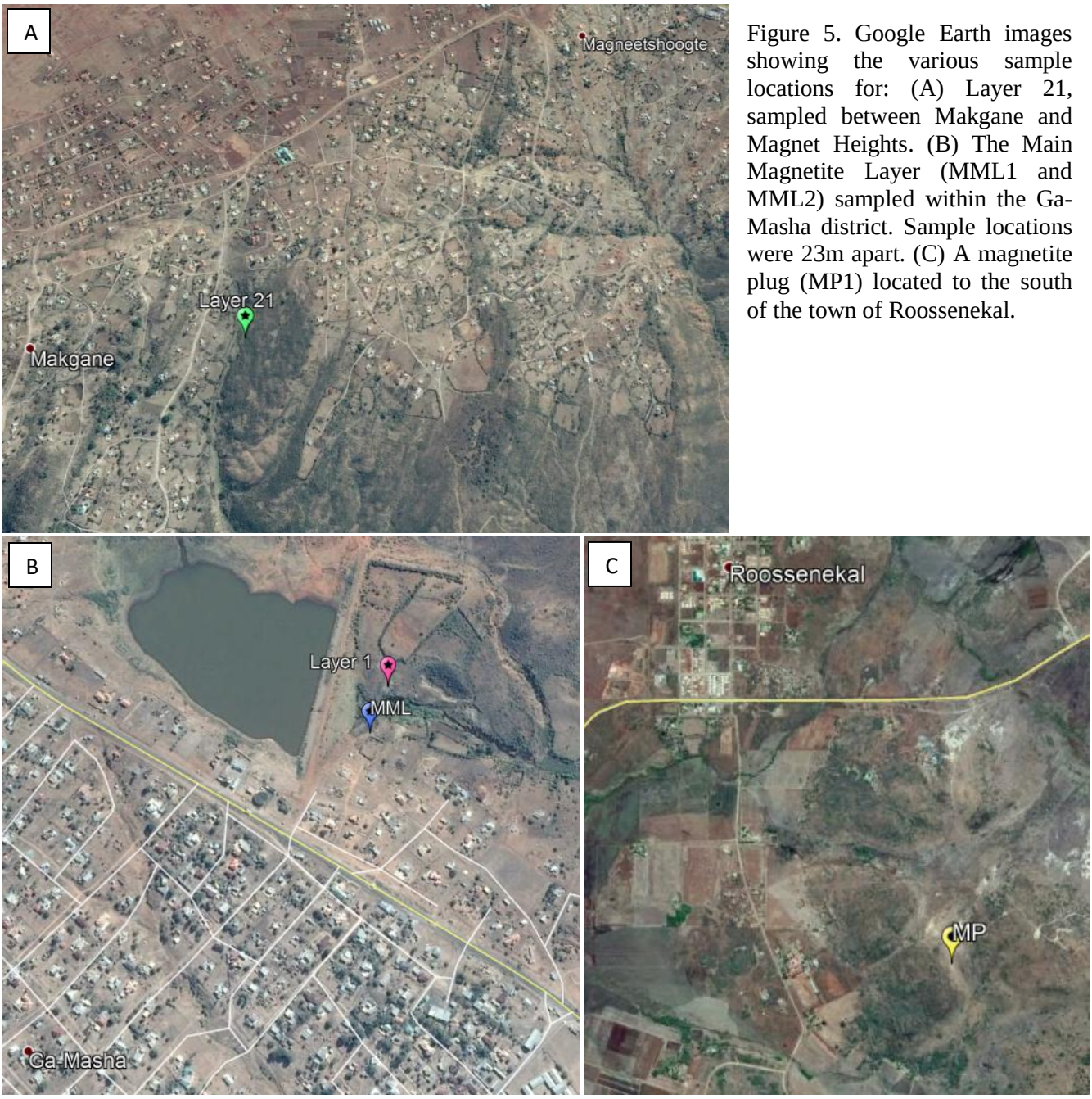

Figure 5. Google Earth images showing the various sample locations for: (A) Layer 21, sampled between Makgane and Magnet Heights. (B) The Main Magnetite Layer (MML1 and MML2) sampled within the Ga-Masha district. Sample locations were 23m apart. (C) A magnetite plug (MP1) located to the south of the town of Roossenekal.

Polished Sections

The various polished sections used in this study were made using the University of Pretoria's Metallurgy Department. Each sample was cut and polished using the diamond saw and polishing machine respectively. Samples were placed in 3D printed rings before a mixture of AKA resin and AKA cure was poured over them. The samples were then placed into the drying oven to set overnight. Once dry, the bottom of the rings was ground off and later polished using various diamond polishing discs ranging from 1mm down to 3µm. Special care was taken to prevent over-polishing.

Reflective Light Microscopy

Six polished sections were made from the samples collected from the various layers and the plug. One polished section was made for each layer and plug. The petrographical study of these polished sections was used as a preliminary study to identify minerals, examine textural relations and identify the reflective light properties of each sample.

Micro-focus X-ray Radiography and Tomography facility (MIXRad)

Micro-focus X-ray Computed Tomography technology becomes very attractive radiation based research technique since high-quality micron-level information of the interior, as well as the composition of samples, can be obtained non-invasively and non-destructively. Micro-focus investigations are therefore extensively focused in research fields such as the geosciences with typical investigations on porosity, mineral distribution and quantification (e.g. 3D Volume fractions), petrographical analyses, fracture (cleat) analysis etc. The South African Nuclear Energy Corporation (NECSA) accommodates post-graduate students in X-ray investigations in research projects with the aid of a 100kV X-ray source (Hoffman and De Beer, 2012).

The sample is fixed on the sample manipulator in the micro-focus X-ray cabinet to ensure no movement of the sample occurs during scanning. The sample is then horizontally optimised, for maximum enlargement of the sample to obtain optimal spatial resolution. This adjustment is also to ensure that the sample is horizontally included in each 2D radiograph at all angles of rotation and for correct normalisation during the tomography reconstruction process. The energy and current density settings are individually adjustable while the system is in operation. According to Hoffman and De Beer (2012), this allows one a careful adjustment to achieve at least 15% penetration through the sample but never exceeds 65535 grey values of dynamic range in areas without the sample. Filters are available to achieve a comfortable high dynamic range within the radiographs.

Once the sample is correctly positioned, a shading correction algorithm is obtained through acquiring flat field radiographs under the same conditions as the sample images but with the sample removed from the field of view. Additionally, radiographs with the X-rays switched off are acquired to remove possible non-functional pixels and to determine the grey value of air during the normalisation process. One flat field image (an average of up to 128 radiographs) and one "dark" image (an average of up to 128 radiographs) are usually obtained

to develop the shading correction (Hoffman and De Beer, 2012). The Inspect-X software incorporates these images in real-time during the scanning process so that the projections obtained from a CT scan are already normalised. The acquisition software also enables the researcher to correct for beam hardening artefacts and reconstruct in real time, but this is not desired since it is a time-consuming process.

The projection images are in an appropriate tiff-format for the reconstruction process to commence on the reconstruction PC the moment the scan is complete. CT-Pro reconstruction software, fully developed in-house by Nikon, is used to transform the 2D projections into a 3D volume. CT-Pro allows for rapid (<2min) reconstruction with limited input from the operator. The reconstruction parameters are optimised automatically so that the quality of a scan does not depend on a qualitative opinion of the operator. The final product from a reconstruction in CT-Pro is a RAW 3D volume file, which can be directly imported into VGStudioMax visualisation software that allows and enables the researcher to distinguish between different materials based upon segmentation (Hoffman and De Beer, 2012).

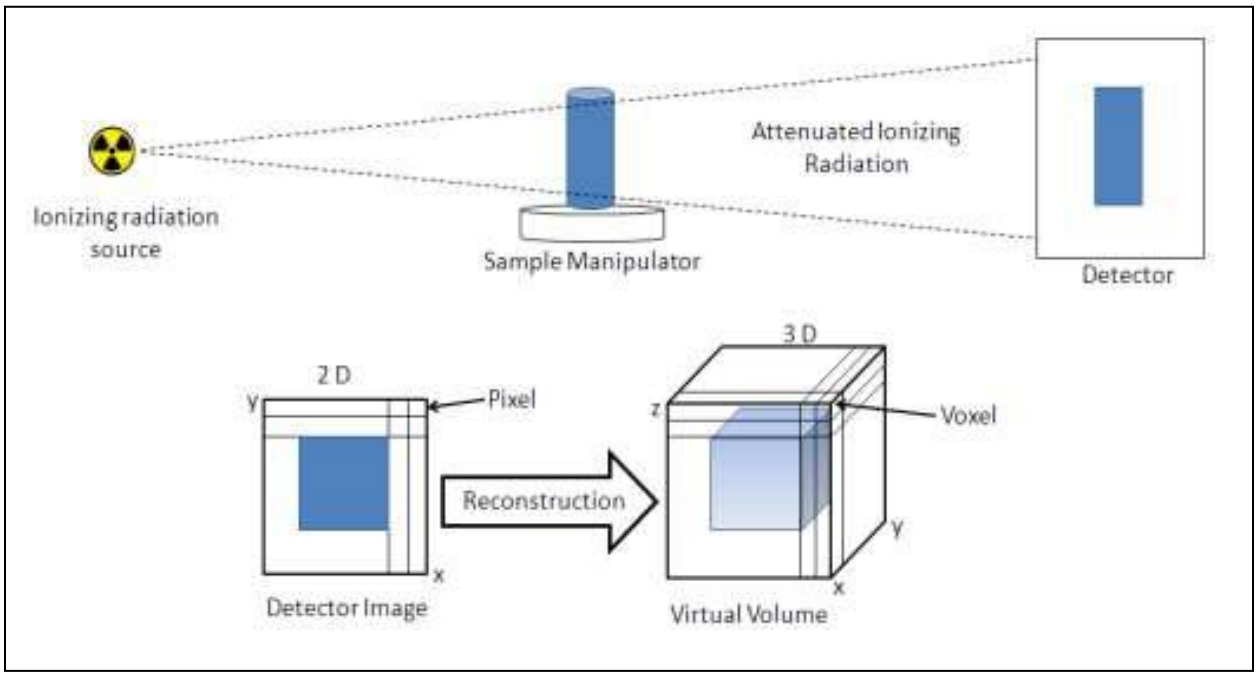

Figure 6. Image showing the Tomographic Process at the MIXRAD facility. Hoffman and De Beer (2012).

Unfortunately, due to the nature of the samples in the study, the MIXRad facility provided negative results. The density of the various minerals found within the titaniferous magnetites is so similar that the CT scan was unable to distinguish between different phases and therefore the processing of the images yielded no usable results.

Scanning Electron Microscope (SEM)

Point analyses, images, textural relationships and mineral identification were carried out for each polished section. The data were collected at the University of Pretoria's Metallurgy Department. Analytical conditions used during the analysis were an acceleration voltage of 15.0 kV (kept constant). Each polished section was analysed under low vacuum conditions. Point analyses of each polished section were used to identify the respective weight percentages of each element occurring within the various textural elements. The point analyses showed the various changes in elemental abundance throughout the section as well as differences from sample to sample. The SEM imaging and point analysis were conducted using AzTec Version 3.0 that also allowed for the identification of various forms of exsolution, and secondary textures, which are of major interest.

The Accuracy of the SEM Measurements

Excitation volume of the SEM electron beam defines the subsurface volume of material in the sample that interacts with the electron beam. The volume of the specimen interacting with the electron beam depends on the following factors: (1) the atomic number of the examined material (the higher atomic number materials absorb or stop more electrons and so have a smaller interaction volume), (2) the accelerating voltage being used (higher voltages penetrate farther into the sample and generate larger interaction volumes) and (3) the angle of incidence for the electron beam; (the greater the angle from normal, the smaller the volume). All atoms within the excitation volume are susceptible to excitation, resulting in multiple measured phases. The consequence is that even though great care is taken to place point analyses, the excitation volume often is larger than the targeted phase. Therefore, the data acquired through point analyses is treated as qualitative and not quantitative and is merely an indication of possible phases that are present. The Fe^{2+}/Fe^{3+} ratio proved difficult to calculate due to a total Fe-content measured by the SEM. The Fe^{2+} to Fe^{3+} proportions within each component may have contributed to the offset seen within the ternary diagrams for each sample, therefore skewing the data.

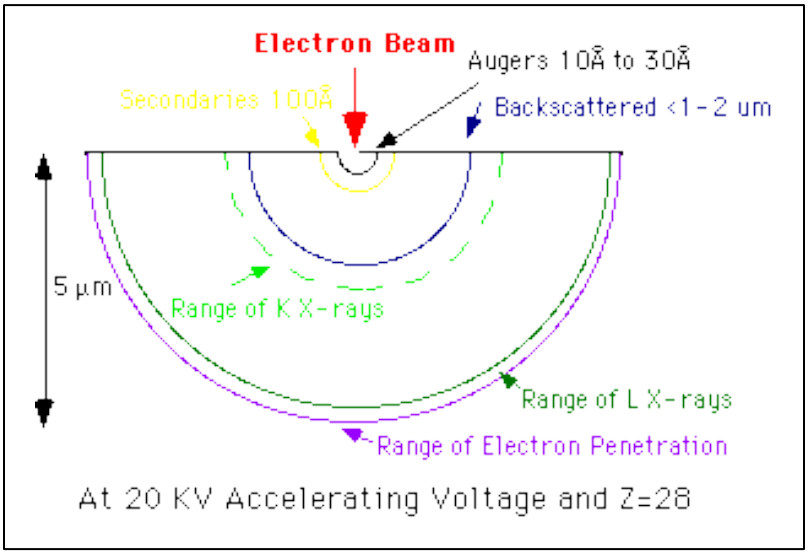

Figure 7. A schematic diagram of the excitation volume for an accelerating voltage of 20kV. The diagram shows the range of penetration and excitation in the surrounding material. (University of Nebraska, 2018)

Chapter 4: Results

Main Magnetite Layer (MML1)

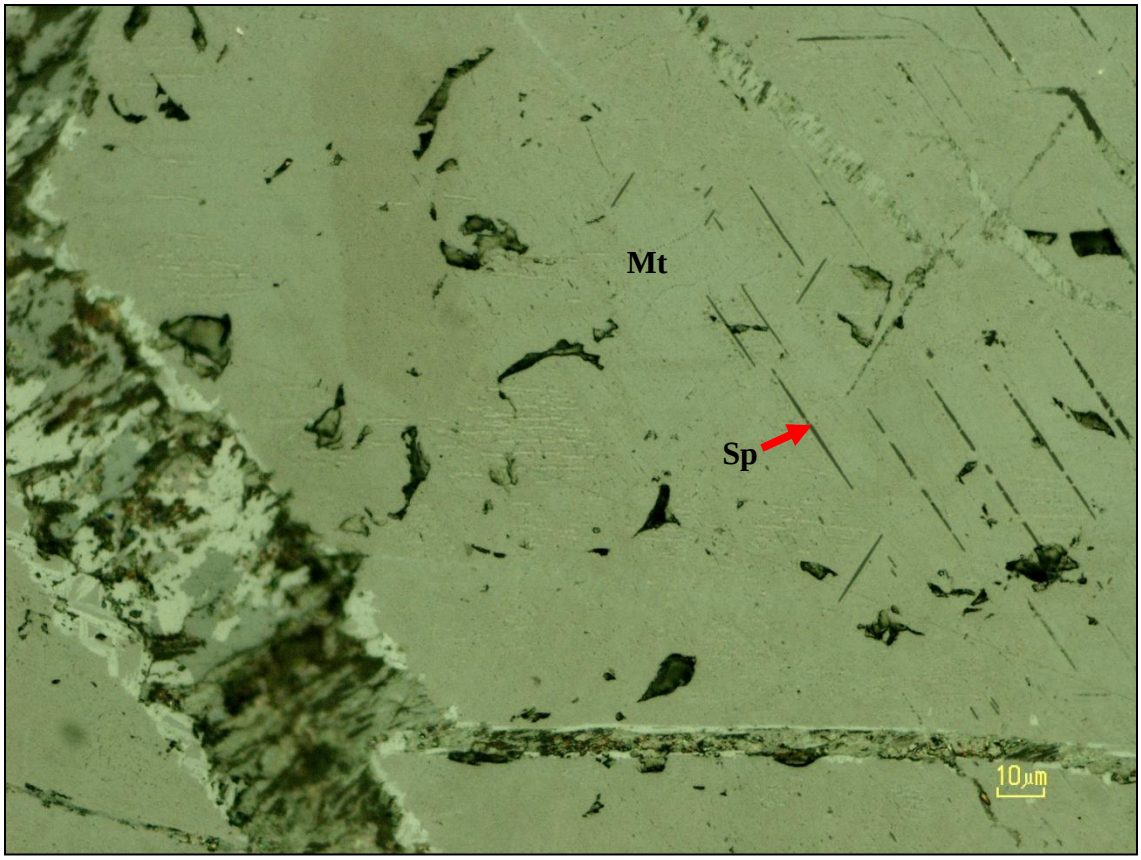

Figure 8. A photomicrograph of the MML1-2 polished section showing a magnetite grain with veins along the euhedral grain boundary as well as a spinel trellis-exsolution, a cloth microtexture and fractures. Image taken under 50x magnification. Mt = Magnetite, Sp = Spinel.

Grain sizes of magnetite grains vary from 0.5-1.5mm wide. Ilmenite grains vary in size from 1-2mm along the long axis of the elongated grain. Under plane-polarised light (PPL), the polished section shows very light grey colours for magnetite, pink-brown colours for ilmenite and dark grey colours for veins and fracture infilling. Under cross-polarised light (XPL), magnetite is isotropic, and ilmenite grains show a moderate anisotropy with dark grey colours. Most magnetite grains are subhedral to euhedral with hexagonal crystal morphology, whereas ilmenite grains are anhedral and elongated. Certain ilmenite grains show thin lamellae twinning. A spinel trellis exsolution is dominant throughout the section, occurring within magnetite grains, as well as a micro-cloth texture of ulvöspinel and magnetite, both visible within figure 8 above. In general, the polished section is highly fractured with the occurrence of multiple syntaxial veins and fracture infilling.

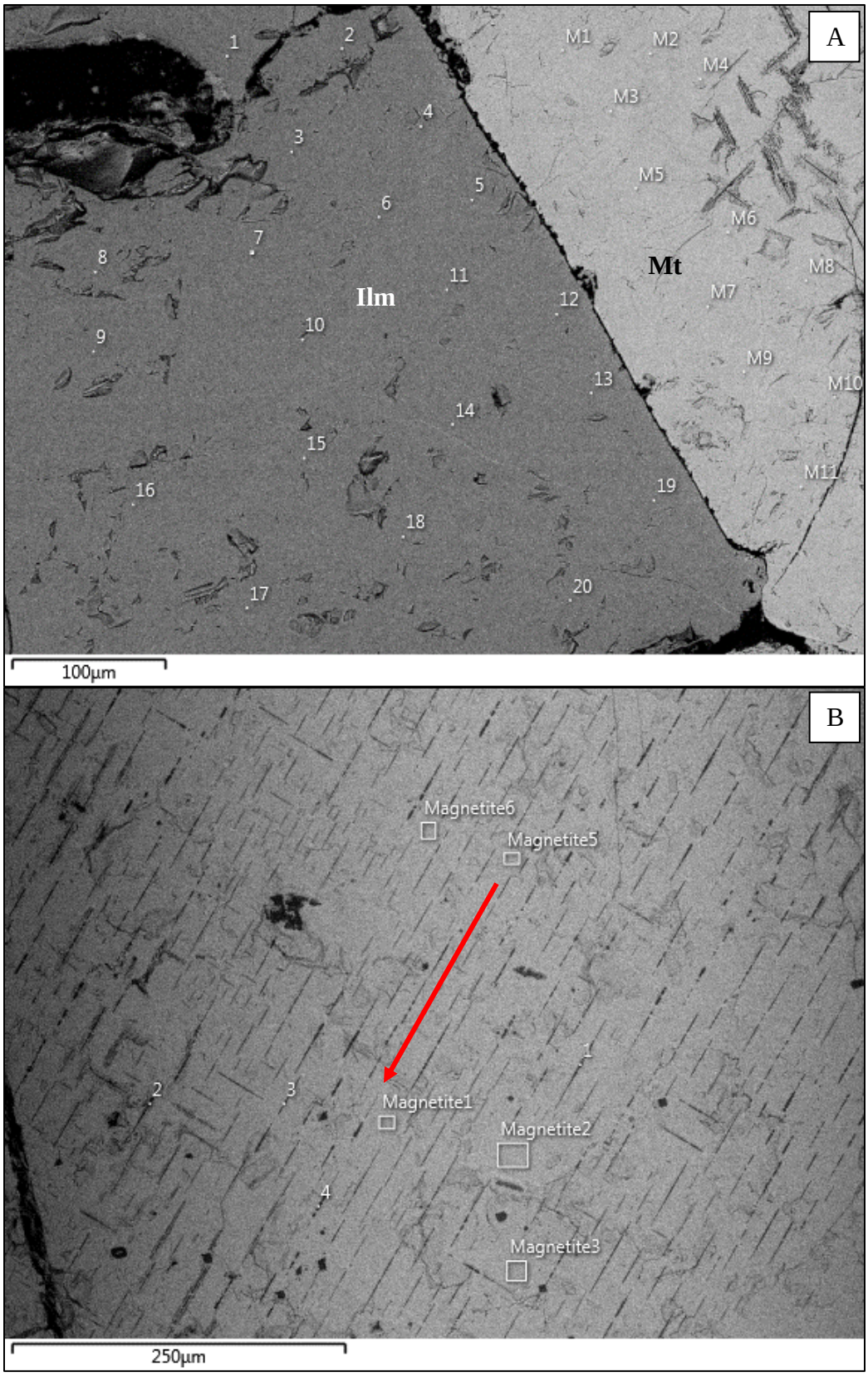

Figure 9. (A) A SEM image of the MML1-2 sample showing the magnetite-ilmenite grain boundary. The image shows the vein development along grain boundaries and fractures running across the respective grains. Darker grains are ilmenite and lighter grains are magnetite. Mt = Magnetite, Ilm = Ilmenite. (B) A SEM image of the MML1-2 sample showing a magnetite grain with extensive spinel trellis-exsolution. One plane (red arrow indicates direction) appears to show more continuous exsolution when compared to the perpendicular direction.

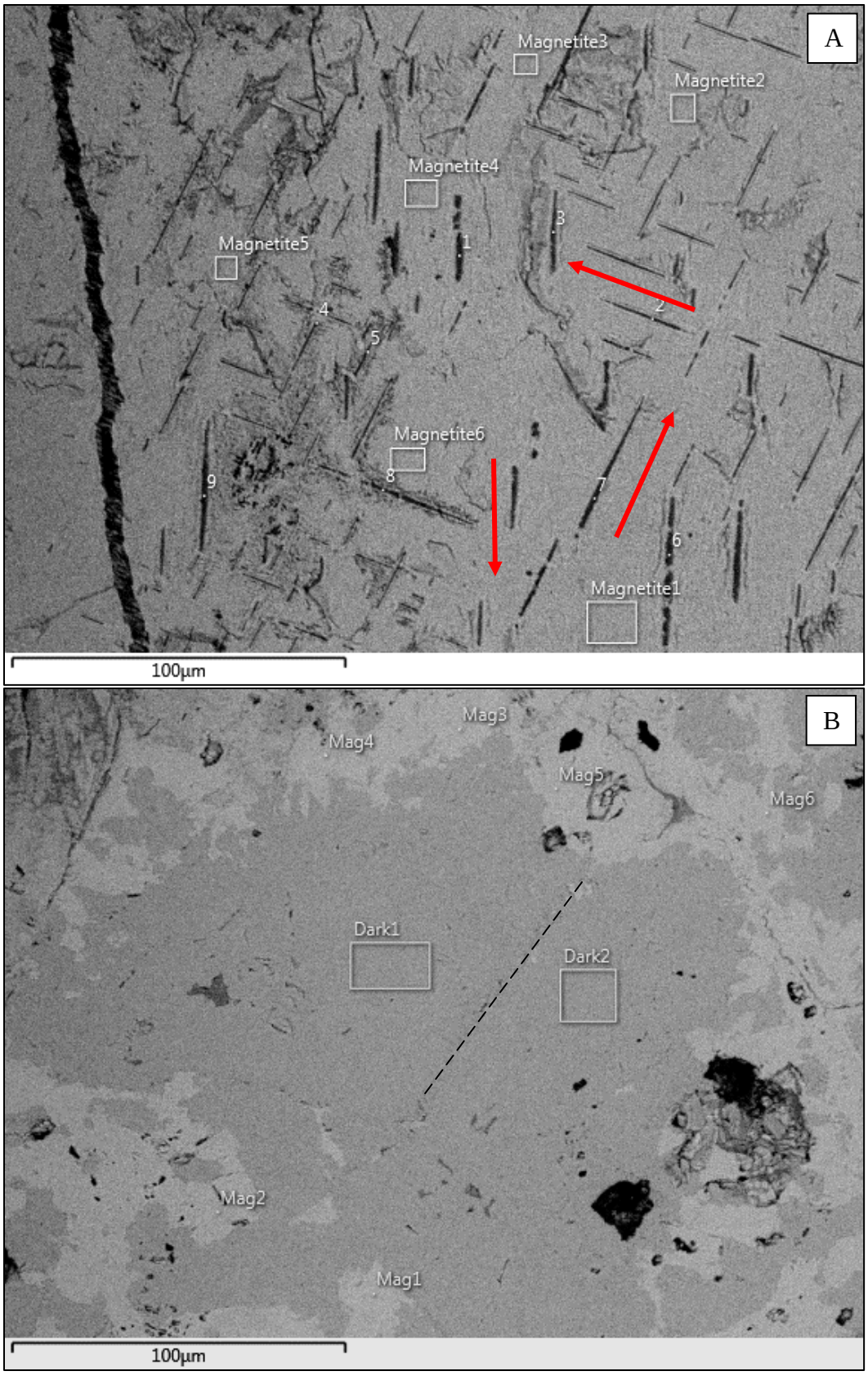

Figure 10. (A) A SEM image of the MML1-2 sample showing a magnetite grain with extensive spinel trellis-exsolution pattern. Certain areas around the exsolution show alteration rims. Three distinct directions of exsolution are visible within this image. (B) A SEM image of the MML1-2 sample showing a magnetite grain with martitization, represented by the darker areas and the unaltered magnetite, by the lighter areas. Healed fractures (dashed line) are also visible through the centre of the magnetite grain (Dark1 and Dark2 indicate a martitized magnetite grain).

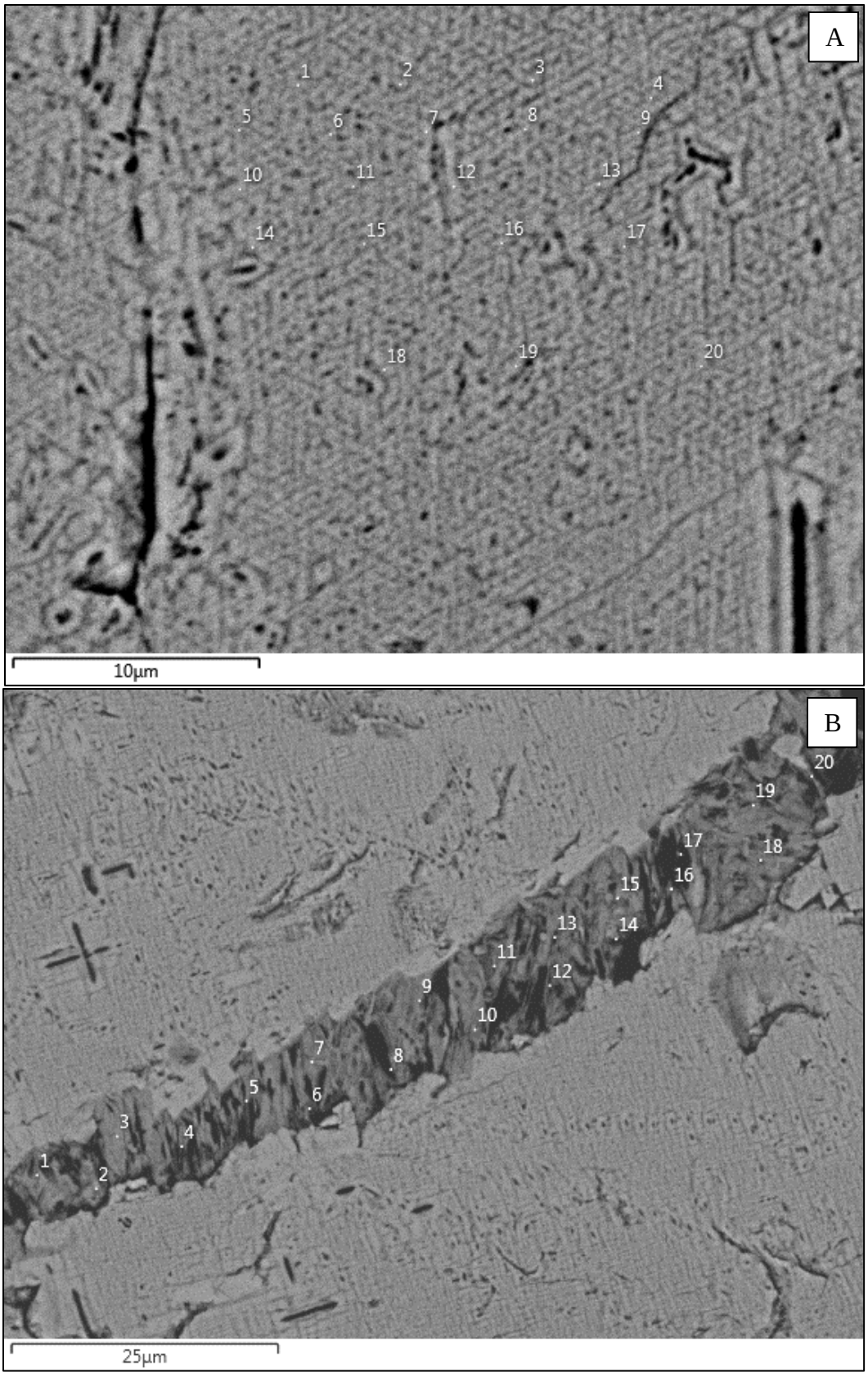

Figure 11. (A) A SEM image of the MML1-2 sample showing the cloth-texture exsolution of ulvöspinel within magnetite. (B) A SEM image of the MML1-2 sample showing a syntaxial vein passing through a magnetite grain. The magnetite grain shows a visible cloth-texture of ulvöspinel and magnetite. Some spinel trellis exsolution is also visible.

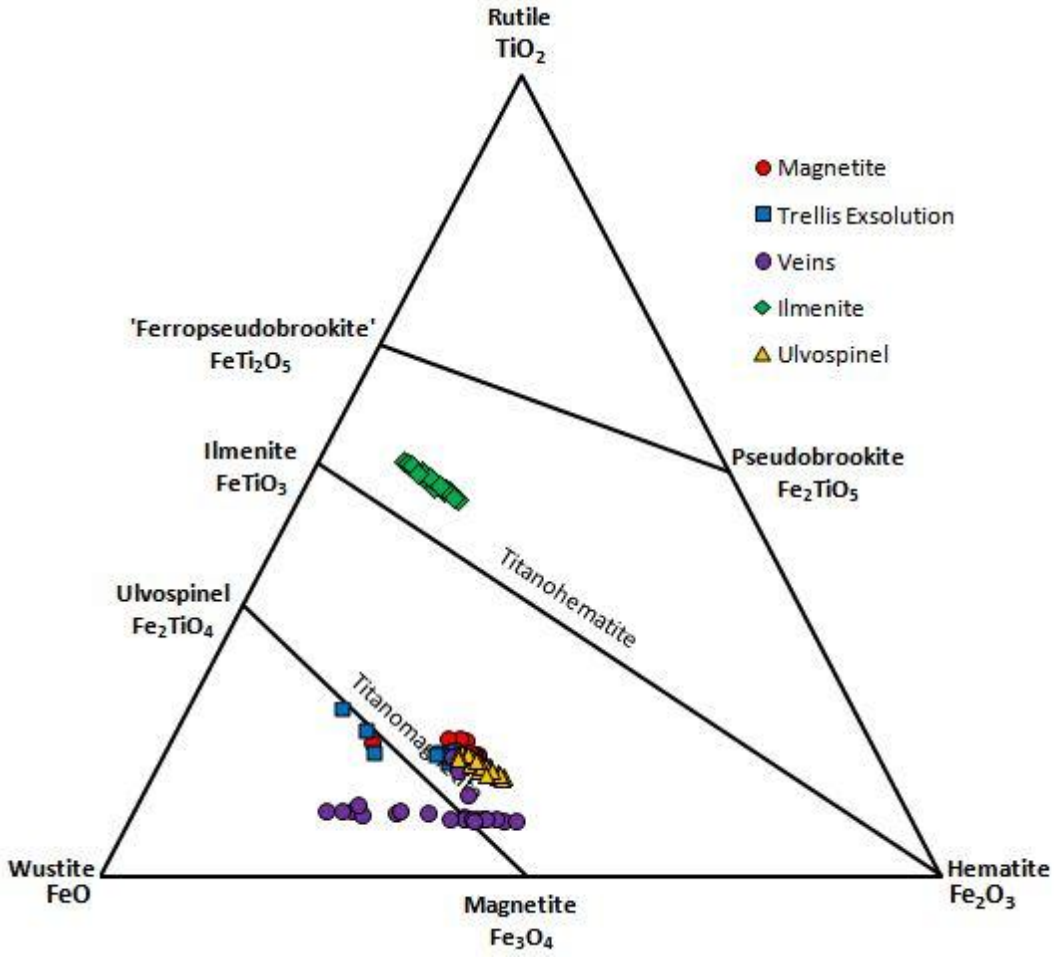

Figure 12. A FeO-TiO_2-Fe_2O_3 ternary diagram showing the respective concentrations of each element for various minerals and textures within the MML1 sample. Linear trends are visible for ilmenite, trellis exsolution, ulvöspinel and veins. Data from Table 1 and Appendix B.

Table 1: MML1 summary table shows the various summarised data analyses for the MML 1 sample for each component.									
Component		**FeO (Wt-%)**	**Fe_2O_3 (Wt-%)**	**TiO_2 (Wt-%)**	**Al_2O_3 (Wt-%)**	**SiO_2 (Wt-%)**	**MgO (Wt-%)**	**Cr_2O_3 (Wt-%)**	**V_2O_3 (Wt-%)**
Magnetite Grains	Min.	35.32	20.54	2.38	1.80	0.42	0.95	-	0.42
	Mean	43.20	38.42	11.51	3.47	1.28	1.22	-	1.55
	Max.	51.09	57.39	16.08	6.91	4.65	1.62	-	2.01
Ulvöspinel Cloth Texture	Min.	42.51	31.56	11.48	3.69	0.62	0.81	-	1.29
	Mean	44.38	35.24	12.83	4.28	0.85	1.08	-	1.55
	Max.	47.06	38.61	14.37	4.99	1.05	1.29	-	1.73
Ilmenite Grains	Min.	31.44	9.40	43.57	0.96	0.43	4.53	-	0.45
	Mean	33.69	13.43	46.20	1.16	0.58	4.80	-	0.70
	Max.	35.79	17.30	48.64	1.54	1.09	5.03	-	1.06
Spinel Trellis-Exsolution	Min.	30.17	19.13	8.92	11.17	0.42	2.15	-	1.14
	Mean	35.36	24.39	10.37	21.34	0.86	6.66	-	1.33
	Max.	46.62	28.22	13.32	28.77	2.56	9.45	-	1.59
Syntaxial Veins	Min.	43.15	17.39	6.05	4.06	1.05	-	-	0.86
	Mean	47.24	30.90	7.42	9.07	4.35	-	-	1.03
	Max.	53.37	41.90	14.01	21.54	8.43	-	-	1.72

The mean composition of both the magnetite grains and the ulvöspinel cloth-texture show similar concentrations in FeO, Fe_2O_3, TiO_2 and Al_2O_3 as seen in Table 1. Magnetite shows a slightly higher concentration in Fe_2O_3, whereas ulvöspinel shows a slightly higher concentration in FeO, TiO_2 and Al_2O_3. Ilmenite grains show relatively lower concentrations of FeO and Fe_2O_3, with significantly higher amounts of TiO_2. The ilmenite grains appear significantly depleted in Al_2O_3 when compared with the various other textural elements. The spinel trellis-exsolution shows a very similar concentration to that of the ilmenite grains; however, the trellis-exsolution appears depleted in TiO_2 and significantly enriched in Fe_2O_3 and Al_2O_3. The various veins that run through the sample show relative concentrations in FeO and SiO_2 and a relative depletion in TiO_2 when compared with the various other textural elements. The MML1 sample analyses had no chromium concentrations in any of the textural elements, with no magnesium within the veins.

Main Magnetite Layer (MML2)

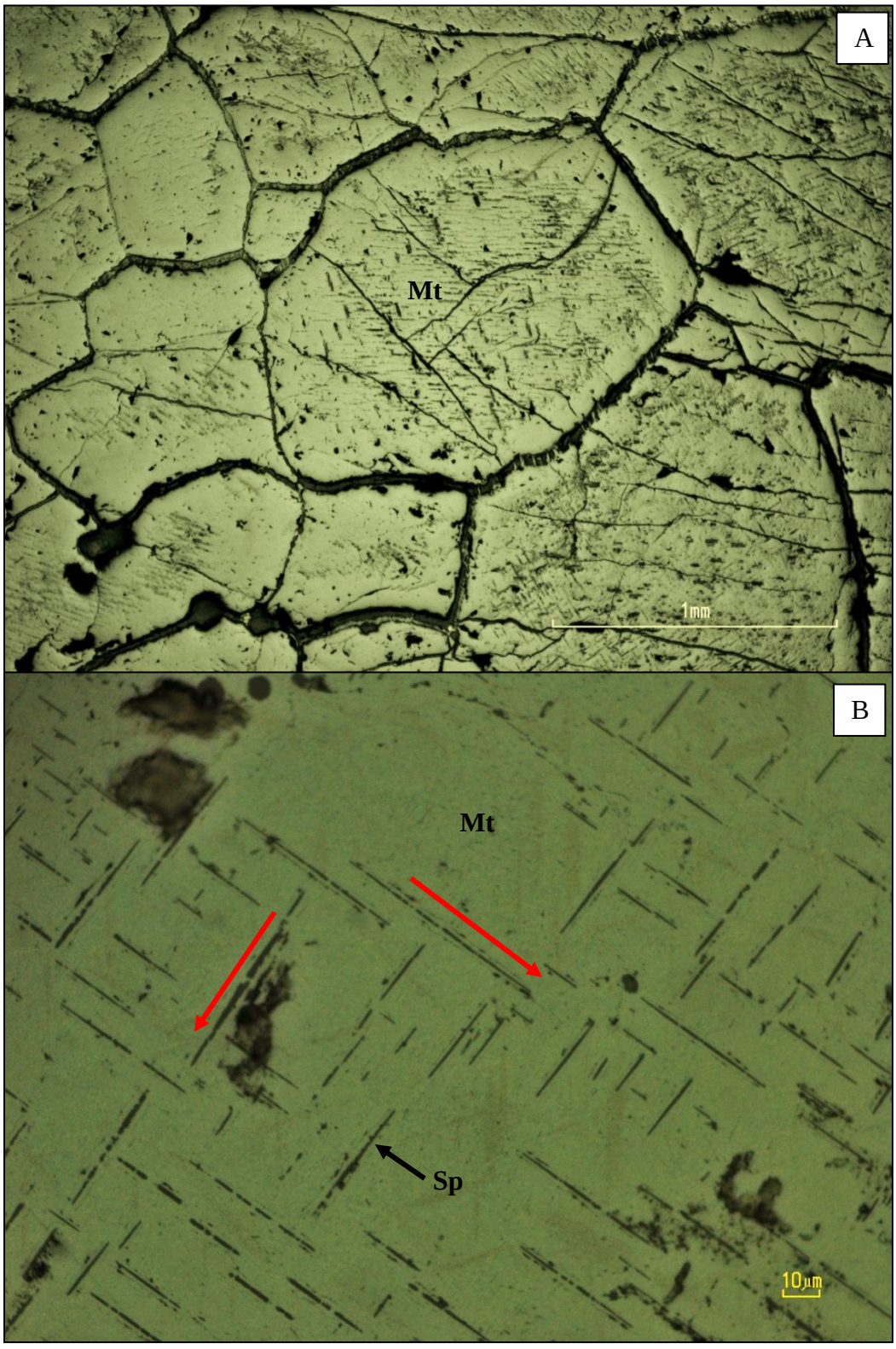

Figure 13. (A) A photomicrograph of the MML2 sample showing subhedral magnetite grains with spinel trellis-exsolution patterns. Alteration rims are visible around some of the trellis exsolution. Veins have developed along grain boundaries. Image was taken under 5x magnification. (B) A photomicrograph of the MML2 sample showing the extensive spinel trellis exsolution, with two distinct directions. Image was taken under 50x magnification. Mt = Magnetite, Sp = Spinel.

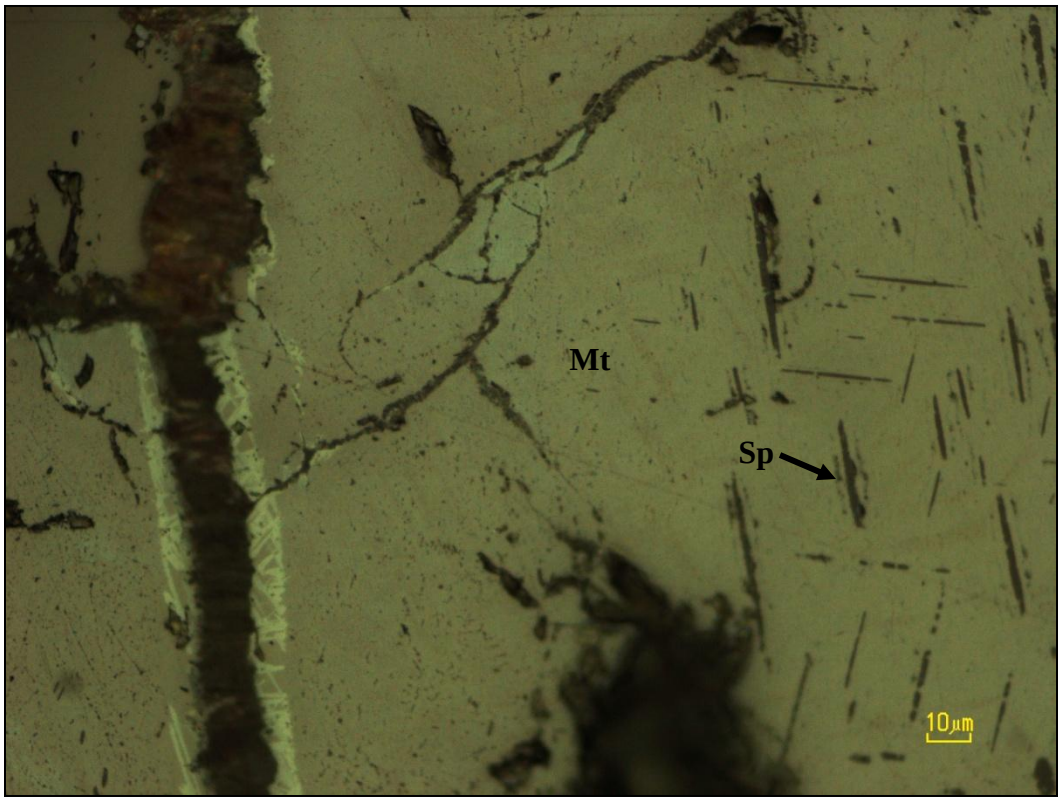

Figure 14. A photomicrograph of the MML2 sample showing the edge of a magnetite grain. A syntaxial vein is visible along the boundary, the outer edge of which shows extremely small trellis exsolution. Fractures and spinel trellis exsolution is visible. Image was taken under 50x magnification. Mt = Magnetite, Sp = Spinel

Grain sizes of magnetite grains range from 0.3-1.2mm wide. Under plane-polarised light (PPL), the polished section shows very light grey colours for magnetite and dark grey colours for veins and fracture infilling. Under cross-polarised light (XPL), magnetite is isotropic, and ilmenite grains show a moderate anisotropy with dark grey colours. Most magnetite grains are anhedral to subhedral with hexagonal crystal morphology. A spinel trellis exsolution is dominant throughout the section, occurring within magnetite grains as seen in figure 13a, as well as a patchy cloth texture exsolution of ulvöspinel and magnetite, seen in figure 14 above. In general, the polished section shows extensive fracturing with the occurrence of multiple syntaxial veins and fracture infilling. Triple junctions at grain boundaries are highly visible within this sample.

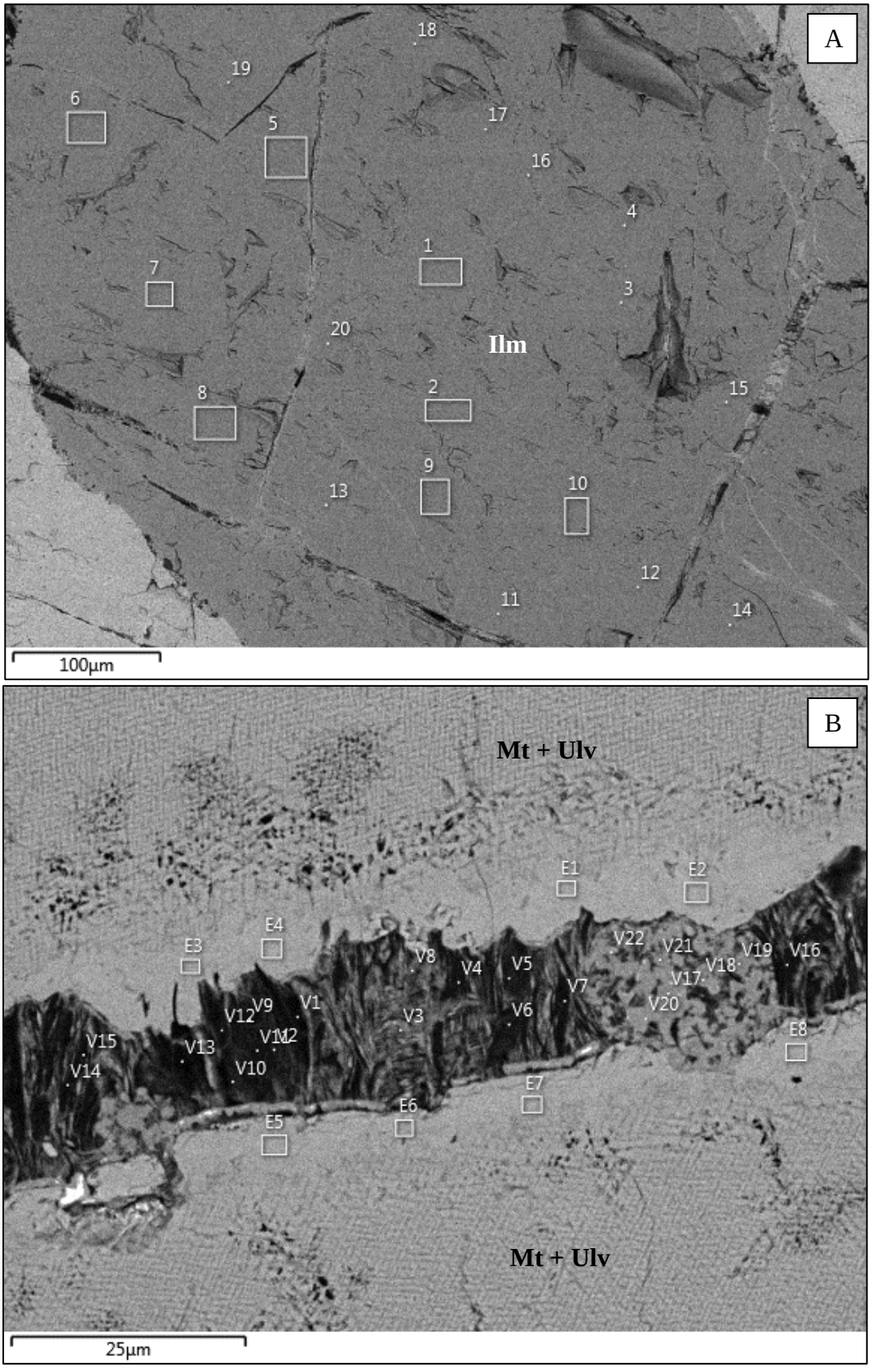

Figure 15. (A) A SEM image of the MML2 sample showing an elongated ilmenite grain with extensive fracturing and vein infilling. Ilm = Ilmenite. (B) A SEM image of the MML2 sample showing a syntaxial vein bordered by two magnetite grains with well-developed cloth-texture exsolution of ulvöspinel and magnetite. Small fractures are visible along the edge of the respective magnetite grains. Mt = Magnetite, Ulv = Ulvöspinel.

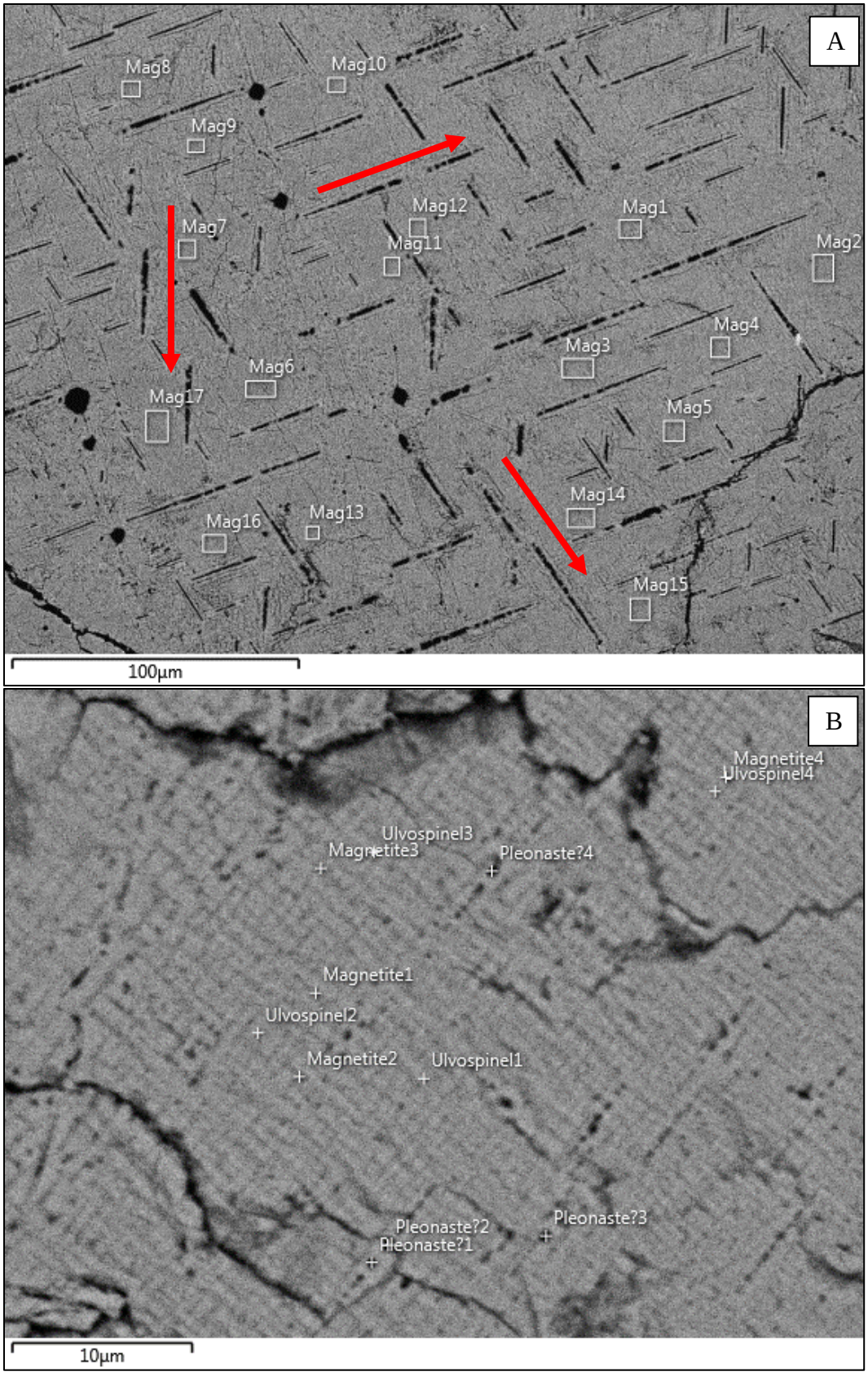

Figure 16. (A) A SEM image of the MML2 sample showing extensive spinel trellis exsolution within a magnetite grain. Three distinct directions are visible (indicated by the red arrows). (B) A SEM image of the MML2 showing the cloth-texture exsolution of ulvöspinel and magnetite found throughout the MML2 sample. Extensive fracturing is also visible within the image.

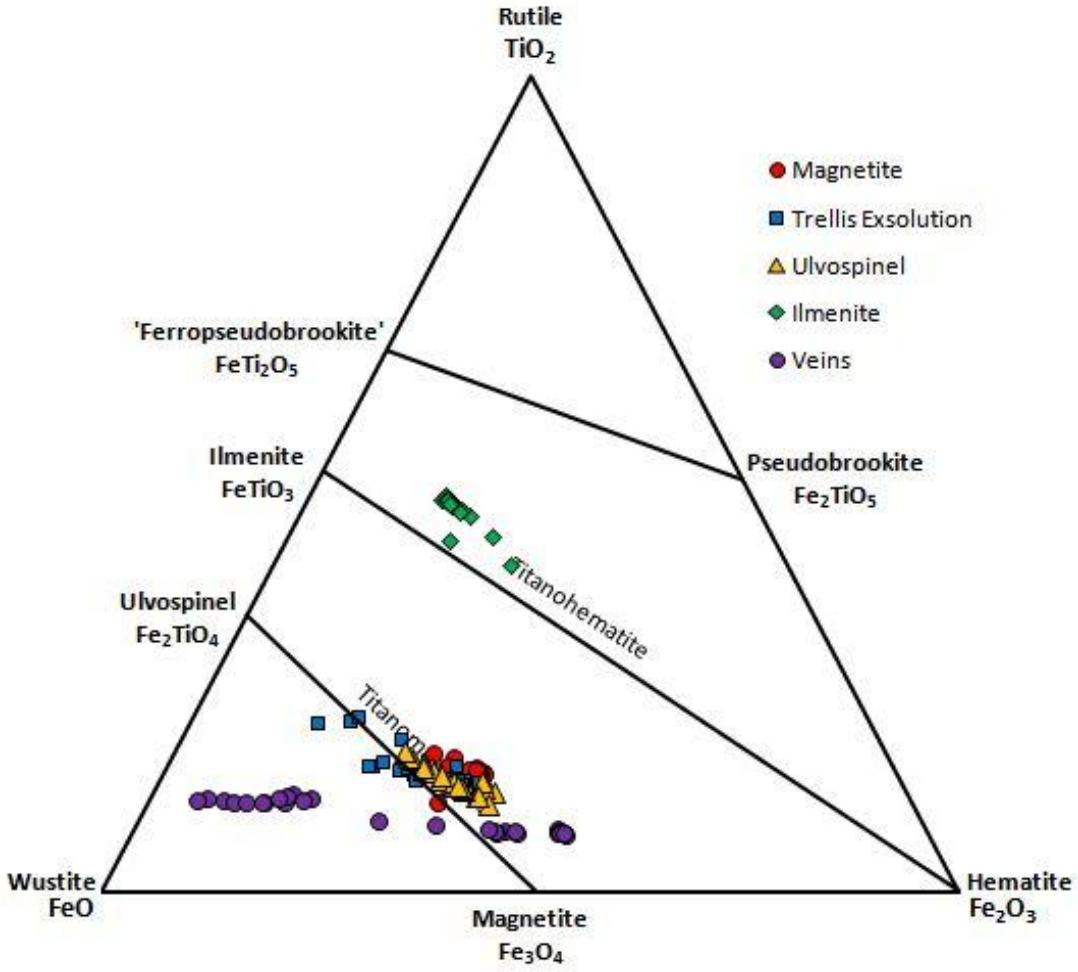

Figure 17. A FeO-TiO_2-Fe_2O_3 ternary diagram showing the respective concentrations of each element for various minerals and textures within the MML 2 sample. Linear trends are visible for ilmenite, ulvöspinel, trellis-exsolution and veins. Data from Table 2 and Appendix B.

Table 2: MML2 Summary Table shows the various summarised data analyses for the MML 2 sample for each component.									
Component		**FeO (Wt-%)**	**Fe_2O_3 (Wt-%)**	**TiO_2 (Wt-%)**	**Al_2O_3 (Wt-%)**	**SiO_2 (Wt-%)**	**MgO (Wt-%)**	**Cr_2O_3 (Wt-%)**	**V_2O_3 (Wt-%)**
Magnetite Grains	Min.	40.87	28.24	10.24	2.79	0.84	0.81	-	1.44
	Mean	45.19	32.27	13.59	4.39	1.45	1.77	-	1.60
	Max.	49.79	33.65	16.19	6.36	4.87	5.58	-	1.87
Ulvöspinel Cloth Texture	Min.	42.64	23.15	9.48	2.77	0.84	2.13	-	1.16
	Mean	45.50	29.62	12.13	6.83	2.59	2.25	-	1.44
	Max.	48.50	37.46	15.13	8.45	3.19	2.47	-	1.74
Ilmenite Grains	Min.	30.50	14.53	38.03	1.14	0.43	1.02	-	0.59
	Mean	32.94	16.51	44.13	1.54	0.58	4.17	-	0.65
	Max.	35.52	26.22	45.70	4.45	0.66	4.69	-	0.75
Spinel Trellis-Exsolution	Min.	34.37	12.25	8.84	4.25	1.47	0.83	-	1.03
	Mean	44.56	22.68	12.52	13.89	1.93	3.06	-	1.51
	Max.	54.50	33.34	19.55	28.32	2.84	8.12	-	1.92
Syntaxial Veins	Min.	38.91	3.46	6.42	3.82	1.85	1.12	-	0.58
	Mean	44.12	25.27	6.78	11.16	7.47	4.49	-	0.85
	Max.	51.98	46.56	7.07	18.80	13.32	10.79	-	1.05

The mean composition of both the magnetite grains and the ulvöspinel cloth-texture show similar concentrations in FeO, Fe_2O_3, TiO_2 and Al_2O_3 as seen in table 2. Magnetite shows a slightly higher concentration in Fe_2O_3 and TiO_2, whereas ulvöspinel shows a slightly higher concentration in FeO and Al_2O_3. Ilmenite grains show relatively lower concentrations of FeO and Fe_2O_3, with significantly higher amounts of TiO_2. The ilmenite grains appear significantly depleted in Al_2O_3 when compared with the various other textural elements. The spinel trellis-exsolution shows a very similar concentration to that of the magnetite grains; however, the trellis-exsolution appears depleted in Fe_2O_3 and TiO_2 and significantly enriched in Al_2O_3. The various veins that run through the sample show similar concentrations of FeO and Al_2O_3, with a relative depletion in TiO_2, when compared with the various other textural elements. The MML2 sample analyses had no chromium concentrations in any of the textural elements.

Magnetite Plug (MP1)

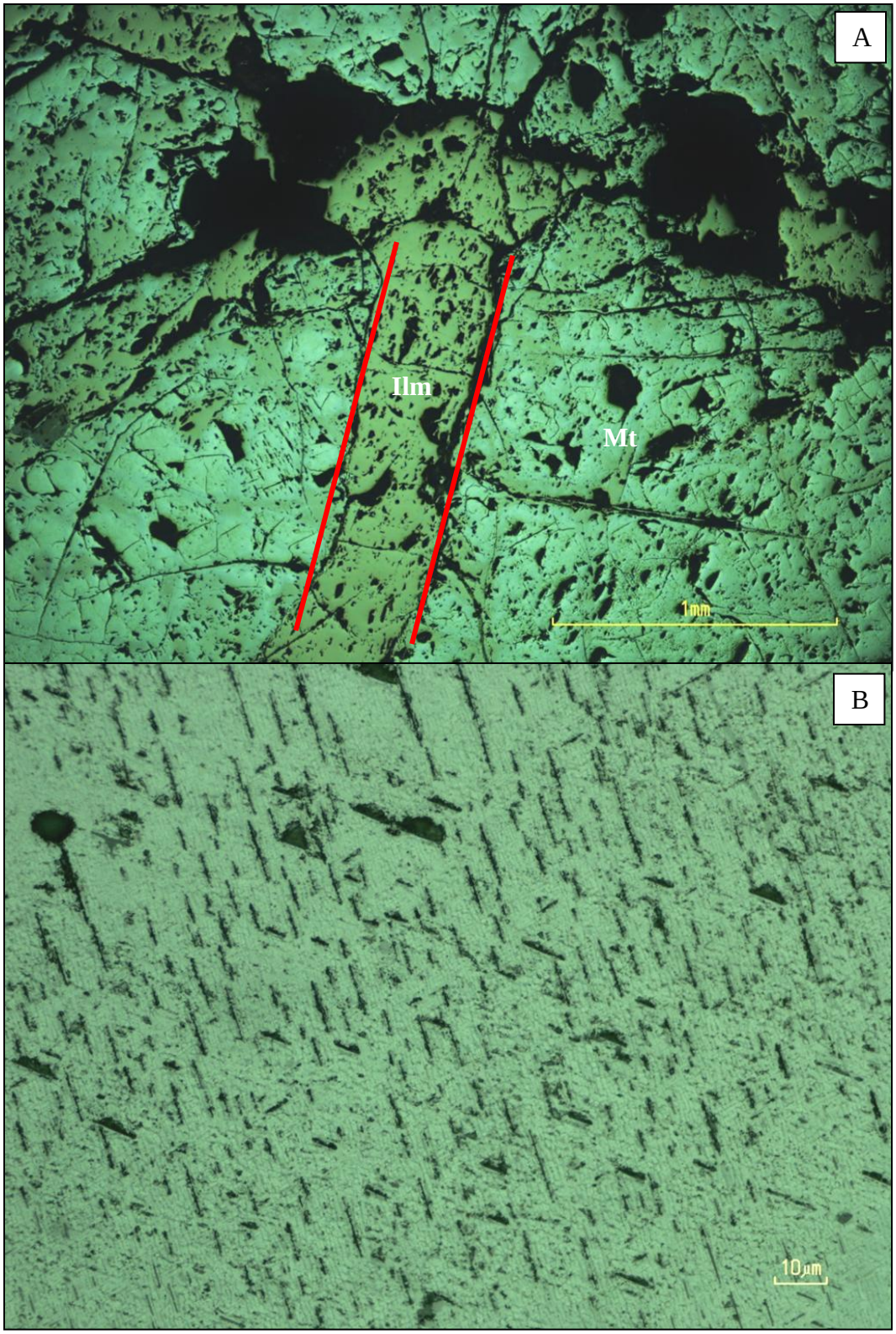

Figure 18. (A) A photomicrograph of a highly weathered MP1 sample showing an elongated ilmenite grain surrounded by anhedral magnetite grains. Image taken under 5x magnification. Mt = Magnetite, Ilm = Ilmenite. (B) A photomicrograph of the MP1 sample showing extensive spinel trellis exsolution with a micro-cloth texture exsolution of ulvöspinel and magnetite. Image taken under 50x magnification.

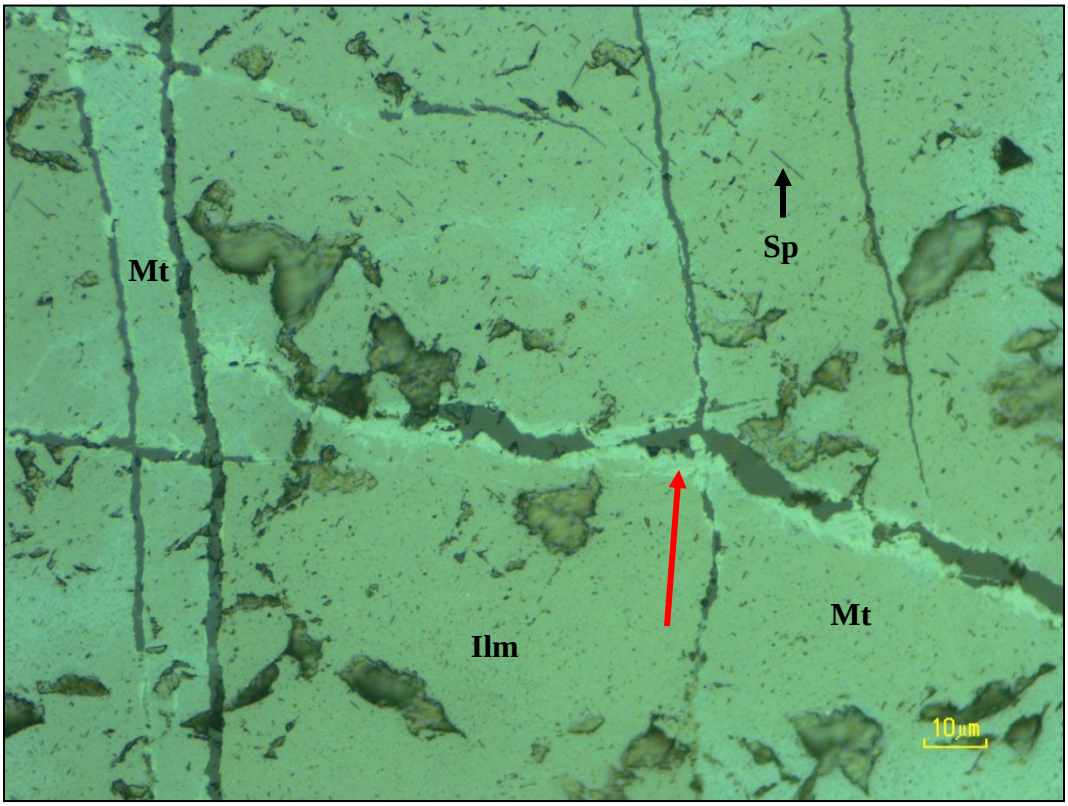

Figure 19. A photomicrograph of the MP1 sample showing the parallel vein development as well as a large syntaxial vein (red arrow) within the MP1 sample. Image was taken under 50x magnification. Mt = Magnetite, Sp = Spinel, Ilm = Ilmenite.

Since the magnetite grains are anhedral, no clear size range was calculated as an accurate representation. Under plane-polarised light (PPL), the polished section shows very light grey colours for magnetite, pink-brown colours for ilmenite and dark grey colours for veins and fracture infilling. Under cross-polarised light (XPL), magnetite is isotropic, and ilmenite grains and gangue mineral grains show a moderate anisotropy with dark grey colours and green-browns respectively. Most magnetite grains are anhedral or with no distinct morphology, whereas ilmenite grains are elongated as seen in figure 18a. Gangue minerals have no recognisable crystal form or habit. A spinel trellis exsolution is dominant throughout the section, occurring within magnetite grains, as well as well-developed cloth-texture exsolution of ulvöspinel and magnetite, visible within figure 19 above. Spinel trellis exsolution ranges in size from 1-8µm seen in figure 18b. In general, the polished section shows extensive fracturing with the occurrence of multiple syntaxial veins and fracture infilling.

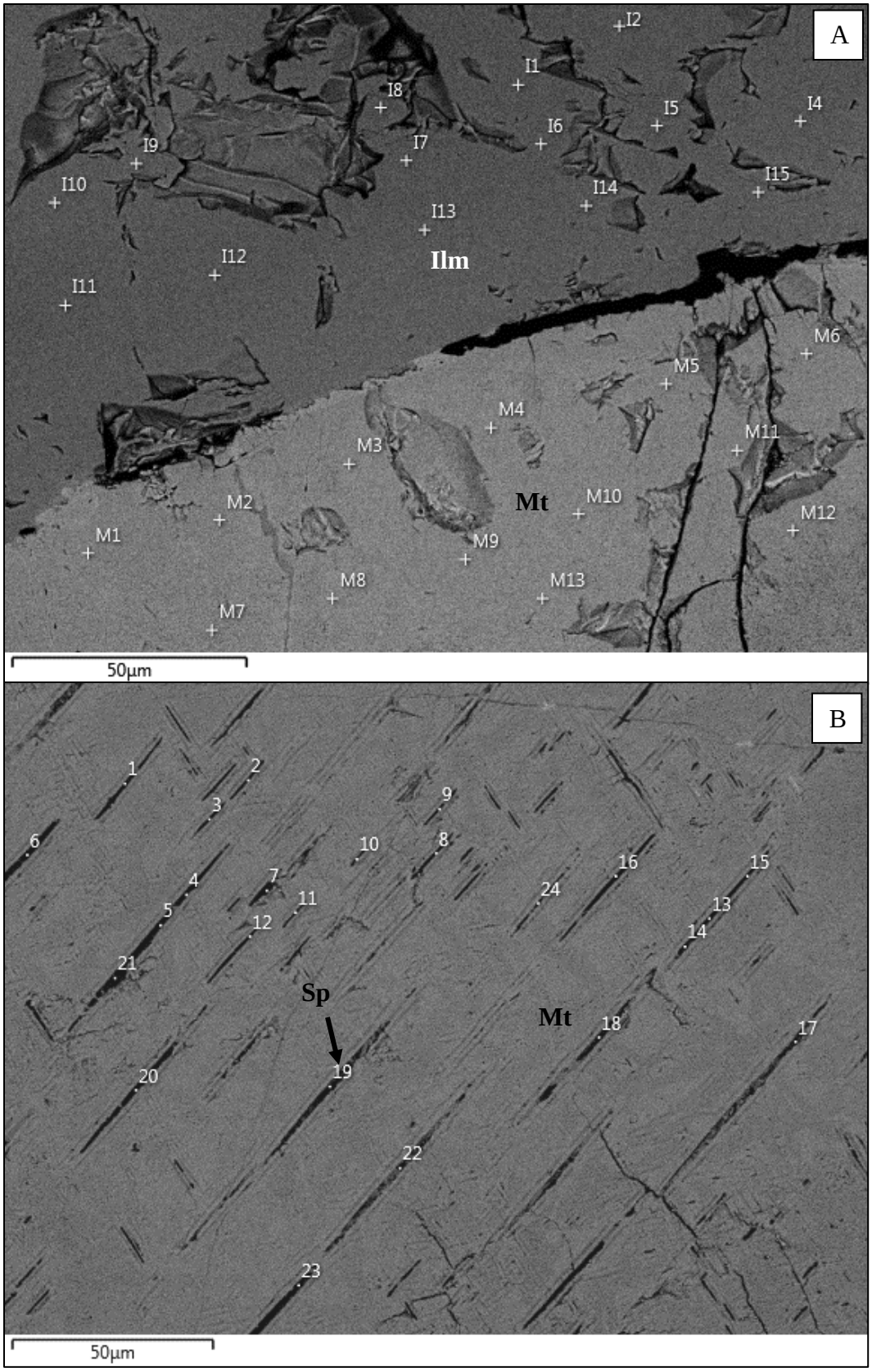

Figure 20. (A) A SEM image of the MP1 sample showing an ilmenite-magnetite boundary, with vein development along the boundary and fracturing occurring within the magnetite grain. (B) A SEM image of the MP1 sample showing a magnetite grain with spinel trellis exsolution growth in two distinct directions, with one direction more favorable than the other direction. Mt = Magnetite, Sp = Spinel, Ilm = Ilmenite.

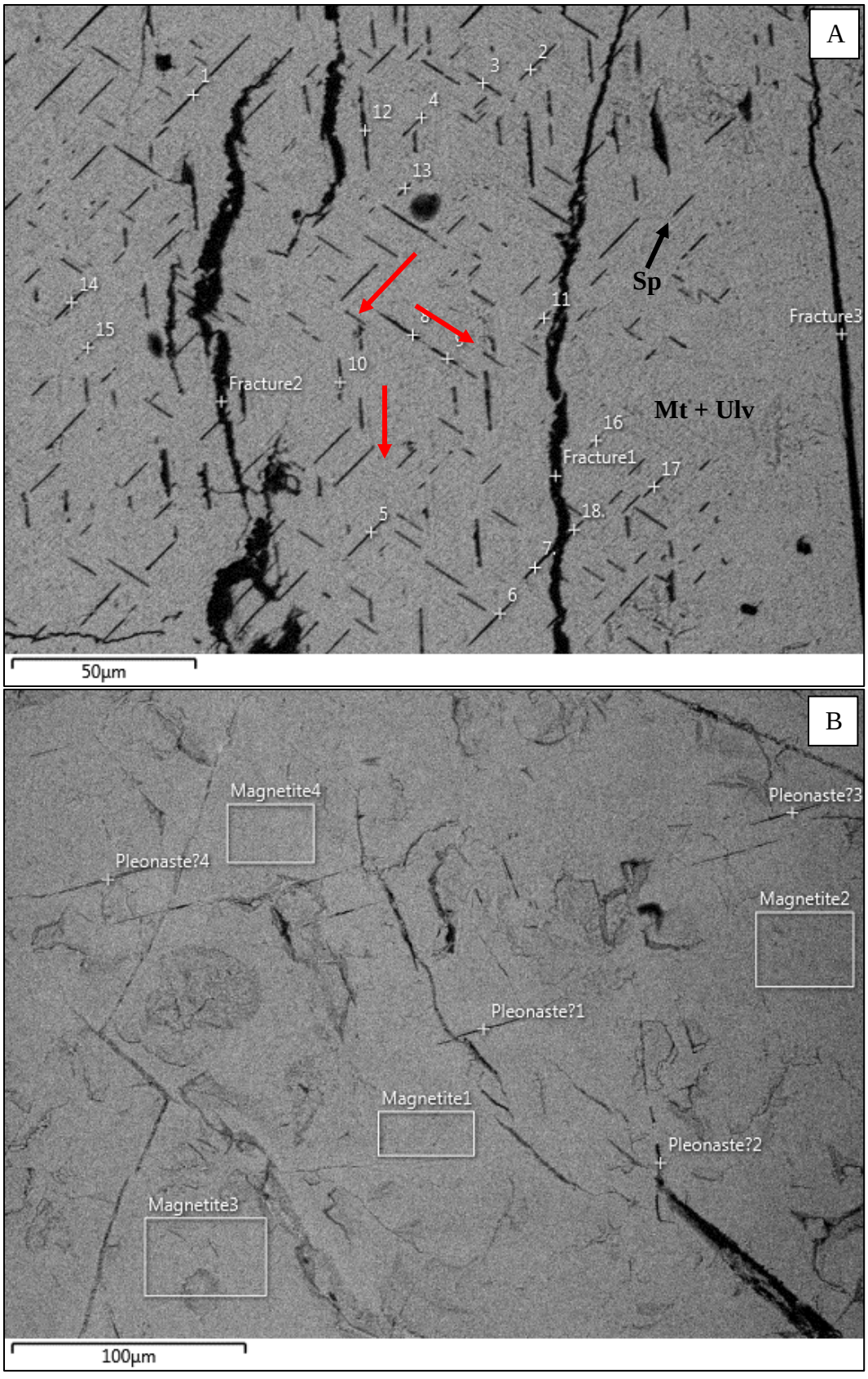

Figure 21. (A) A SEM image of the MP1 sample showing a magnetite grain with extensive fracturing and infilling as well as a spinel trellis exsolution with three distinct directions and a well developed cloth-texture exsolution of ulvöspinel and magnetite. (B) A SEM image of the MP1 sample showing its massive habit and extensive fracturing.

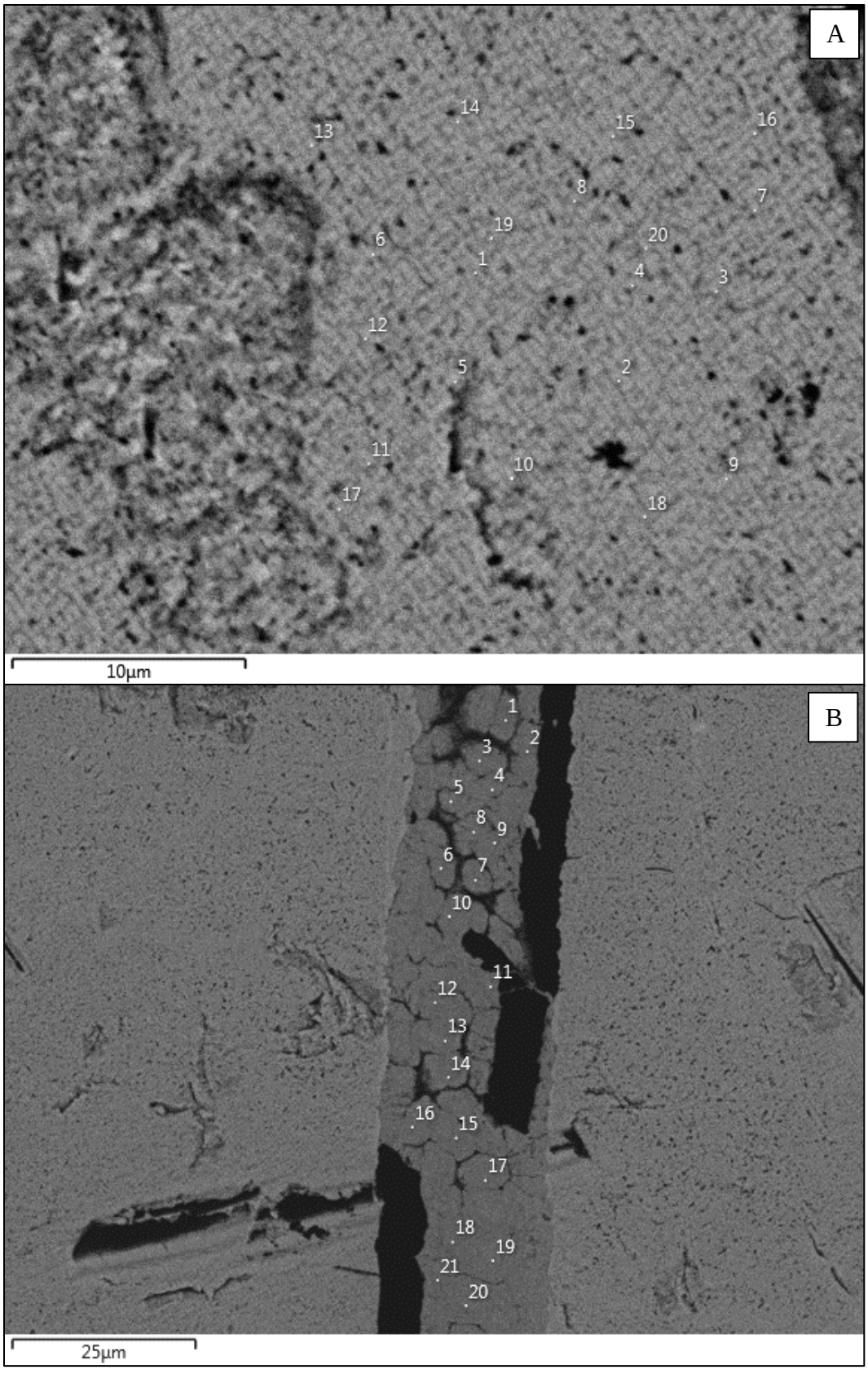

Figure 22. (A) A SEM image of the MP1 sample showing the micro-cloth texture exsolution of ulvöspinel and magnetite. (B) A SEM image of the MP1 sample showing a large blocky syntaxial vein that appears to have euhedral to subhedral Fe-Ti-Al oxide grains. Magnetite grains with a well-developed cloth texture exsolution surround the vein.

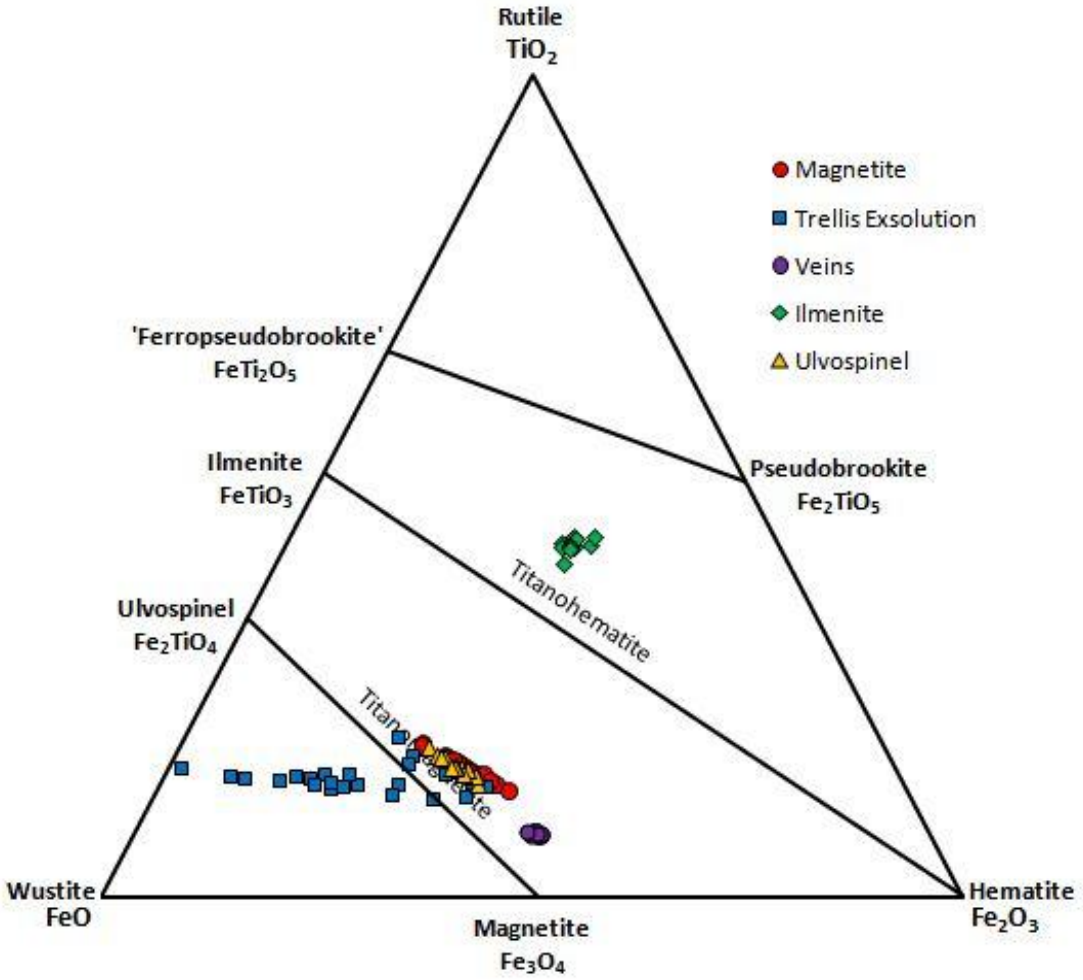

Figure 23. A FeO-TiO_2-Fe_2O_3 ternary diagram showing the respective concentrations of each element for various minerals and textures within the MP1 sample. Linear trends are visible for ulvöspinel, trellis-exsolution and magnetite. Data from Table 3 and Appendix B.

Table 3: MP1 Summary Table shows the various summarised data analyses for the MP1 sample for each component.									
Component		**FeO (Wt-%)**	**Fe_2O_3 (Wt-%)**	**TiO_2 (Wt-%)**	**Al_2O_3 (Wt-%)**	**SiO_2 (Wt-%)**	**MgO (Wt-%)**	**Cr_2O_3 (Wt-%)**	**V_2O_3 (Wt-%)**
Magnetite Grains	Min.	44.02	25.87	12.32	2.77	0.42	-	0.57	1.16
	Mean	47.27	32.13	14.89	3.26	0.53	-	0.68	1.55
	Max.	50.00	38.45	17.43	4.47	0.63	-	0.86	2.15
Ulvöspinel Cloth Texture	Min.	46.49	27.13	13.21	2.22	0.63	-	0.43	1.44
	Mean	47.85	31.34	15.07	2.96	0.71	-	0.56	1.54
	Max.	50.02	34.61	17.44	4.07	1.05	-	0.72	1.73
Ilmenite Grains	Min.	29.59	19.81	38.21	1.56	0.22	2.17	-	0.74
	Mean	31.14	22.45	40.35	1.93	0.45	3.19	-	0.84
	Max.	33.55	24.53	41.74	2.29	0.65	3.93	-	1.06
Spinel Trellis-Exsolution	Min.	43.80	0.76	9.09	4.90	0.42	-	0.44	0.89
	Mean	47.22	18.34	11.38	21.04	0.59	-	0.61	1.41
	Max.	51.96	34.82	18.31	39.41	1.27	-	0.75	2.02
Syntaxial Veins	Min.	41.24	40.87	6.80	5.30	1.04	-	-	0.86
	Mean	41.72	42.46	7.10	6.16	1.33	-	-	1.24
	Max.	42.21	43.19	7.46	7.17	1.87	-	-	1.71

The mean composition of both magnetite grains and the ulvöspinel cloth-texture show similar concentrations in FeO, Fe_2O_3, TiO_2 and Al_2O_3 as seen in table 3. The weight percentages of each oxide within magnetite and ulvöspinel respectively differ by less than one weight percent. Ilmenite grains show relatively lower concentrations of FeO and Fe_2O_3, with significantly higher amounts of TiO_2. The ilmenite grains appear depleted in Al_2O_3 when compared with the various other textural elements. The spinel trellis-exsolution shows a very similar concentration to that of the magnetite grains; however, the trellis-exsolution appears depleted in Fe_2O_3 and TiO_2 and significantly enriched in Al_2O_3. The various veins that run through the sample show relative concentrations in Fe_2O_3 and SiO_2 and a relative depletion in FeO and TiO_2, when compared with the various other textural elements.

Layer 8 (UZ8/17)

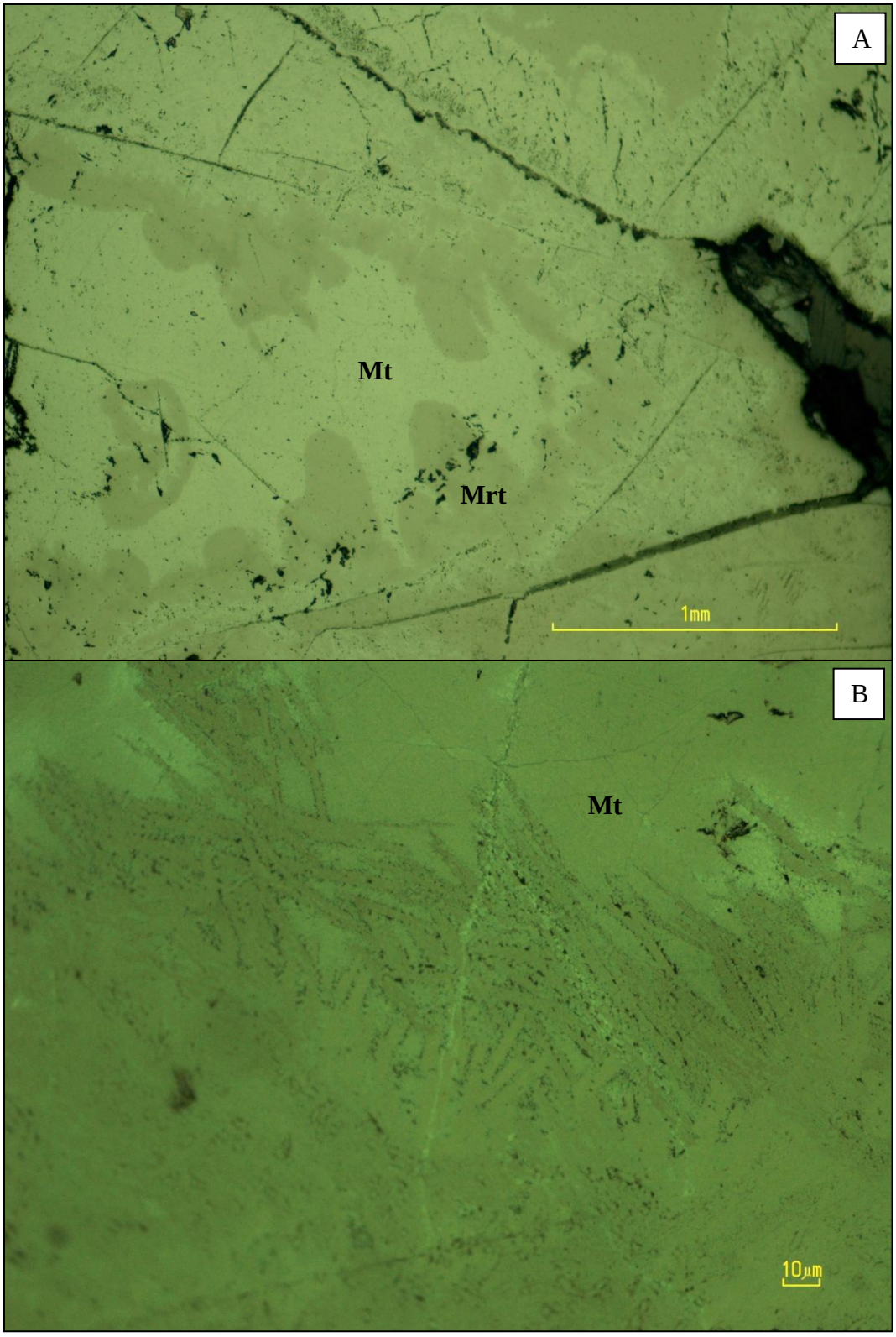

Figure 24. (A) A photomicrograph of the UZ8/17 sample showing a magnetite grain that has undergone an apparent martitization, as evidenced by the patchy nature. A few fractures are also visible within the image. Image was taken under 5x magnification. (B) A photomicrograph of the UZ8/17 sample showing needle-like crystal morphologies within the magnetite grains. Mt = Magnetite, Mrt = Martite.

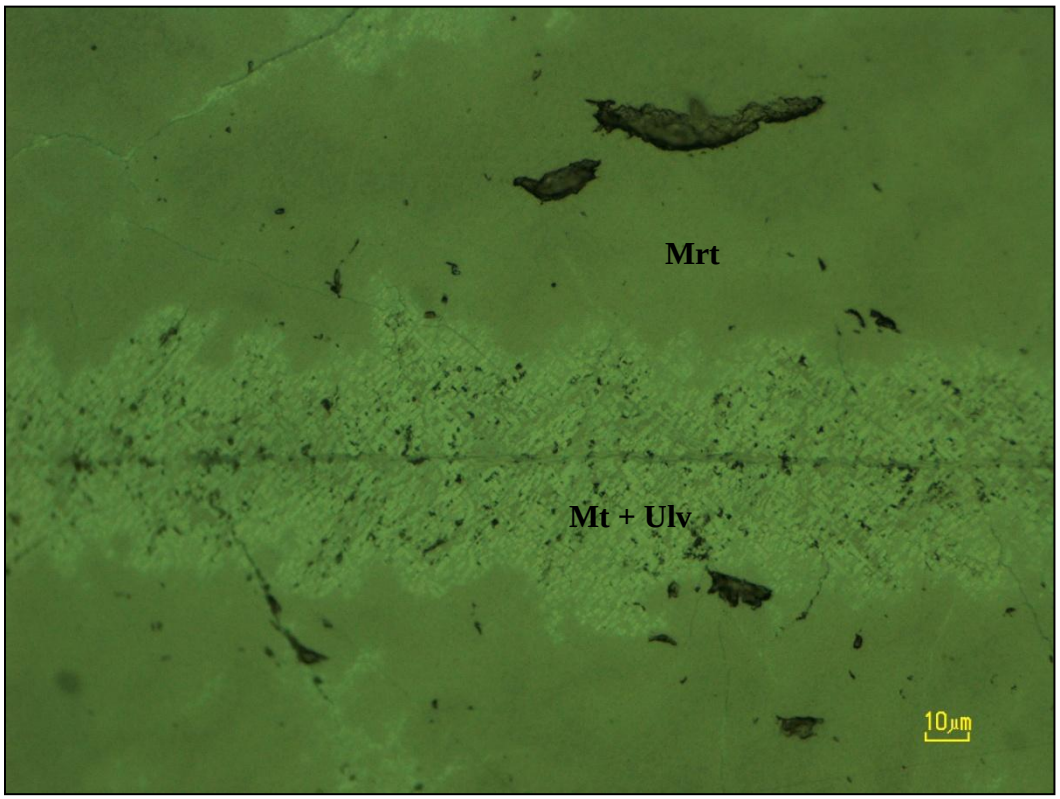

Figure 26. A photomicrograph of the UZ8/17 sample showing a thin vein surrounded by a cloth texture exsolution of ulvöspinel and magnetite. The surrounding magnetite grains have undergone martitization. Image was taken under 5x magnification. Mt = Magnetite, Mrt = Martite, Ulv = Ulvospinel.

Under plane-polarised light (PPL), the polished section shows very light grey colours for magnetite, pink-brown colours for ilmenite and martitized areas and dark grey colours for veins and fracture infilling. Under cross-polarised light (XPL), magnetite is isotropic, and ilmenite grains show a moderate anisotropy with dark grey colours. Most magnetite grains are anhedral with no recognisable crystal morphology, whereas ilmenite grains are generally anhedral with rounded edges. Well-developed cloth-texture exsolution of magnetite and ulvöspinel is dominant throughout the section, visible within figure 26 above. Sizes of the needle-like texture range from 10-40µm, visible within figure 25b. In general, the polished section is highly fractured with the occurrence of multiple veins and fracture infilling. Extensive martitization occurred within this sample, visible within figure 25a. Very few syntaxial veins are visible within this sample.

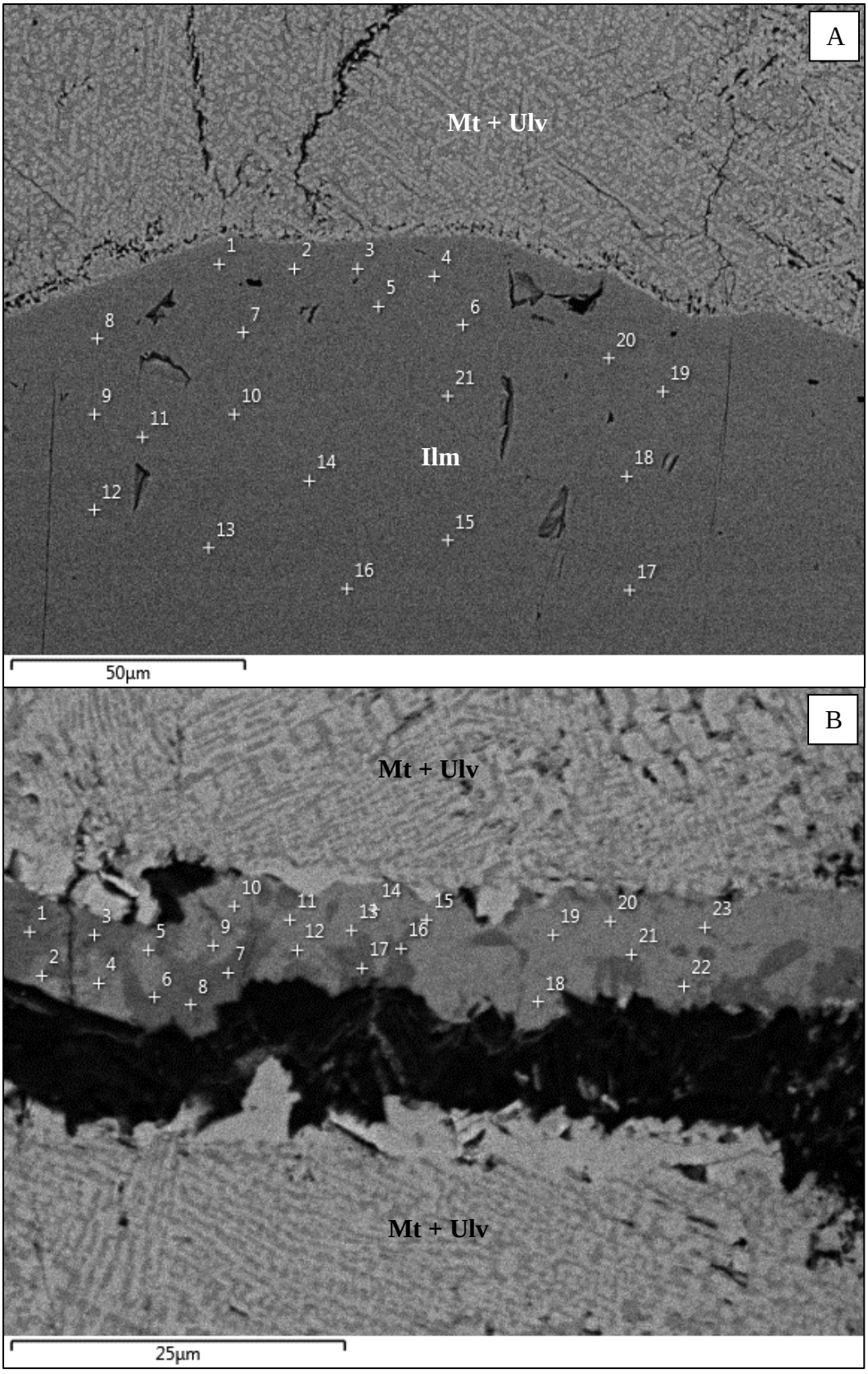

Figure 27. (A) A SEM image of the UZ8/17 sample showing an ilmenite grain adjacent to a magnetite grain with a well-developed cloth-texture exsolution of ulvöspinel and magnetite. (B) A SEM image of the UZ8/17 sample showing a large syntaxial vein surrounded by magnetite grains with a cloth-texture exsolution. Mt = Magnetite, Ilm = Ilmenite, Ulv = Ulvöspinel.

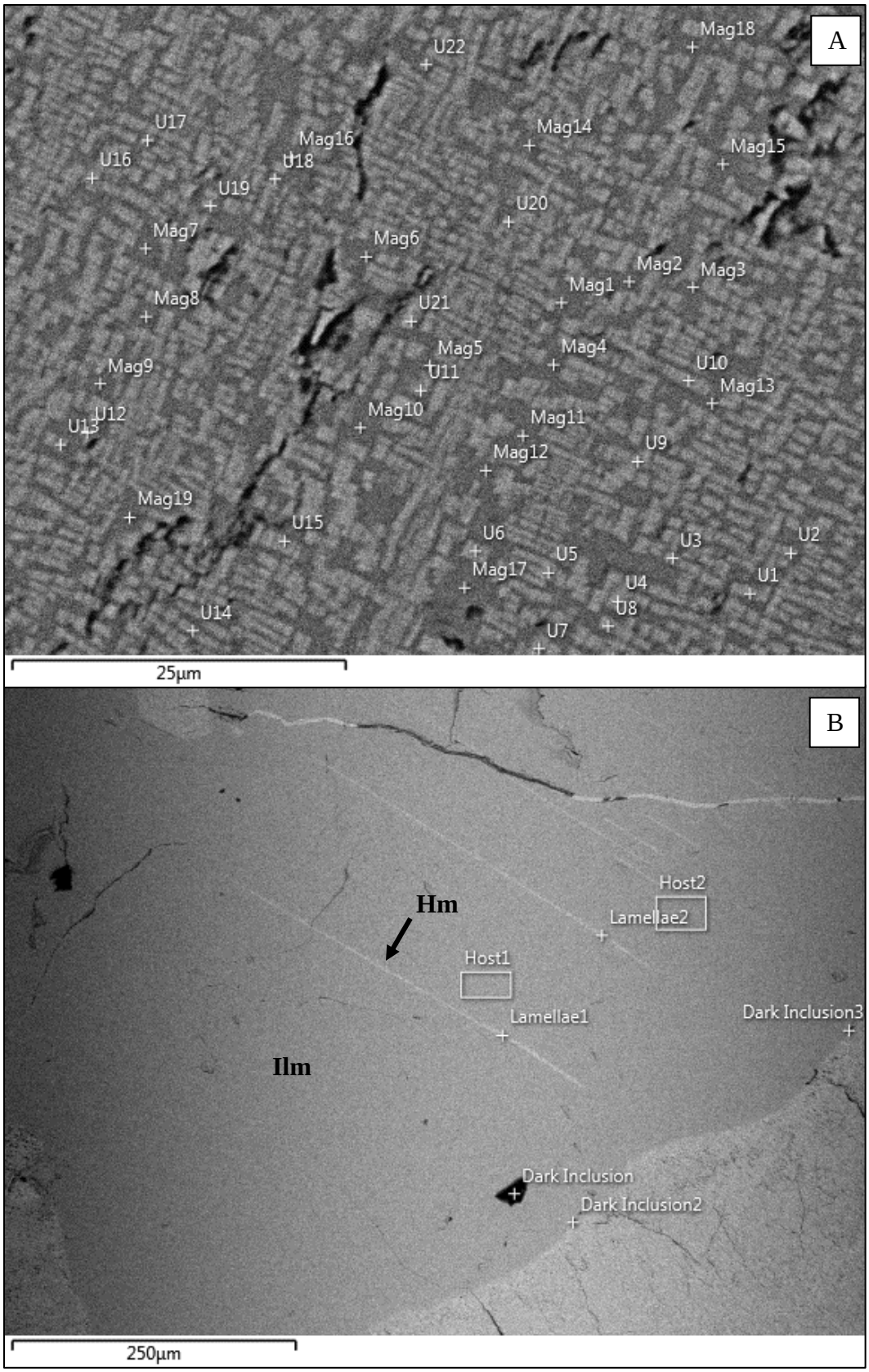

Figure 28. (A) A SEM image of the UZ8/17 sample showing a well developed cloth-texture exsolution of ulvöspinel and magnetite. (B) A SEM image of the UZ8/17 sample showing an ilmenite grain with exsolution lamellae of hematite. Ilm = Ilmenite, Hm = Hematite.

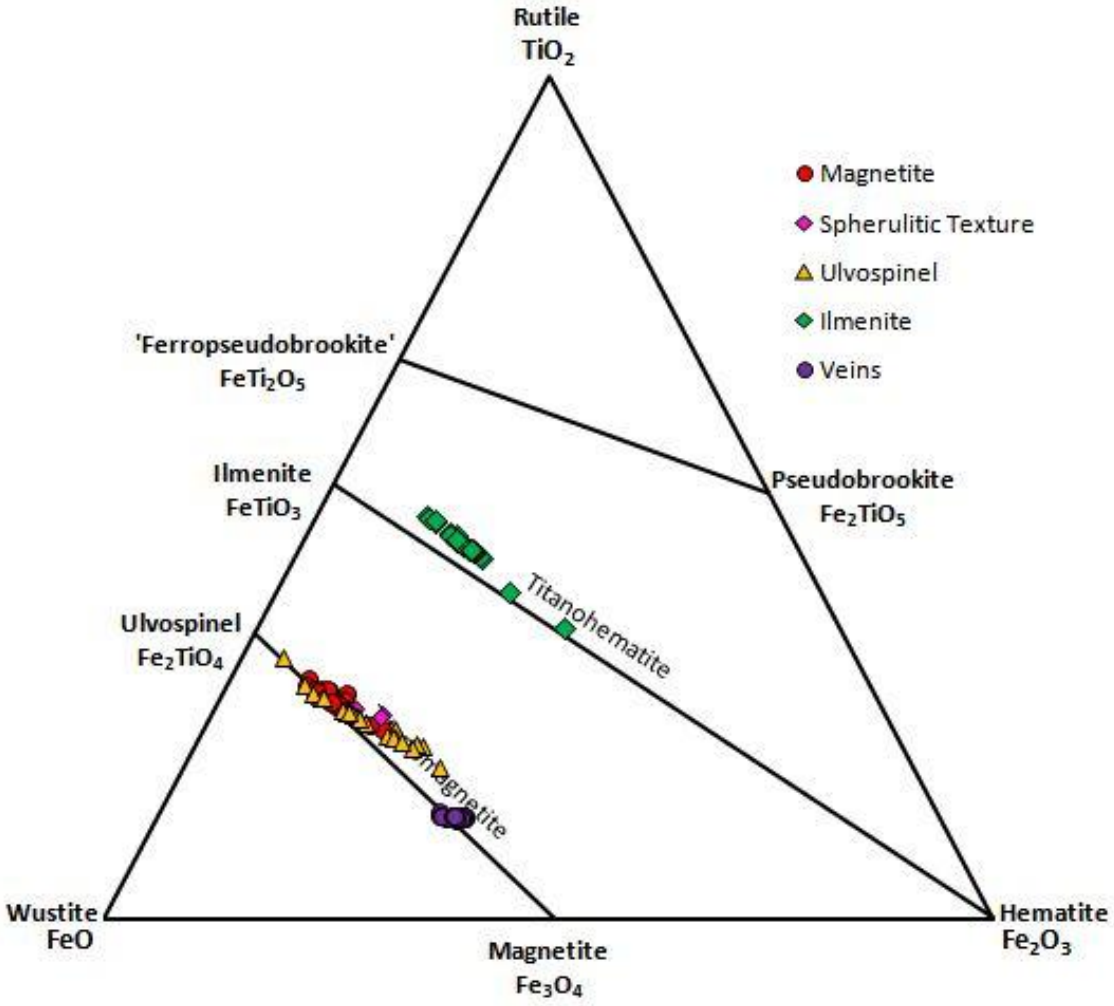

Figure 29. A FeO-TiO_2-Fe_2O_3 ternary diagram showing the respective concentrations of each element for various minerals and textures within the UZ8/17 sample. Linear trends are visible for ulvöspinel and ilmenite. Data from Table 4 and Appendix B.

Table 4: UZ8/17 Summary Table shows the various summarised data analyses for the UZ8/17 sample for each component.									
Component		**FeO (Wt-%)**	**Fe_2O_3 (Wt-%)**	**TiO_2 (Wt-%)**	**Al_2O_3 (Wt-%)**	**SiO_2 (Wt-%)**	**MgO (Wt-%)**	**Cr_2O_3 (Wt-%)**	**V_2O_3 (Wt-%)**
Magnetite Grains	Min.	55.25	8.34	21.56	3.03	0.43	0.67	-	-
	Mean	58.42	11.82	24.95	3.61	0.95	0.87	-	-
	Max.	60.41	19.30	27.34	4.02	1.30	1.01	-	-
Ulvöspinel Cloth Texture	Min.	53.06	8.28	19.59	2.82	0.85	-	-	-
	Mean	56.94	15.72	23.02	3.33	0.99	-	-	-
	Max.	60.67	23.68	26.52	3.82	1.09	-	-	-
Ilmenite Grains	Min.	34.01	14.87	40.49	1.36	1.54	2.39	-	-
	Mean	35.27	17.06	41.90	1.58	1.69	2.49	-	-
	Max.	36.24	19.83	43.07	1.76	1.98	2.90	-	-
Spherulitic (Fibrous) Texture	Min.	53.65	14.02	22.72	2.45	1.07	1.32	-	-
	Mean	55.92	15.75	23.54	2.94	1.32	1.32	-	-
	Max.	57.53	18.15	24.15	3.38	1.50	1.32	-	-
Syntaxial Veins	Min.	48.51	28.32	10.90	2.80	4.04	0.98	-	-
	Mean	49.38	30.45	11.22	3.28	4.74	1.08	-	-
	Max.	51.44	31.58	11.70	4.16	5.09	1.16	-	-

The mean composition of both magnetite grains and the ulvöspinel cloth-texture show similar concentrations in FeO, Fe_2O_3, TiO_2 and Al_2O_3 as seen in table 4. Magnetite shows a slightly higher concentration in FeO, TiO_2 and Al_2O_3, whereas ulvöspinel shows a slightly higher concentration in Fe_2O_3. Ilmenite grains show relatively lower concentrations of FeO and, with higher amounts of Fe_2O_3 and TiO_2. The ilmenite grains appear significantly depleted in Al_2O_3 when compared with the various other textural elements. The spherulitic texture shows a very similar concentration to that of the ulvöspinel cloth texture exsolution; however, the spherulitic texture appears depleted in Al_2O_3. The variation in concentration between the cloth texture and the spherulitic texture is less than one weight percent. The various veins that run through the sample show relative concentrations in Fe_2O_3 and SiO_2 and a relative depletion in TiO_2, when compared with the various other textural elements. The UZ8/17 sample analyses had no vanadium or chromium concentrations in any of the textural elements, with no magnesium within the ulvöspinel cloth texture exsolution.

Layer 21 North of the Steelpoort Fault (UZ21)

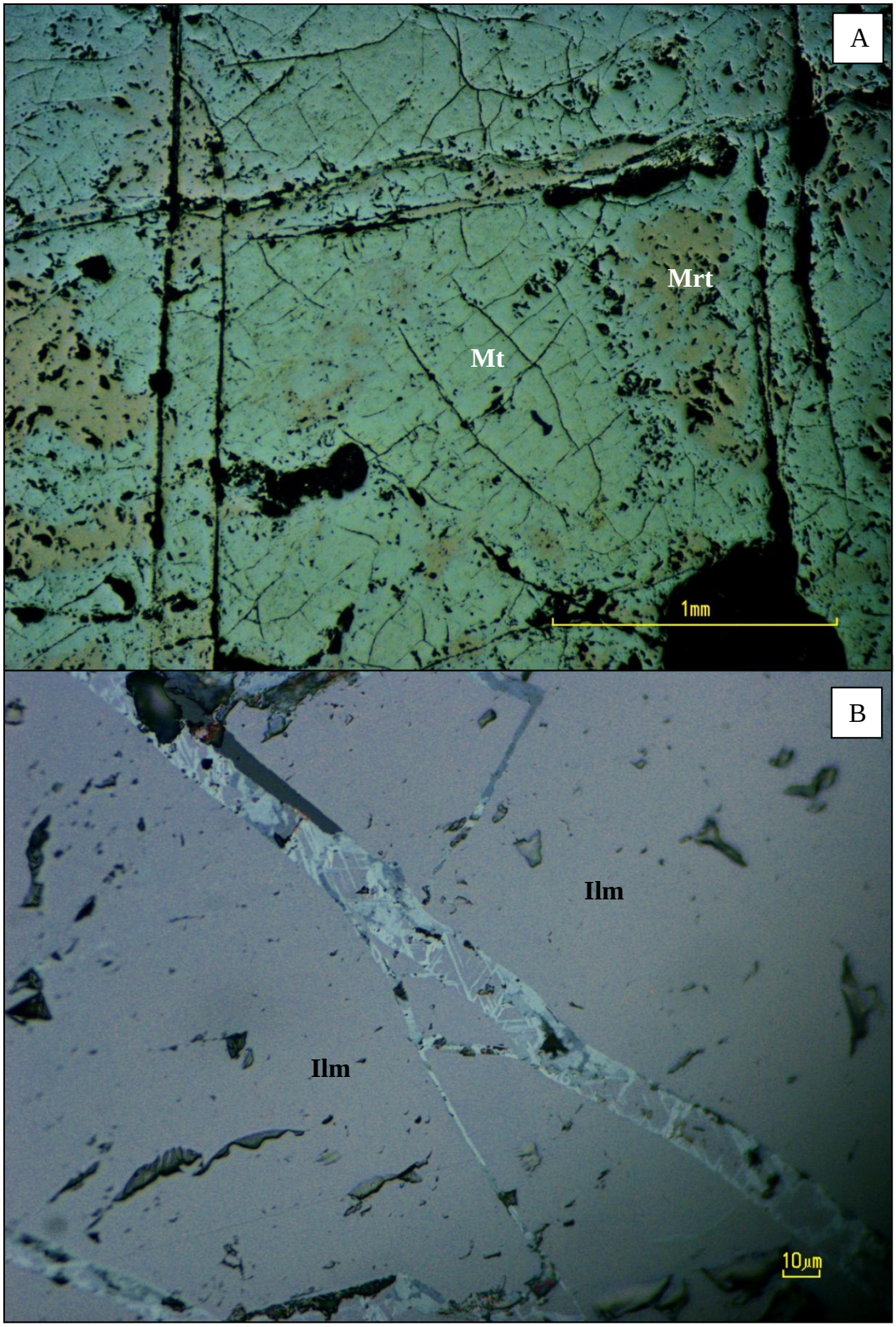

Figure 30. (A) A photomicrograph of the UZ21 sample showing anhedral magnetite grains with extensive fracturing, vein development and patchy martitization. Image was taken under 5x magnification. (B) A photomicrograph of the UZ21 sample showing a large vein cutting an ilmenite grain. The vein shows trellis exsolution. Image was taken under 50x magnification. Ilm = Ilmenite, Mt = Magnetite, Mrt = Martite.

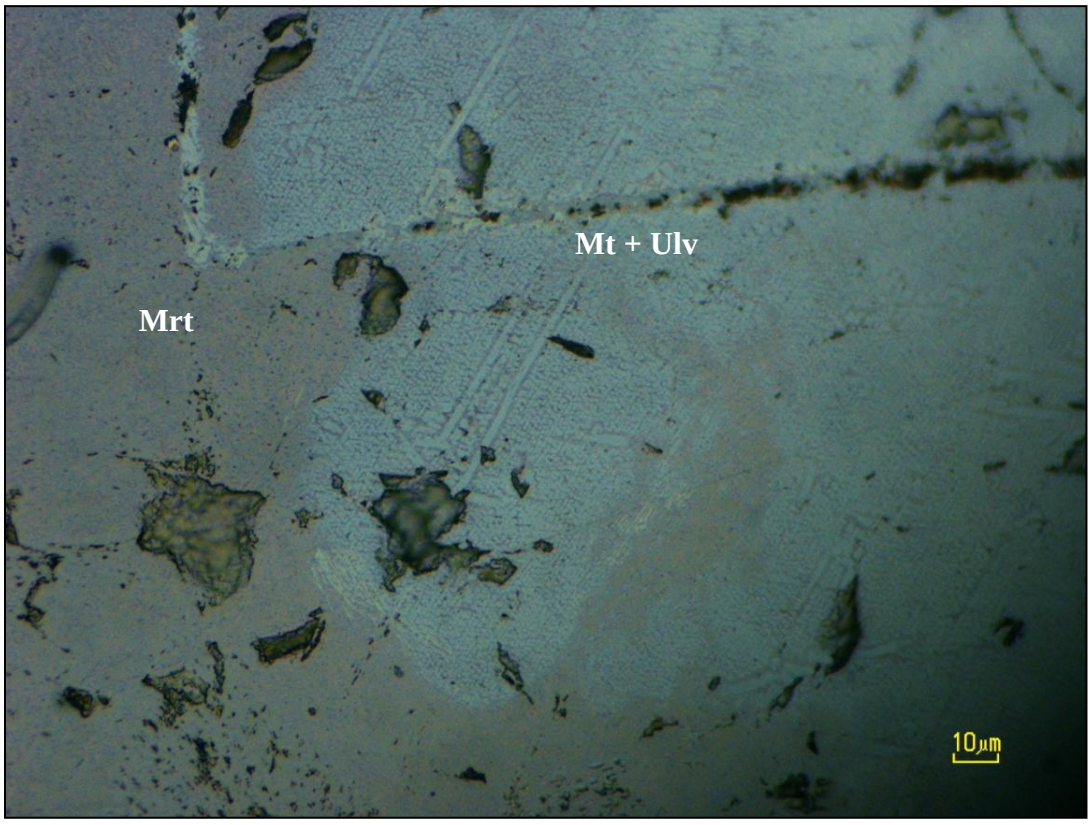

Figure 31. A photomicrograph of the UZ21 sample showing patchy martitization of a magnetite grain with well-developed cloth-texture exsolution of ulvöspinel and magnetite. Image was taken under 50x magnification.

Under plane-polarised light (PPL), the polished section shows very light grey colours for magnetite, pink-brown colours for ilmenite and martitized areas and dark grey colours for veins and fracture infilling. Under cross-polarised light (XPL), magnetite is isotropic, and ilmenite grains show a moderate anisotropy with dark grey colours. Magnetite grains have no crystal habit or recognisable crystal morphology, whereas ilmenite grains are generally subhedral with angular edges. A well-developed cloth texture exsolution of magnetite and ulvöspinel is dominant throughout the section as well as martitization, visible in figure 30a and figure 31 above. In general, the polished section is highly fractured with the occurrence of multiple syntaxial veins and fracture infilling, visible within figure 30b.

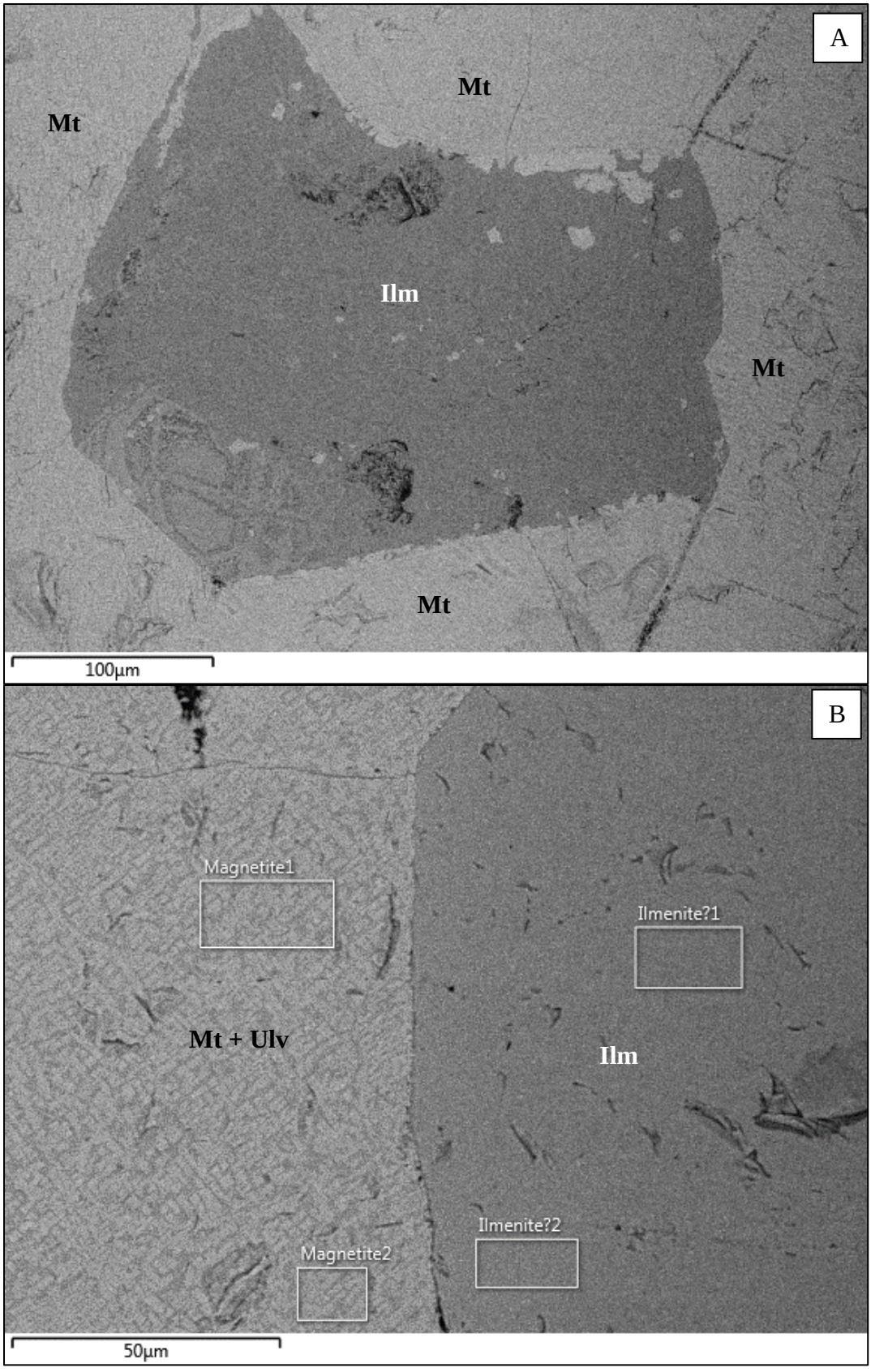

Figure 32. (A) A SEM image of the UZ21 sample showing an anhedral ilmenite grain surrounded by magnetite grains. The ilmenite grain appears to have inclusions of magnetite. (B) A SEM image of the UZ21 sample showing the magnetite-ilmenite boundary. No vein development is visible along the boundary. The magnetite grain has a well-developed cloth texture exsolution of ulvöspinel and magnetite. Mt = Magnetite, Ilm = Ilmenite, Ulv = Ulvöspinel.

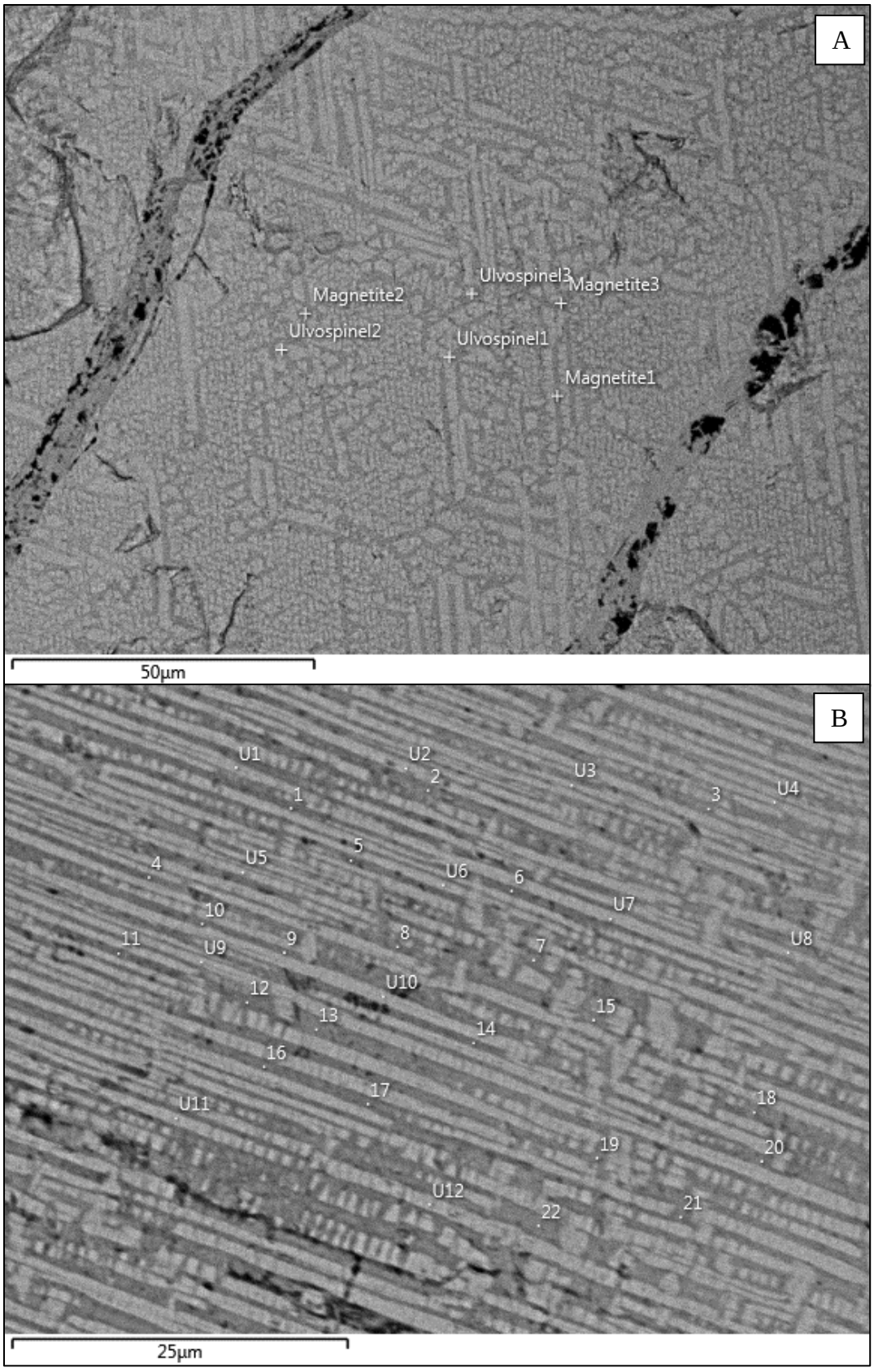

Figure 33. (A) A SEM image of the UZ21 sample showing a magnetite grain with a well-developed cloth-texture exsolution of ulvöspinel and magnetite as well as parallel vein development. (B) A SEM image of the UZ21 sample showing a close up image of the cloth-texture exsolution with preferential growth planes.

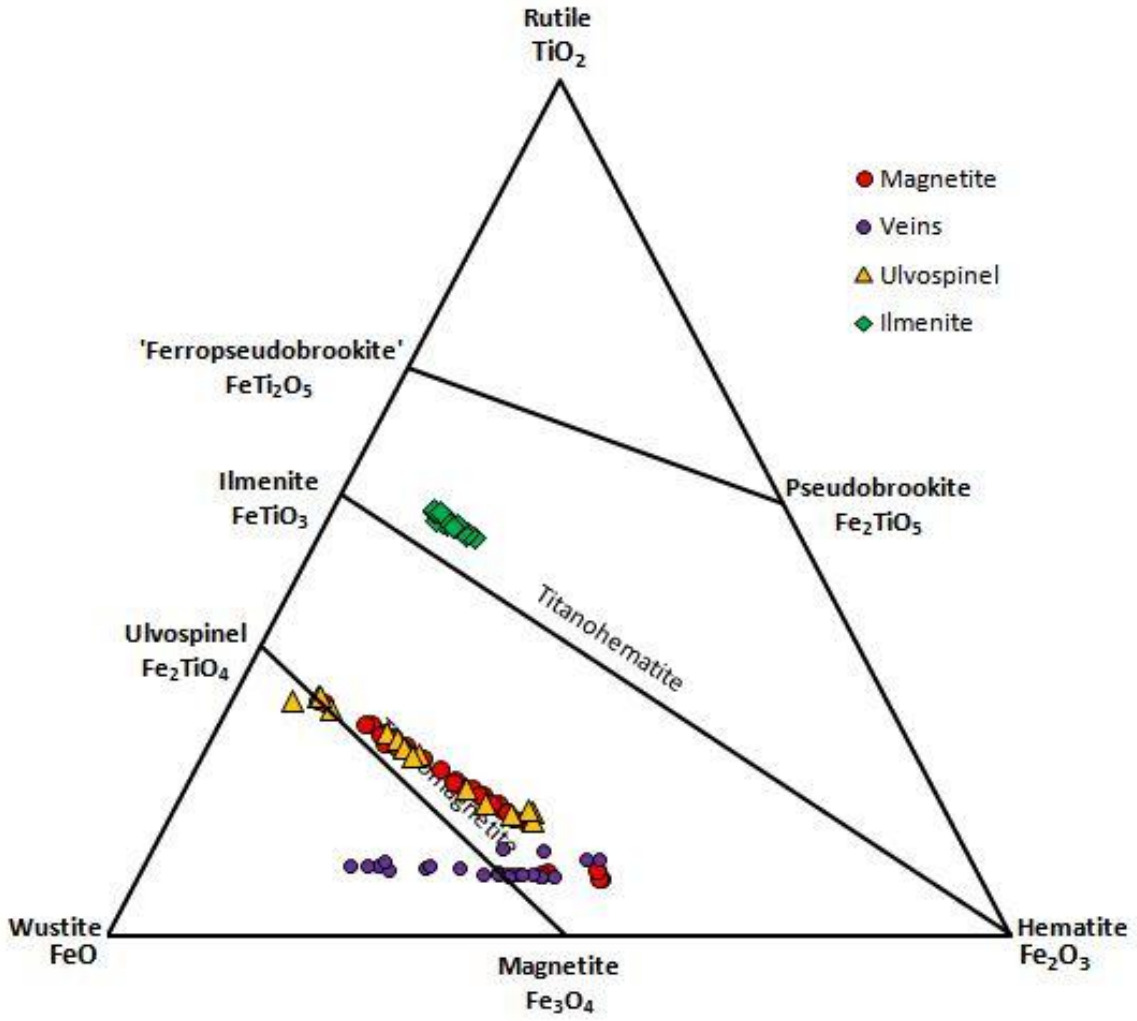

Figure 34. A FeO-TiO_2-Fe_2O_3 ternary diagram showing the relative concentrations of each element within various minerals and textural features of the UZ21 sample. Linear trends are visible for the trellis-exsolution, magnetite, ulvöspinel and ilmenite. Data from Table 5 and Appendix B.

Table 5: UZ21 Summary Table shows the various summarised data analyses for the UZ21 sample for each component.									
Component		**FeO (Wt-%)**	**Fe_2O_3 (Wt-%)**	**TiO_2 (Wt-%)**	**Al_2O_3 (Wt-%)**	**SiO_2 (Wt-%)**	**MgO (Wt-%)**	**Cr_2O_3 (Wt-%)**	**V_2O_3 (Wt-%)**
Magnetite Grains	Min.	40.36	8.98	6.40	2.12	0.42	-	0.43	0.43
	Mean	50.60	27.93	17.21	3.03	0.89	-	0.44	0.64
	Max.	60.58	49.08	26.39	5.20	2.94	-	0.45	0.87
Ulvöspinel Cloth Texture	Min.	43.96	6.18	13.14	2.24	0.21	0.82	-	0.57
	Mean	52.59	23.42	19.87	2.74	0.90	1.08	-	0.68
	Max.	61.71	38.94	26.96	3.57	2.18	1.30	-	0.90
Ilmenite Grains	Min.	34.68	10.56	44.92	0.58	-	2.36	-	-
	Mean	36.67	12.90	46.79	0.73	-	3.04	-	-
	Max.	38.25	16.42	48.10	0.96	-	3.36	-	-
Syntaxial Veins	Min.	38.62	18.20	6.35	12.49	6.71	-	-	-
	Mean	44.00	24.82	6.99	16.13	8.35	-	-	-
	Max.	53.60	45.13	7.24	18.45	10.26	-	-	-

The mean composition of both magnetite grains and the ulvöspinel cloth-texture show similar concentrations in FeO, Fe_2O_3, TiO_2 and Al_2O_3 as seen in table 5. Magnetite shows a slightly higher concentration in Fe_2O_3 and Al_2O_3, whereas ulvöspinel shows a slightly higher concentration in FeO and TiO_2. Ilmenite grains show relatively lower concentrations of FeO and Fe_2O_3, with significantly higher amounts of TiO_2. The ilmenite grains appear significantly depleted in Al_2O_3 when compared with the various other textural elements. The various veins that run through the sample show relative concentrations in Al_2O_3 and SiO_2 and a relative depletion in FeO and TiO_2 when compared with the various other textural elements. The UZ21 sample analyses show variation in concentration for various textural elements. Magnetite grains show no magnesium concentration; the ulvöspinel cloth texture exsolution shows no chromium concentration, the ilmenite grains show no silica, chromium or vanadium concentration and the various veins show no magnesium, chromium or vanadium concentration.

Layer 21 South of the Steelpoort Fault (UZ21B)

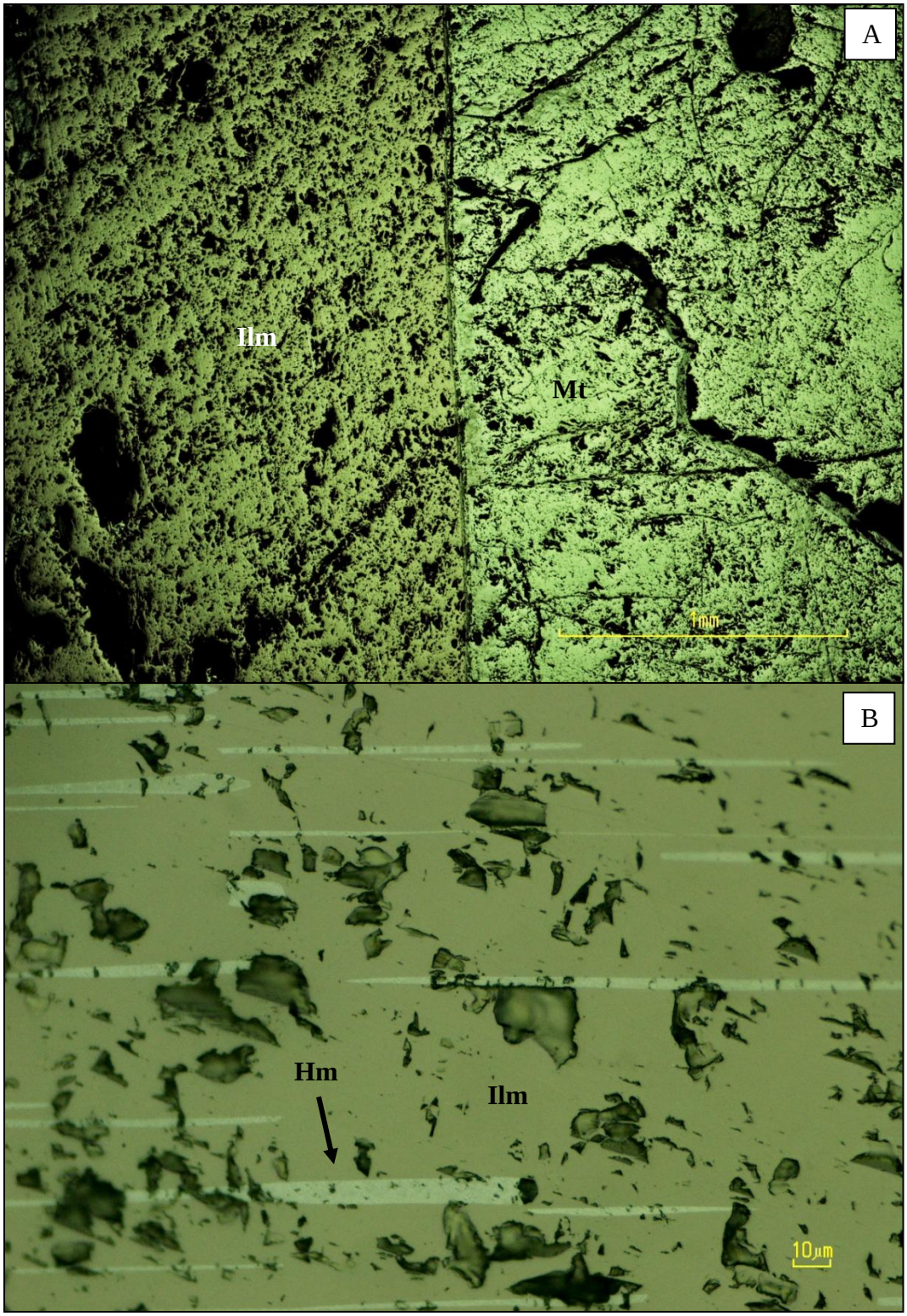

Figure 35. (A) A photomicrograph of the UZ21B sample showing the magnetite-ilmenite boundary. The sample is highly weathered, however, multiple fractures and vein development is still visible. Image was taken under 5x magnification. (B) A photomicrograph of the UZ21B sample, showing a close up of the ilmenite grain. Exsolution lamellae of hematite range in thickness from 2-10µm. Image was taken under 50x magnification. Ilm = Ilmenite, Mt = Magnetite, Hm = Hematite.

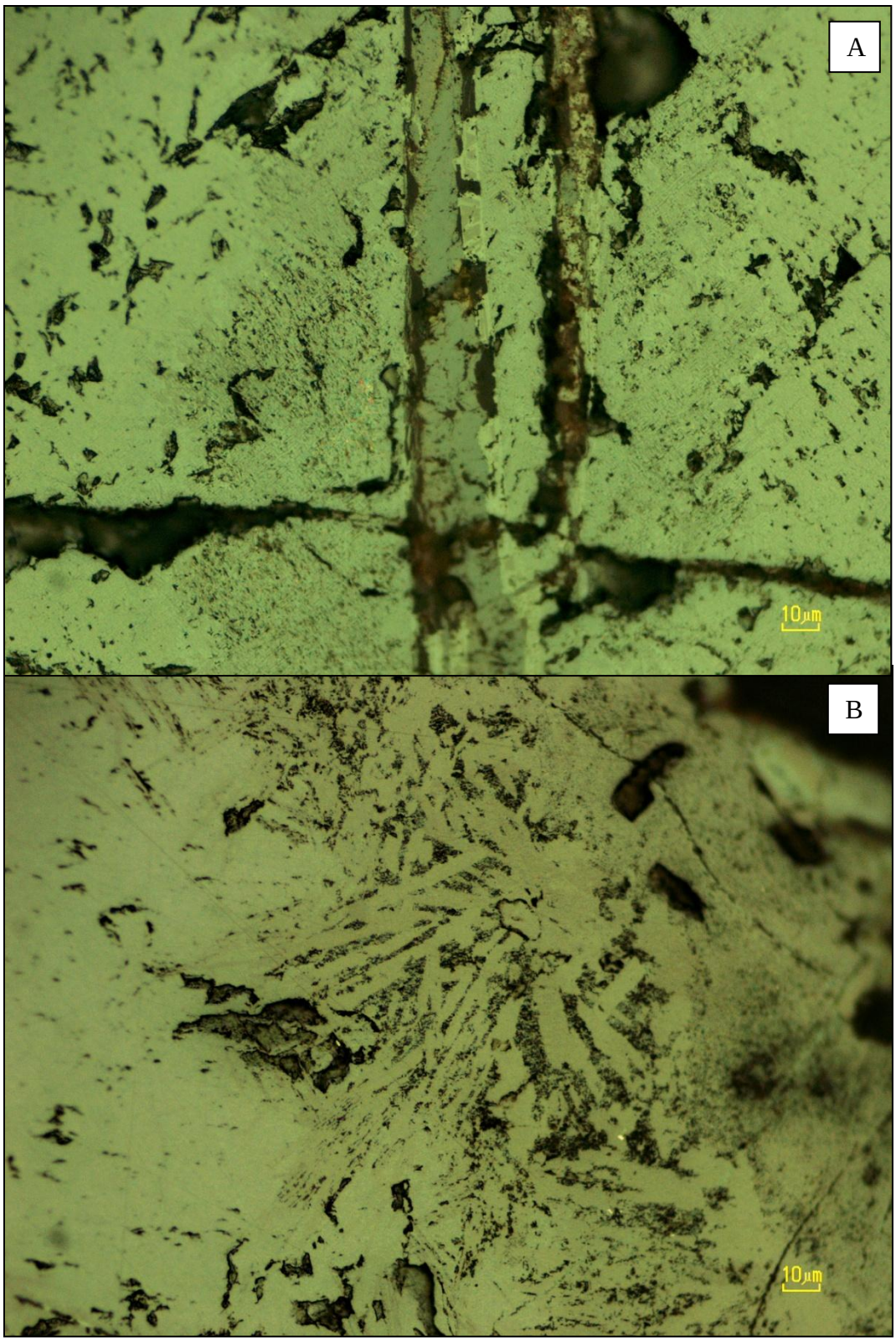

Figure 36. (A) A photomicrograph showing vein development within the UZ21B sample. Radiating oxide needles are visible along the vein. The edge of the vein also appears to have a trellis exsolution texture. Image taken under 20x magnification. (B) A photomicrograph of the UZ21B sample showing a close up of the radiating oxide needles, the edges of which appear to show alteration. Image was taken under 50x magnification.

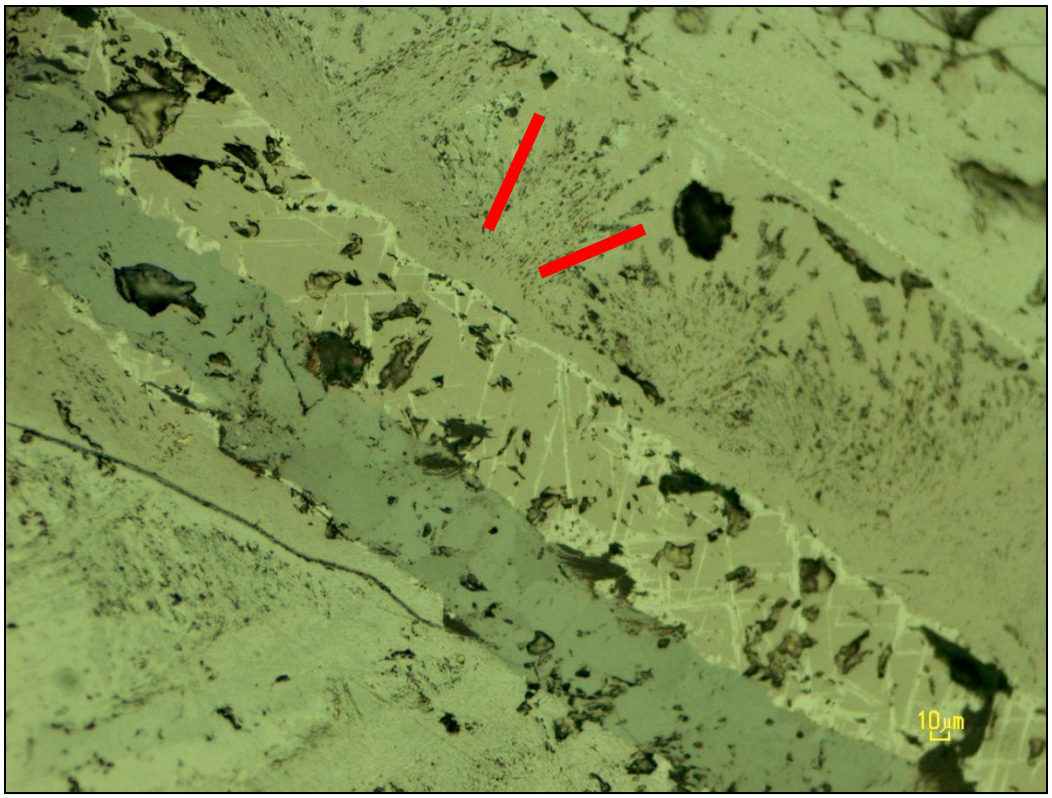

Figure 37. A photomicrograph of the UZ21B sample showing the two generations of vein development as well as the radiating, fibrous oxide needles. Image was taken under 20x magnification. Needles range in size from 10-50µm.

Under plane-polarised light (PPL), the polished section shows very light grey colours for magnetite, pink-brown colours for ilmenite and dark grey colours for veins and fracture infilling. Under cross-polarised light (XPL), magnetite is isotropic, and ilmenite grains show a moderate anisotropy with dark grey colours. Most magnetite grains are anhedral with no recognisable morphology, whereas ilmenite grains are generally elongated and anhedral. Certain ilmenite grains show thin lamellae of hematite exsolution. A poorly developed cloth-texture exsolution of magnetite and ulvöspinel occurs throughout the section. Adjacent to multiple veins in the section is areas of radial oxide needles, originating from the vein itself as seen in figure 37 above. In general, the polished section is highly fractured with the occurrence of multiple syntaxial veins and fracture infilling, visible within figure 36a and b.

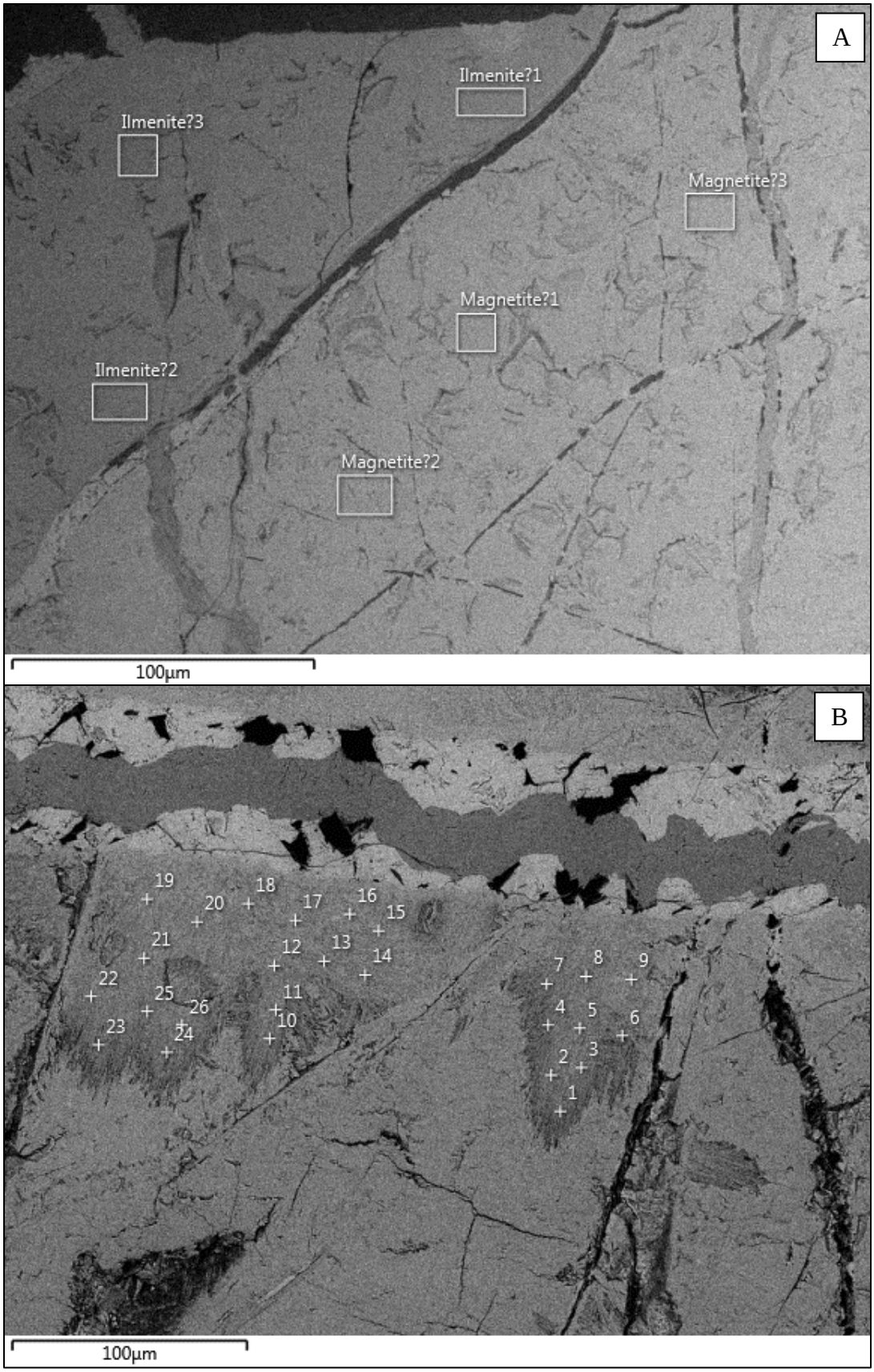

Figure 38. (A) A SEM image of the UZ21B sample showing magnetite-ilmenite boundary showing vein development across and through the various anhedral grains. (B) A SEM image of the UZ21B showing the development of a syntaxial vein as well as radiating oxide needles originating from the vein itself.

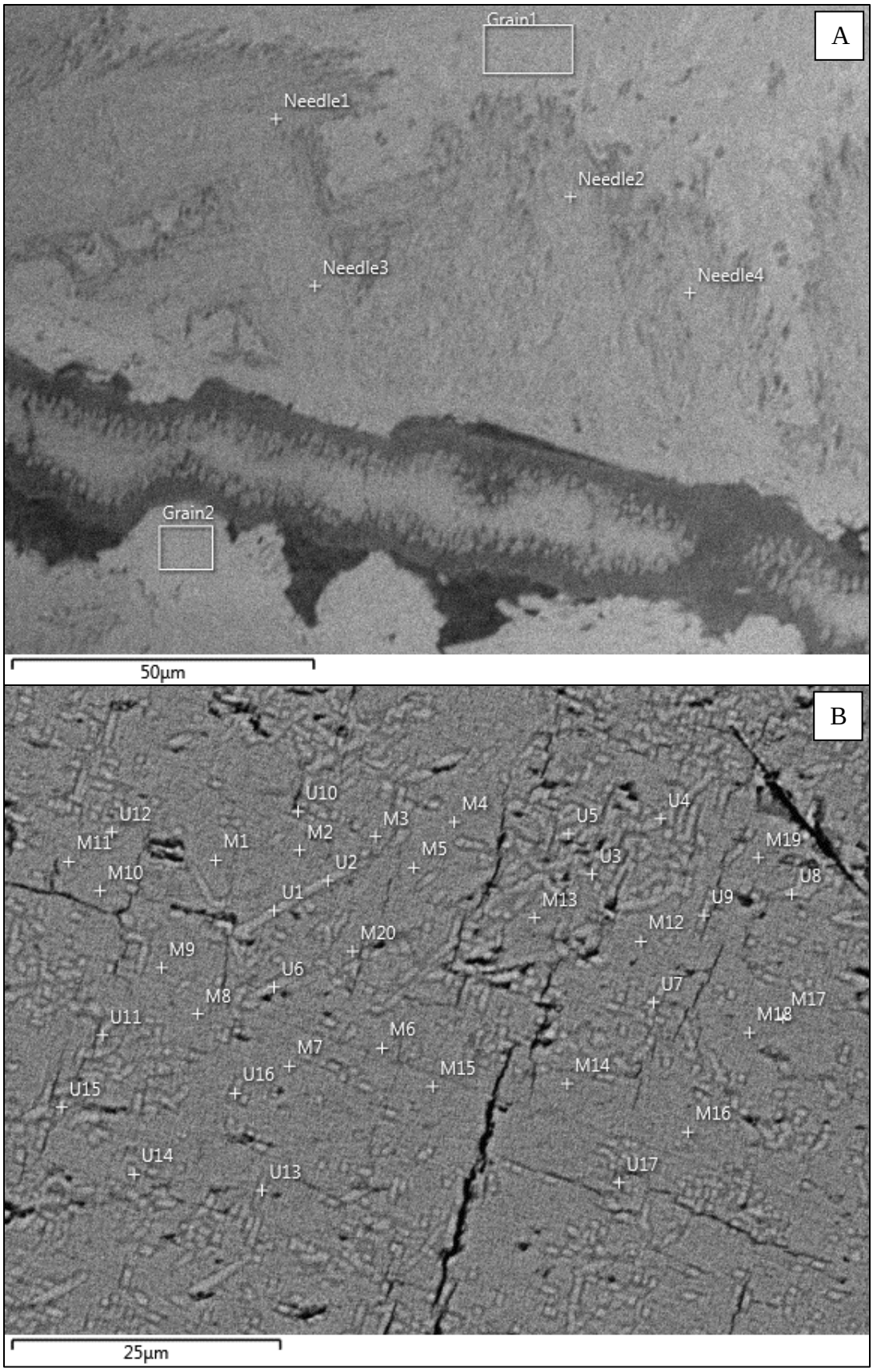

Figure 39. (A) A SEM image of the UZ21B sample showing a close up of the radiating needles adjacent to a syntaxial vein. The needles appear to have a fibrous nature. (B) A SEM image of the UZ21B sample showing poorly developed cloth-texture exsolution of ulvöspinel and magnetite.

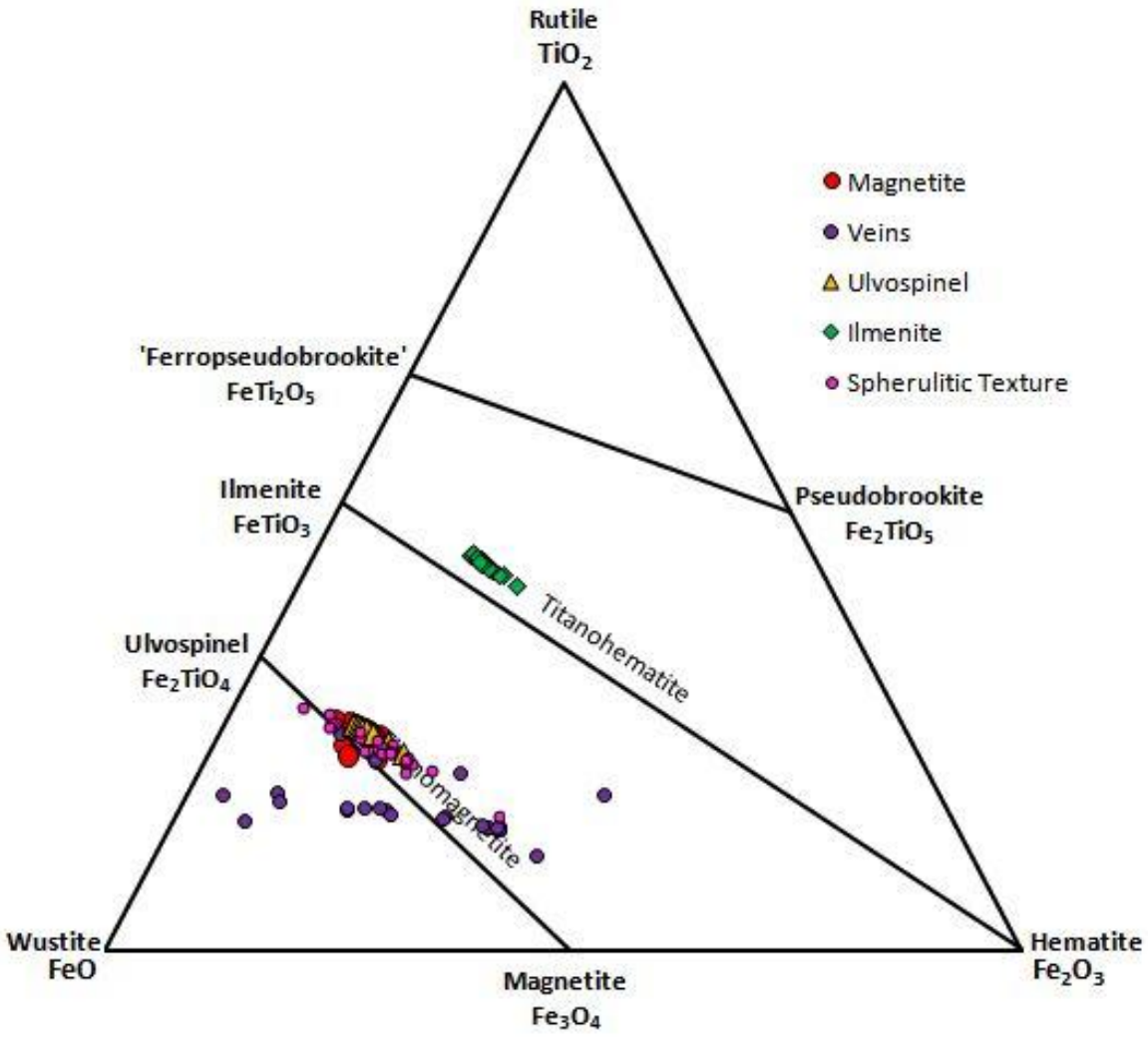

Figure 40. A FeO-TiO_2-Fe_2O_3 ternary diagram showing the relative concentrations of each element within various minerals and textural features of the UZ21B sample. Linear trends are visible for the spherulitic texture, magnetite, ulvöspinel veins and ilmenite. Data from Table 6 and Appendix B.

Table 6: UZ21B Summary Table shows the various summarised data analyses for the UZ21B sample for each component.									
Component		**FeO (Wt-%)**	**Fe_2O_3 (Wt-%)**	**TiO_2 (Wt-%)**	**Al_2O_3 (Wt-%)**	**SiO_2 (Wt-%)**	**MgO (Wt-%)**	**Cr_2O_3 (Wt-%)**	**V_2O_3 (Wt-%)**
Magnetite Grains	Min.	55.53	11.34	20.70	2.45	0.43	-	-	-
	Mean	57.23	15.05	24.38	2.96	1.32	-	-	-
	Max.	59.29	18.23	25.85	4.39	2.81	-	-	-
Ulvöspinel Cloth Texture	Min.	54.66	13.38	22.36	2.46	-	-	0.44	-
	Mean	56.76	15.66	24.54	2.80	-	-	0.46	-
	Max.	57.83	20.53	25.56	3.24	-	-	0.59	-
Ilmenite Grains	Min.	31.78	15.62	39.61	1.94	1.10	2.74	-	-
	Mean	33.70	17.64	41.55	2.41	1.59	3.12	-	-
	Max.	34.69	22.28	42.60	2.91	2.20	3.58	-	-
Spherulitic (Fibrous) Texture	Min.	47.74	7.14	14.85	2.22	0.84	0.83	0.29	-
	Mean	55.31	17.37	22.16	2.92	1.41	1.19	0.42	-
	Max.	61.30	33.93	26.51	4.20	2.38	1.68	0.58	-
Syntaxial Veins	Min.	45.31	11.36	10.55	2.02	0.87	-	-	-
	Mean	51.17	26.86	14.77	5.15	2.24	-	-	-
	Max.	56.77	39.14	22.36	11.34	6.06	-	-	-

The mean composition of both the magnetite grains and the ulvöspinel cloth-texture show similar concentrations in FeO, Fe_2O_3, TiO_2 and Al_2O_3 as seen in table 6. Magnetite shows a slightly higher concentration in FeO and Al_2O_3, whereas ulvöspinel shows a slightly higher concentration in Fe_2O_3 and TiO_2. Ilmenite grains show relatively lower concentrations of FeO and Fe_2O_3, with significantly higher amounts of TiO_2. The ilmenite grains appear significantly depleted in Al_2O_3 when compared with the various other textural elements. The spherulitic texture shows a very similar concentration to that of the ulvöspinel cloth texture exsolution; however, the spherulitic texture appears depleted in TiO_2 and slightly enriched in Fe_2O_3 and Al_2O_3. The various veins that run through the sample show relative concentrations in Fe_2O_3, Al_2O_3 and SiO_2 and a relative depletion in TiO_2, when compared with the various other textural elements. The UZ21B sample analyses show variation in concentration for various textural elements. Magnetite grains show no magnesium, chromium or vanadium concentration; the ulvöspinel cloth texture exsolution shows no silica, magnesium or vanadium concentration, the ilmenite grains show no chromium or vanadium concentration and the various veins show no magnesium, chromium or vanadium concentration.

Ternary Diagrams

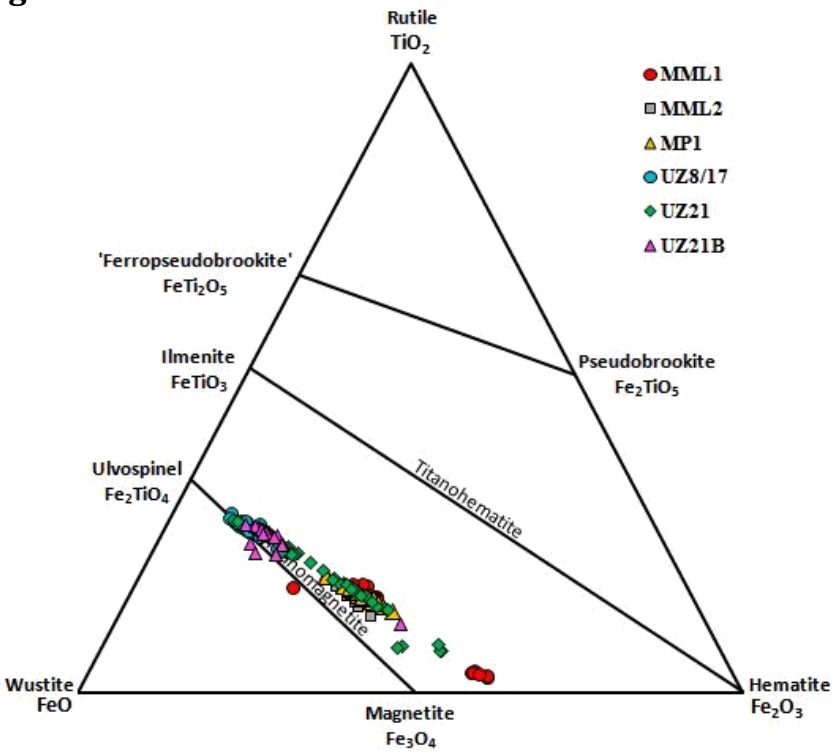

Figure 42. A FeO-TiO_2-Fe_2O_3 ternary diagram showing the relative concentrations of each element within magnetite of the various research samples. Linear trends are visible for the for all of the samples. Data is summarised from each ternary and is available in appendix B.

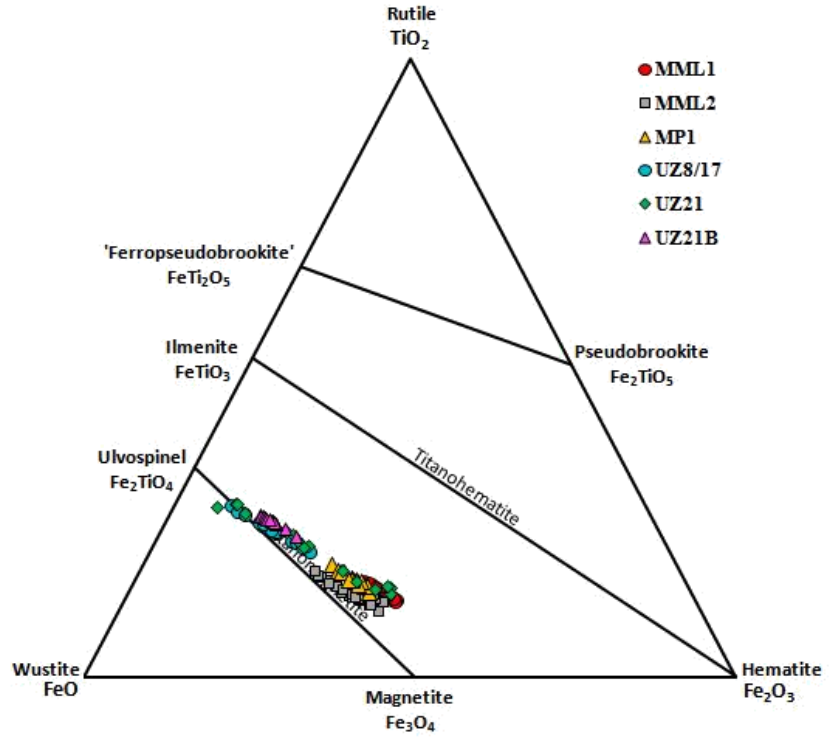

Figure 41. A FeO-TiO_2-Fe_2O_3 ternary diagram showing the relative concentrations of each element within ulvöspinel of the various research samples. Linear trends are visible for the for all of the samples. Data is summarised from each ternary and is available in appendix B.

Chapter 5: Discussion

Exsolution Textures

According to Duchesne (1970), essential characteristics of titaniferous magnetites lie within their chemical compositions. One of the more extensive studies carried out showed that R_3O_4 (magnetite), R_2TiO_4 (ulvöspinel) and $RTiO_3$ (ilmenite) classifies the composition of titaniferous magnetite (Duchesne, 1969). The number of occupancies of different cations in different positions is an indication of different chemical environments of magnetite formation (Zhang et al., 2012). Therefore, textures relating to compositions of magnetite can provide a better picture of deformation relative to mineralisation.

Intergrowths of ilmenite occur within magnetite and exist between two extremes, which include the cloth microtexture and the trellis microtexture (with a "sandwich" variant) (Duchesne, 1970). The cloth intergrowth is also characteristic of the ulvöspinel exsolutions in the magnetite as seen by Ramdohr (1953) and Anderson (1968). These lamellae usually lie on {100}, with inter-lamellar magnetite-rich blocks (Price, 1980). The exsolution microstructure only develops on a small scale, due to the slow rate of the kinetic processes involved in unmixing at the solvus temperature. Within the ulvöspinel cloth microtexture, it is the coarse {100} lamellae pattern which gives the grain the appearance of cloth (Ramdohr, 1953). Experimental work conducted by Lindsley (1962), Vincent et al. (1957) and Basta (1960), showed ulvöspinel forms a complete solid solution with magnetite at temperatures above 600°C. Ulvöspinel forms part of the inverse spinel group, which implies that some of the R^{3+} cations occupy the tetrahedral sites and the rest, along with the R^{2+} cations, occupy the octahedral site. During cooling, ulvöspinel forms exsolution lamellae along the {100} planes of the magnetite. According to Verhoogen (1962), pure ulvöspinel is only stable under very low oxygen fugacity conditions. The {100} lamellae of the cloth microtexture generated by exsolution of ulvöspinel occur at a temperature below the magnetite-ulvöspinel solvus. The ulvöspinel completely transforms into ilmenite micro-lamellae through in situ oxidation. The reaction that occurs during this process is this:

$$\underset{\text{(Ulvöspinel)}}{6\ Fe_2TiO_4} + O_2 \rightarrow \underset{\text{(Ilmenite)}}{6\ FeTiO_3} + \underset{\text{(Magnetite)}}{2\ Fe_3O_4} \qquad (1)$$

This equation implies there is a simple addition of oxygen to the magnetite without a reasonable change in volume (Duchesne, 1970). The titaniferous magnetites in which all grains of magnetite show the cloth-microtexture are rich in titanium, however, not all Ti-rich magnetites necessarily show this microtexture. Although all the samples within this study exhibit the cloth microtexture, the abundance of the cloth microtextures vary from sample to sample. Samples MML1, MML2 and MP1 all exhibit the cloth microstructure ranging in size from 1μm to 2μm wide. Samples UZ8/17 and UZ21 exhibit well-developed cloth microtexture ranging in size from 3μm to 5μm wide. The only sample with poorly developed cloth-microtexture is that of UZ21B. The poorly developed microtexture indicates that the degree of oxidation occurring across all the samples differs. The respective ternary diagrams for each sample indicate the degree of oxidation. Figure 6 shows that the magnetite and ulvöspinel in MML1 underwent low degrees of oxidation evidenced by the small variation in FeO and Fe_2O_3 ratios of the ternary diagram. The ternary diagram of the solid solution series shows the degree of oxidation from left

to right within the diagram. Low degree of oxidation results in a poorly formed cloth microtexture.

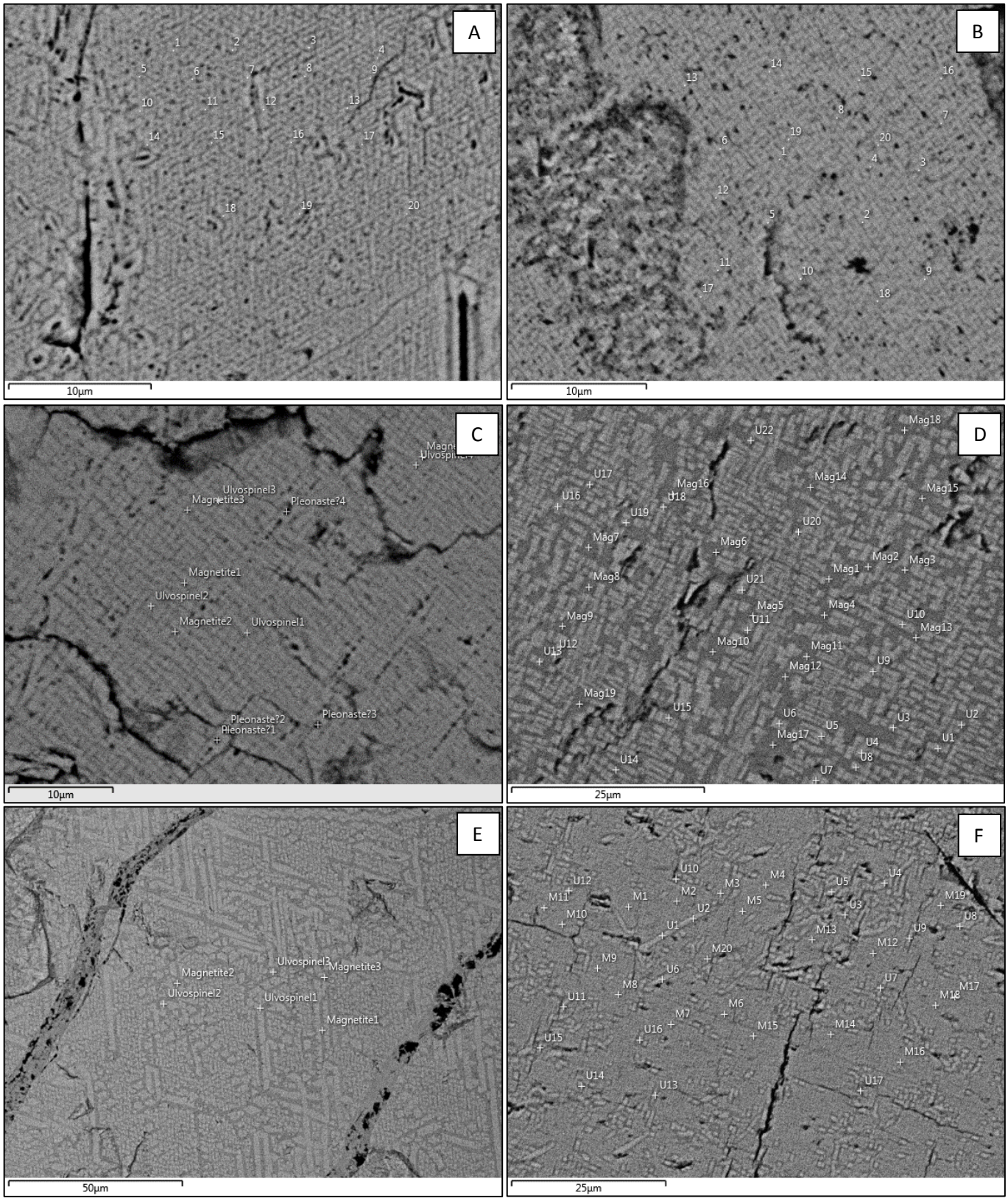

Figure 43. Various images showing the variation in cloth microtexture development across the different samples. (A) MML1 (B) MP1 (C) MML2 (D) UZ8/17 (E) UZ21 and (F) UZ21B.

Samples of MML2 and MP1 show a slightly higher degree of oxidation as evidenced by Figure 15 and Figure 22. Figure 44B and 44C show a slightly more developed cloth microtexture when compared to that of MML1 in A. Samples UZ8/17, and UZ21 show the most well-developed cloth microtexture, largely due to the higher degree of oxidation as seen in Figure 29 and Figure 35. The UZ21B sample shows an extremely poor cloth microtexture, evidenced by Figure 43F, which shows that little to no oxidation occurred.

Within the trellis microtexture, the {111} ilmenite lamellae form a distinctly thicker network with regular multidirectional growth (Duchesne, 1970). When an aluminium-rich spinel is present, like that found within this study, these ilmenite lamellae are dotted with spinel micro-crystals as seen in Figure 44 below. When the network of trellis microtexture surrounds magnetite, the network may appear on either a background of homogeneous magnetite or a cloth-microtexture (Duchesne, 1970). The surrounding network illustrates that both the cloth-microtexture and the trellis-microtexture can coexist within the same mineral grain.

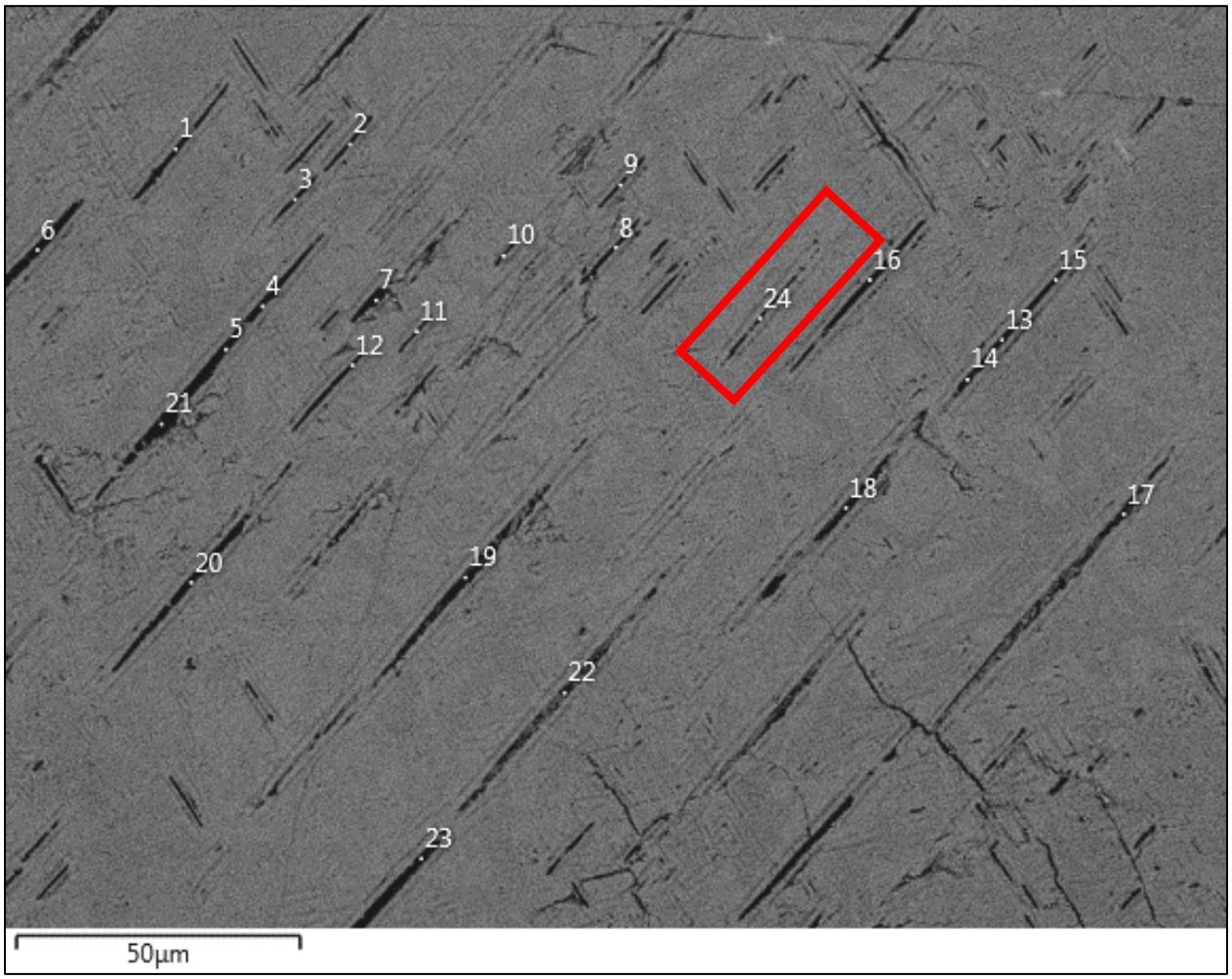

Figure 44. A SEM image showing a trellis microtexture surrounded by a cloth microtexture. The red box aims to indicate small aluminium-rich spinel micro-crystals. The image is taken from sample MP1.

According to Duchesne (1970), when the magnetite contains more than 2 wt-% (weight percent) Al_2O_3, two generations of lens-shaped exsolution are visible. Within the cloth microtexture, surrounding the first generation of spinel lenses are box-like structures. Figure 42 of the MP1 sample above shows these box-like structures.

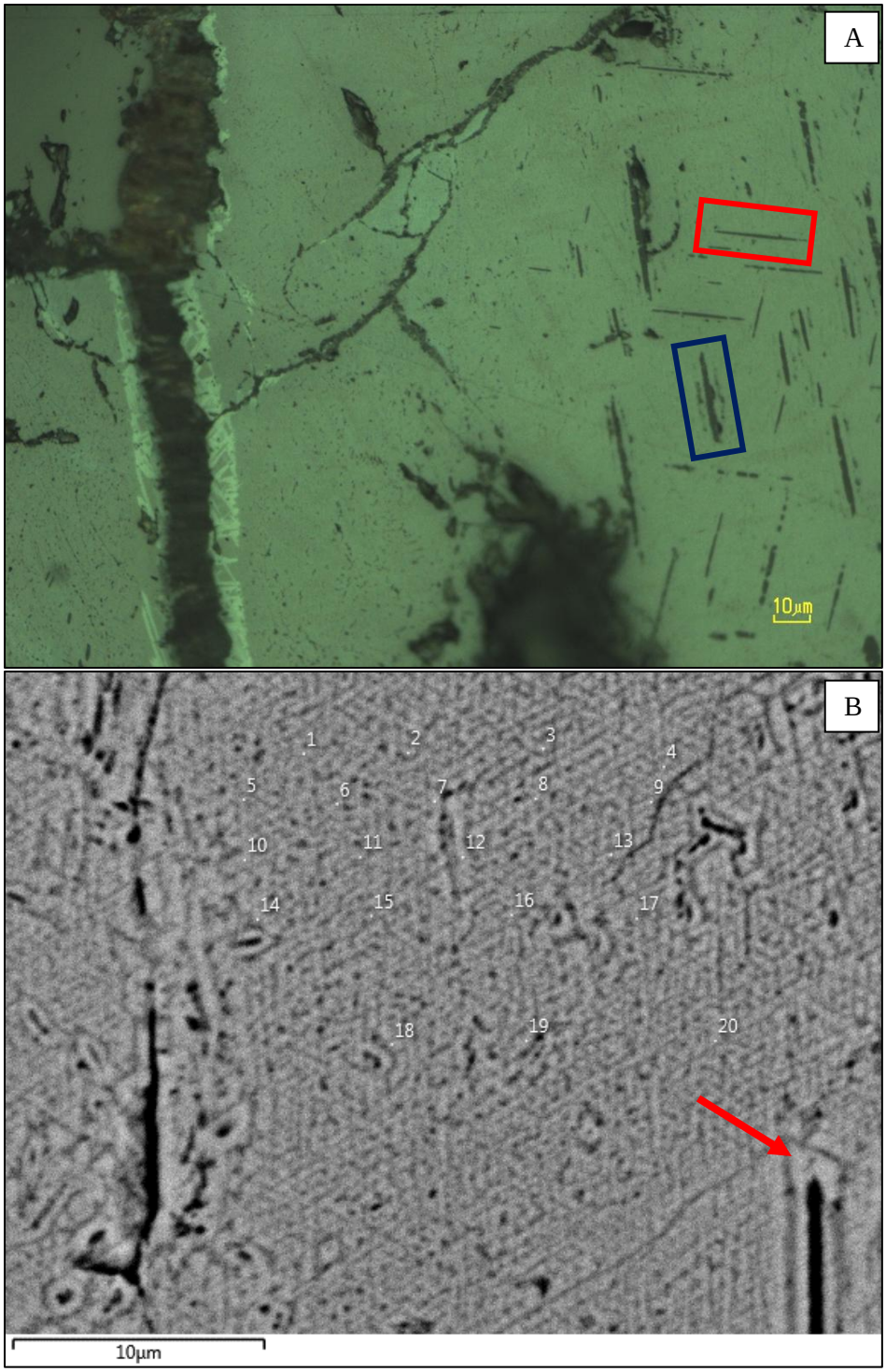

Figure 45. (A) A photomicrograph of the MML2 sample. The red box shows one generation of an aluminium-rich ilmenite lens without a box-like structure. The blue box shows another generation of the aluminium-rich spinel lens with a box structure surrounding it. (B) A SEM image showing a close up of the box-like structure surrounding the aluminium-rich spinel lens.

Different modes of oxidation of ulvöspinel may account for the diversity of the microtextures observed. According to Duchesne (1970), one can assume that oxidation of ulvöspinel occurs over a wide range of temperatures and that the temperature at which the process begins may be above or below the magnetite-ulvöspinel solvus. Oxidation takes place above and below the solvus, as well as across a range of temperatures. According to Duchesne (1970), if oxidation begins at a relatively low sub-solvus temperature, ilmenite forms under difficult diffusion conditions, occurring where ulvöspinel previously exsolved. If oxidation occurs at a higher sub-solvus temperature, Fe- and Ti- liberated by the oxidation of ulvöspinel, according to equation 1, migrate towards the {111} planes to form trellis lamellae of ilmenite. If oxidation begins at a super-solvus temperature, the ulvöspinel dissolved in the magnetite is oxidised, and a (super-solvus) ilmenite is formed along the {111} planes to produce a trellis lamellae. Duchesne (1970) speculated that super-solvus oxidation related to the total amount of ulvöspinel contained in the magnetite results in a trellis microtexture on a homogeneous background of magnetite. If partial super-solvus oxidation takes place, two possible scenarios may occur; either (1) fast diffusion maintains a uniform concentration of both Fe and Ti within the non-oxidized regions of the magnetite, down to the solvus or (2) a concentration gradient appears before reaching the solvus (Duchesne, 1970). According to Duchesne (1970), the varieties of microtextures found within titaniferous magnetites occur through oxidation initiating at different temperatures relative to those temperatures of the magnetite-ulvöspinel solvus. The trellis microtextures form through oxidation initiating at super-solvus temperatures whereas the cloth microtexture is entirely oxidised sub-solvus.

Martitization

There appears to be very little information regarding the process and occurrence of martitization within titaniferous magnetites. Martitization is essentially the oxidation of magnetite and subsequent replacement by hematite or martite (pseudomorph of hematite). The process occurs under moderate-temperature, hydrothermal oxidation. According to Mucke and Cabral (2005), the process of martitization results in a volume change when hematite replaces magnetite. From the cell volumes of magnetite (592.704Å) and hematite (301.279Å) and the number of Fe atoms within them (24 and 12 respectively), the calculated volume change increase is around 1.7% (Mucke & Cabral, 2005). This volume change results in expansion fractures throughout the replaced grains. Two theoretically reversible chemical reactions potentially occur for martitization: one is a redox reaction.

$$2\,Fe_3O_4 + 0.5\,O_{2\,(aq)} \rightarrow 3\,Fe_2O_3 \quad (1)$$

(Magnetite) (Hematite)

The other is a non-redox transformation under acidic conditions.

$$Fe_3O_4 + 2\,H^+_{(aq)} \rightarrow Fe_2O_3 + Fe^{2+}_{(aq)} + H_2O \quad (2)$$

(Magnetite) (Hematite) (Water)

(Ohmoto, 2003)

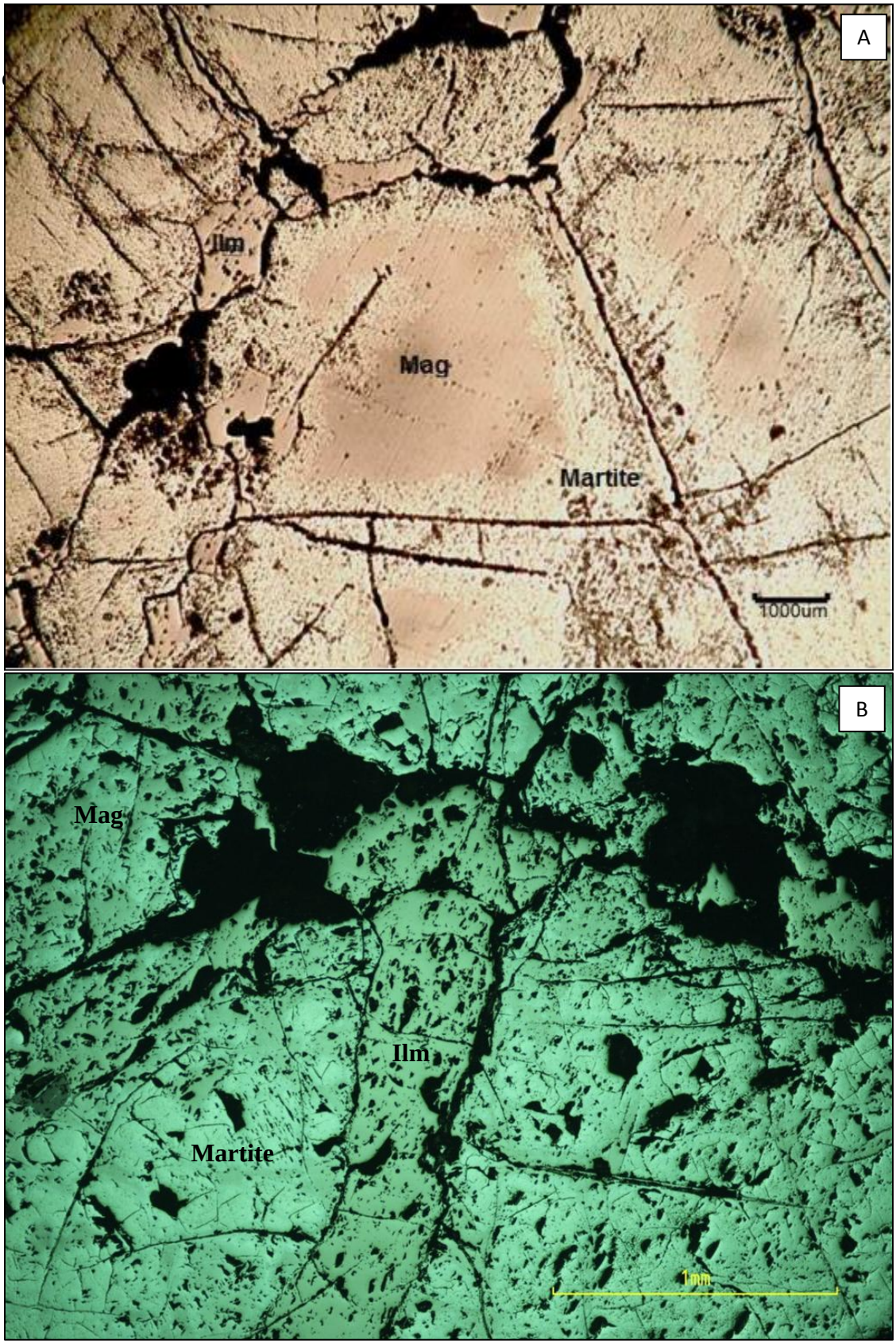

Figure 46. (A) A photomicrograph showing martitized magnetite (Mag) grains along grain boundaries. The core of the grain is unaltered (Mondal and Baidya, 2015). (B) A photomicrograph of the MP1 sample showing martitized regions along grain boundaries and fractures.

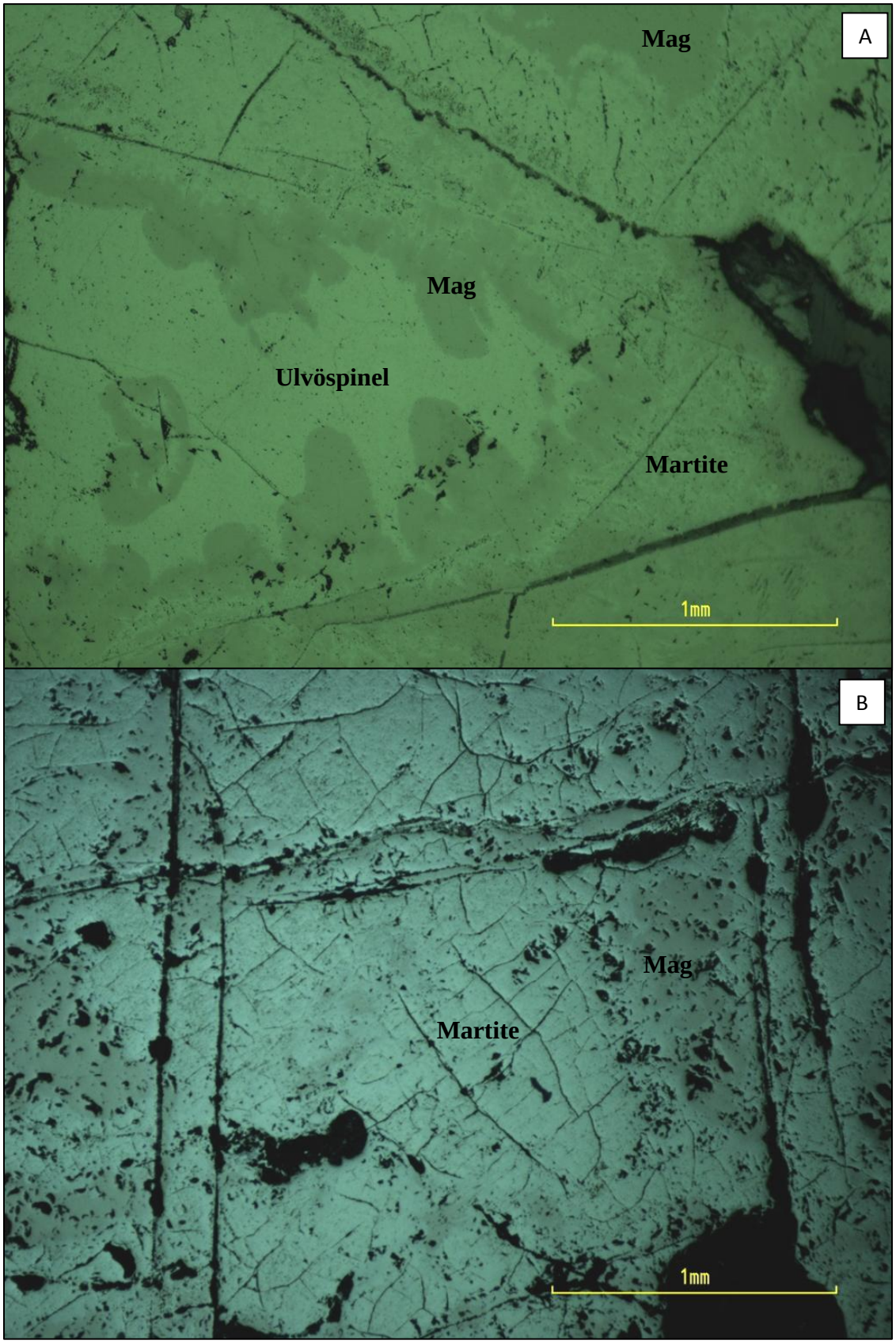

Figure 47. (A) A photomicrograph of the UZ8/17 sample showing extensive martitization with an ulvöspinel cloth-microtexture in the centre of the magnetite (Mag) grain. (B) A photomicrograph of the UZ21 sample showing martitization and extensive fracturing throughout the various magnetite (Mag) grains.

The magnetite grains are preferentially martitized along grain boundaries and octahedral planes {111} leaving unaltered cores except in few places where it is martitized throughout the grain. This martitization is a result of low-temperature oxidation. The difference in martitization is evident within Figure 47, where the UZ8/17 sample (47a) shows zones of martitization within a single grain and the UZ21 sample (47b) shows martitization throughout the grain. The centre of the UZ8/17 sample exhibits an ulvöspinel cloth-microtexture surrounded by magnetite and martite along the various grain boundaries, as seen within Figure 48 below.

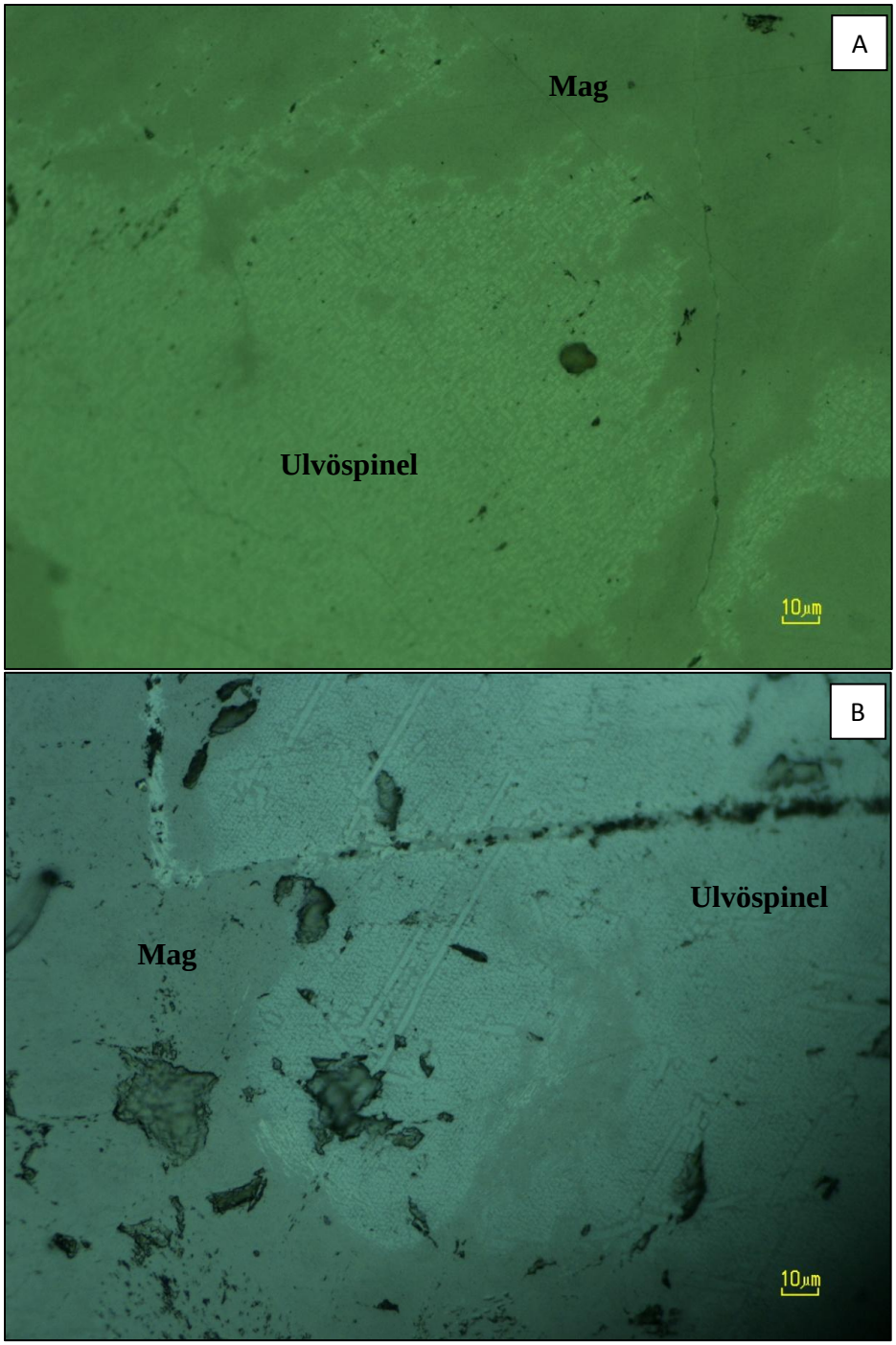

Figure 48. A photomicrograph of (A) the UZ8/17 and (B) UZ21 samples showing an ulvöspinel cloth-microtexture surrounded by martitized magnetite (Mag).

These images of the cloth-microstructure surrounded by martitized magnetite suggest that oxidation conditions shifted from ulvöspinel-favoured to martite-favoured conditions. The shift may be due to a temperature change, i.e. the sample cooled below the ulvöspinel window, thereby promoting martitization. Another possibility may be infilling of a Fe-Ti rich fluid, occurring within the various cooling fractures. The introduction of many veins and fracture infilling suggests that the respective samples underwent low-grade hydrothermal alteration, producing the martitized magnetite.

Syntaxial Veins

Syntaxial vein growth usually occurs when the vein-forming mineral is a major constituent of the host rock. Growth occurs along a single plane known as the median plane (Bons et al., 2012). Therefore, the youngest part of the vein forms along the median plane and the oldest part along the outside of the vein. Syntaxial veins may be symmetrical, but often growth occurs closer to one side of the vein, producing an asymmetry in the vein (Fisher and Brantley, 1992). Crystals within the syntaxial vein grow epitaxially off grains within the wall rock. Typically, growth within the vein occurs from both sides of the vein towards the centre, however, occasionally one finds that crystals only grew from one side towards the other (Fisher and Brantley, 1992). Syntaxial veins usually form from a single crack-seal event, which creates the space necessary for minerals to grow (Wilson, 1994). Vein-filling minerals usually precipitate onto the wall rock and grow inwards. As the crystals grow alongside each other in the same direction, the crystals become elongate in the growth direction. Different growth rates of individual crystals result in growth competition where some crystals grow faster than other crystals (Bons et al., 2012). The growth rate differentials result in a variation of elongate or blade-like crystals, with some crystals that narrow towards the growth direction and others widen. Ongoing nucleation of new crystals suppresses the elongate shape, and more equant grains fill the vein to produce a blocky texture. However, recrystallisation after vein formation tends to destroy the elongate blocky morphology of the vein crystals (Williams and Urai, 1989).

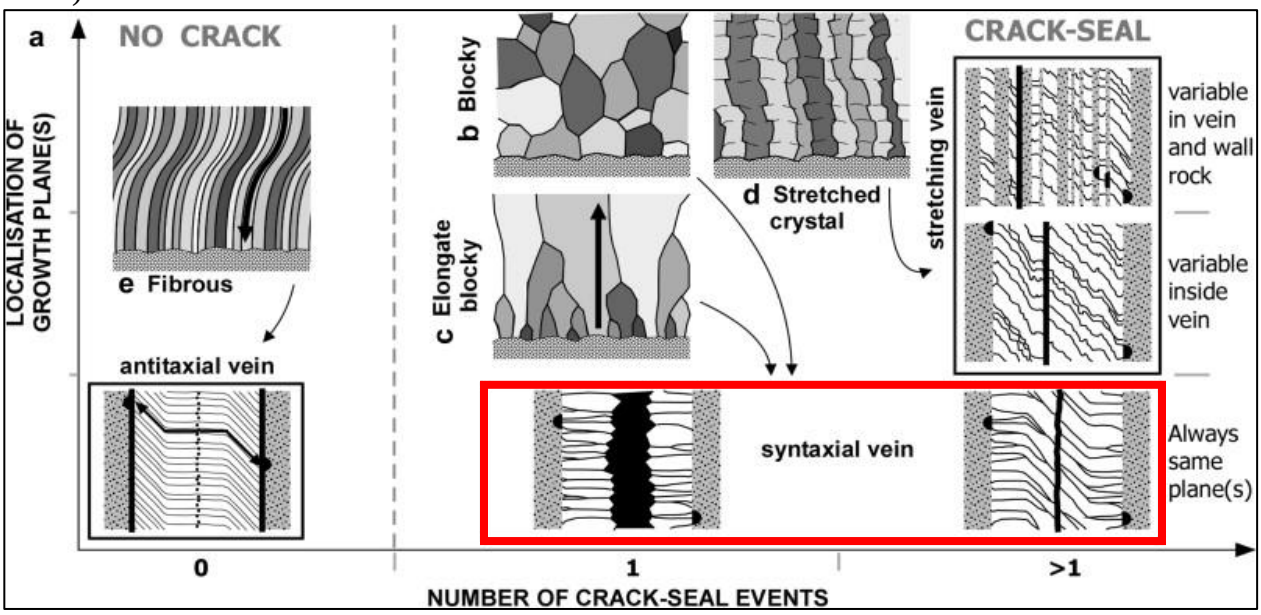

Figure 49. Image showing the various basic vein types and crystal morphology, as well as the number of crack-seal events (Bons et al., 2012). The red box highlights syntaxial veins, as they are the most common type found in this study.

Many of the samples within this study, such as MML1, MML2, MP1, UZ8/17 and UZ21B, exhibited syntaxial vein growth. Figure 50 below shows the variation from sample to sample, with some exhibiting symmetrical growth and others, asymmetrical growth. Some samples exhibit blocky crystals, and others exhibit blade-like crystal growth. This variation is a result of variation in growth rates as well as competition for space within the syntaxial vein.

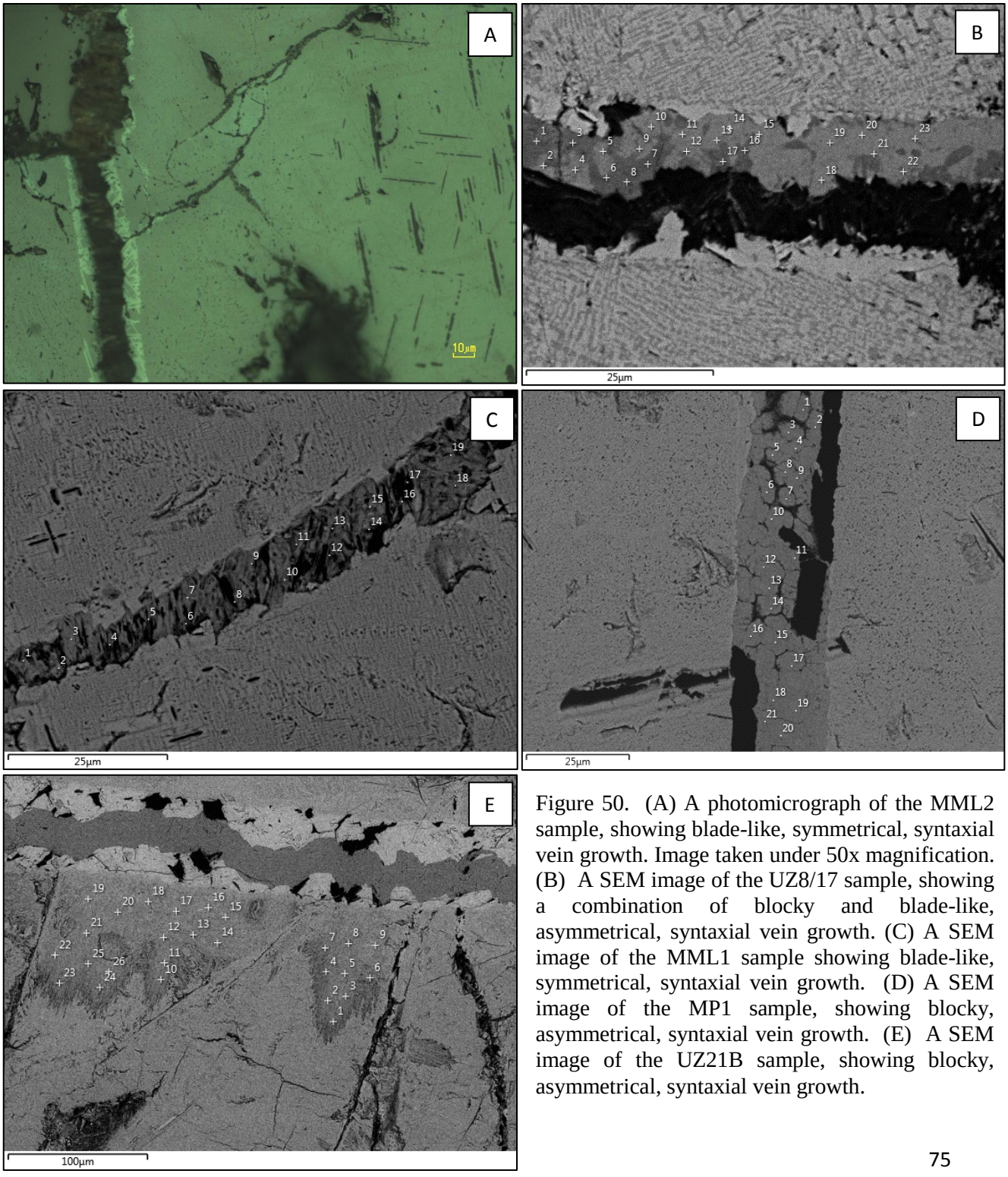

Figure 50. (A) A photomicrograph of the MML2 sample, showing blade-like, symmetrical, syntaxial vein growth. Image taken under 50x magnification. (B) A SEM image of the UZ8/17 sample, showing a combination of blocky and blade-like, asymmetrical, syntaxial vein growth. (C) A SEM image of the MML1 sample showing blade-like, symmetrical, syntaxial vein growth. (D) A SEM image of the MP1 sample, showing blocky, asymmetrical, syntaxial vein growth. (E) A SEM image of the UZ21B sample, showing blocky, asymmetrical, syntaxial vein growth.

Radial Fibrous Texture

During the analytical time on the SEM, a strange radiating, fibrous microtexture was identified. The microtexture appears to radiate outwards from single points along syntaxial veins. The microtexture consists of hundreds of individual fibrous needles with a composition similar to that of ulvöspinel within the UZ8/17 and UZ21B samples. However, no literature is available for this specific microtexture found within Fe-Ti oxide layers. Therefore, the name of this texture, as well as the formational conditions, is unknown.

The mean compositions of ulvöspinel and the fibrous microtexture vary slightly regarding Fe^{2+}, Fe^{3+}, Ti^{4+}, Al^{3+} and Mg^{2+} content. Ulvöspinel exhibits relatively higher enrichments of Fe^{2+} and Ti^{4+}, whereas the fibrous texture exhibits higher enrichments of Fe^{3+}, Al^{3+} and Mg^{2+}. The slightly higher Fe^{3+} content suggests that the fibrous texture underwent more oxidation than that of the ulvöspinel. The fact that the fibrous texture grows adjacent to the syntaxial veins suggests that growth is associated with that of the vein. Assuming conditions relate to that of the vein, relatively low temperatures and oxidising conditions occurred during the time of the fibrous microtexture growth. The only samples this texture occurs within, UZ8/17 and UZ21B are samples that underwent martitization of the magnetite. Martitization may also be a contributing factor to this fibrous microtexture development. Figure 51 and 52 below shows the extensive, fibrous microtexture development within the UZ21B sample.

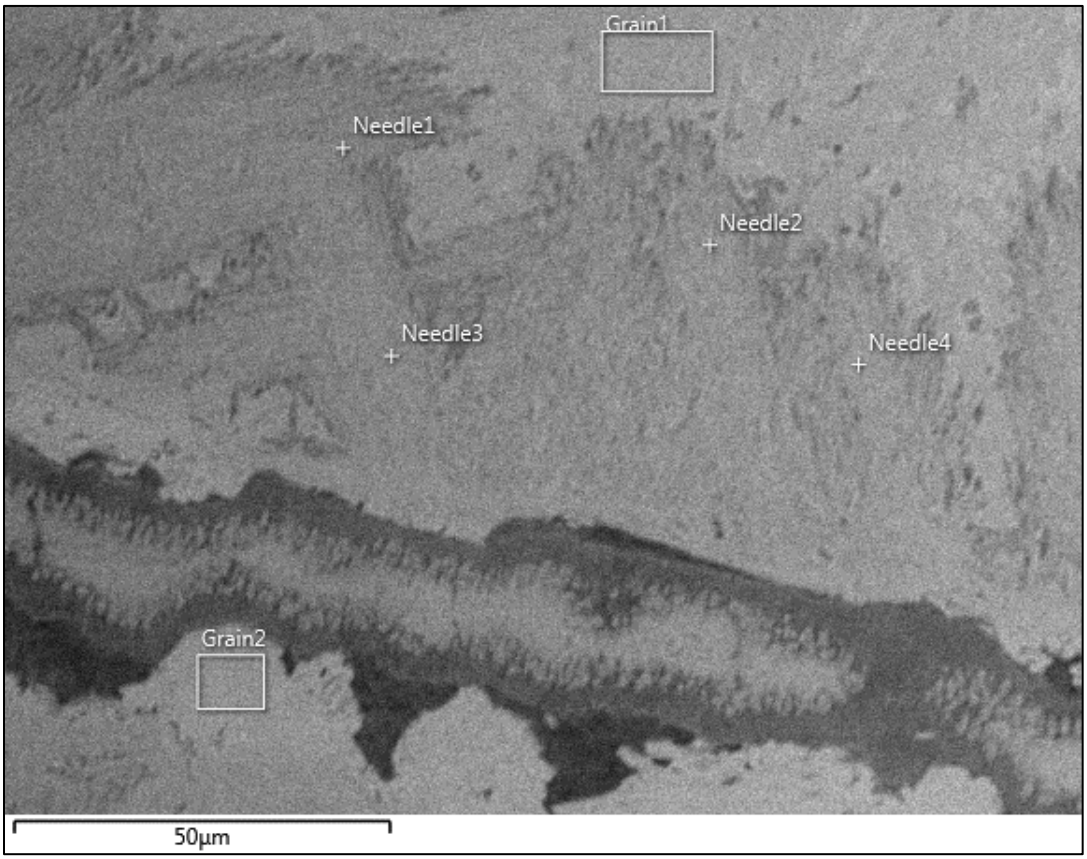

Figure 51. A SEM image showing the extensive fibrous microtexture development, adjacent to a blade-like syntaxial vein. The fibrous needles appear to radiate outwards from central points.

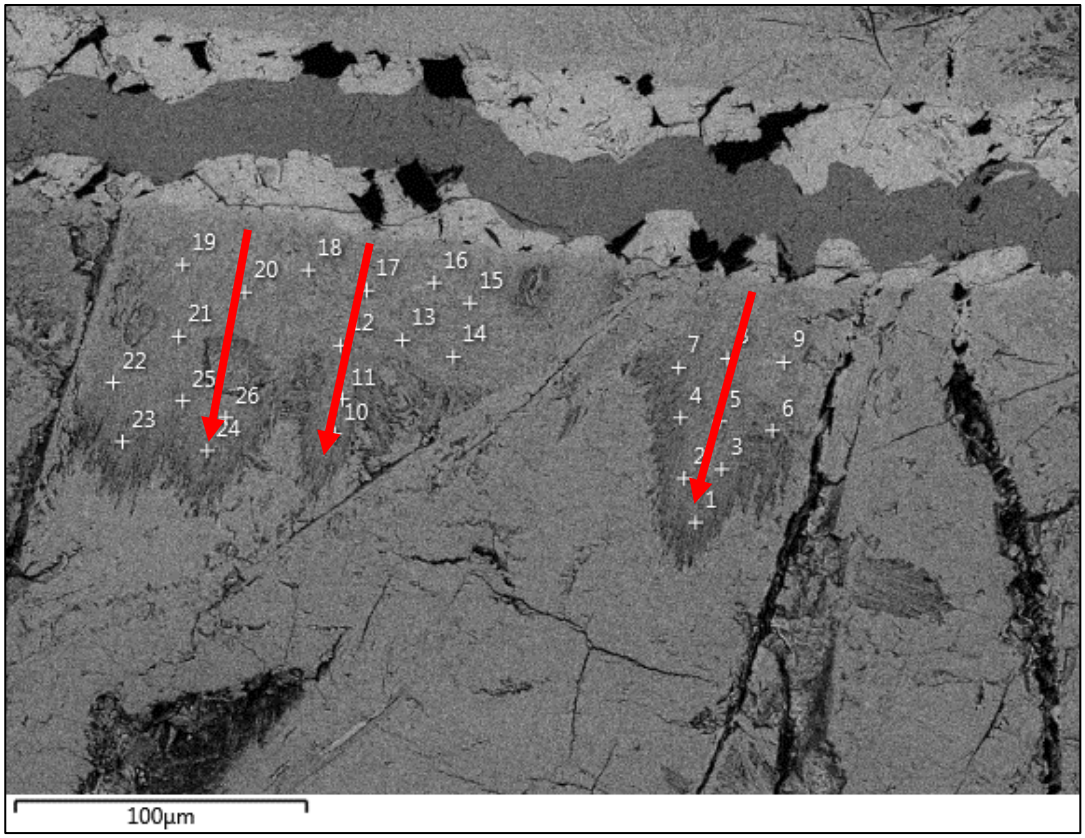

Figure 52. A SEM image of the UZ21B sample showing the radiating fibrous microtexture adjacent to a blocky, syntaxial vein. The radiation of the fibrous needles is more evident within this image. The red arrows sow growth direction.

Figure 53. Image showing fibrous hedenbergite crystals found in a skarn deposit from Campiglia Marittima, Italy. Field of view = 7mm (Strekeisen, 2007). The red lines outline a single generation of fibrous radiating crystals.

Acicular, in mineralogy, refers to a crystal habit composed of slender, needle-like crystals that may or may not radiate from a central point. Acicular crystals differ from fibrous crystals in their thickness. Crystals with a fibrous habit are much thinner, sometimes to the point of being flexible like hair, while acicular crystals are thicker and more rigid. The microtexture seen in the UZ8/17 and UZ21B samples fit the description of fibrous rather than acicular as they tender to show curvature towards the ends as seen in Figure 54 below. A radiating fibrous texture will grow outwards from a central 'seed' point as evidenced by Figure 52 above. Figure 51 shows fibrous hedenbergite crystals, which exhibit the same texture as the pseudo-ulvöspinel crystals seen in this study. The pattern overlaps just like that seen within this study. The only visible difference in the two textures (hedenbergite and pseudo-ulvöspinel) is an obvious size variation. The texture identified within the oxides is orders of magnitude smaller than that of the hedenbergite. Factors influencing a crystal's habit include a combination of two or more crystal forms, trace impurities present during growth, crystal twinning and growth conditions (heat, pressure, space) and specific growth tendencies like growth striations.

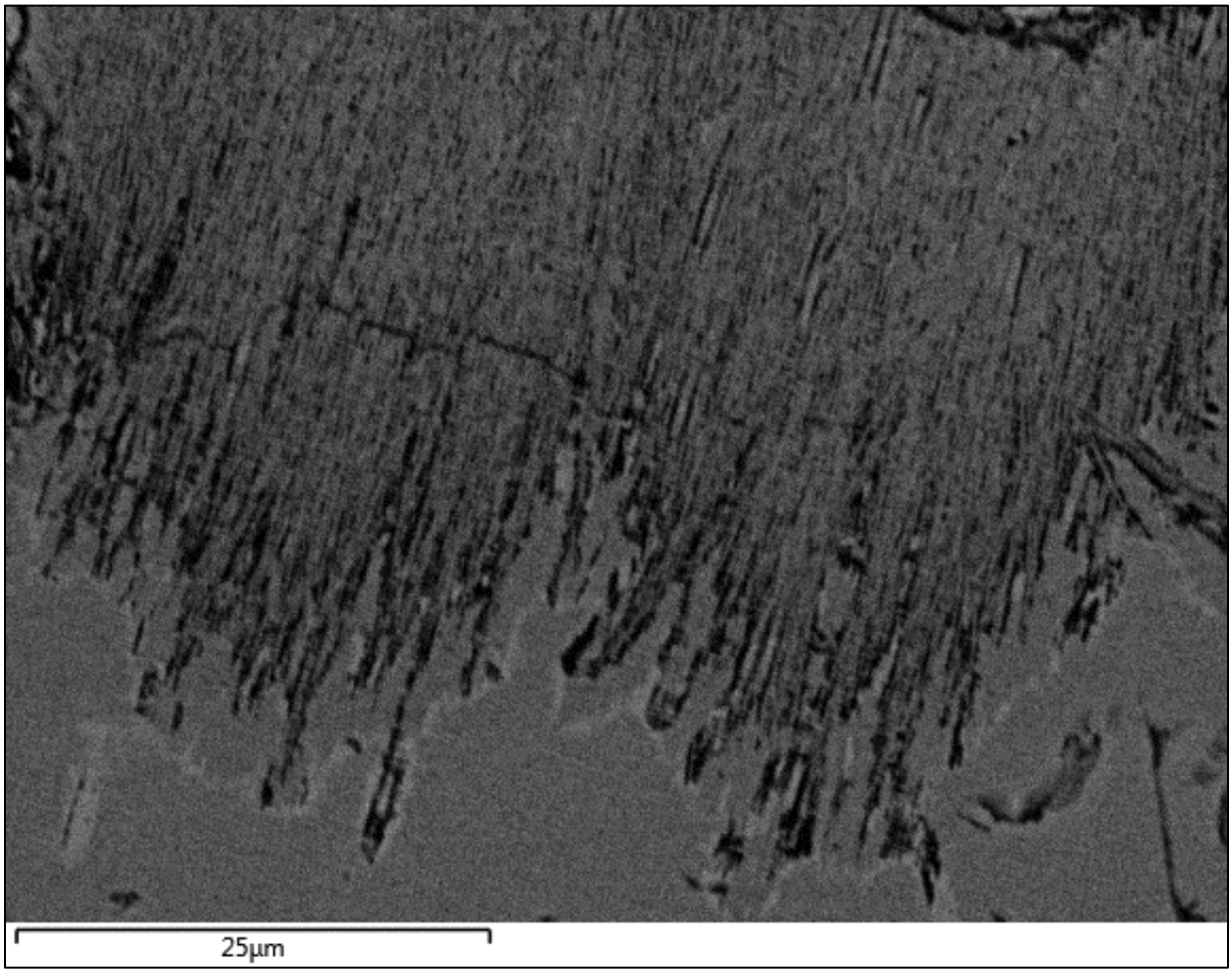

Figure 54. A SEM image of the UZ21B sample showing a close up of the fibrous crystal growth. Note the curvature towards the end of the individual crystals.

Microstructures – A Possible Formational Model

Placing strain on a mineral's crystal lattice is predominantly achieved through changes in pressure and temperature. Increases in temperatures allow for the movement of larger ions, typically between 15-30% larger, into the crystal lattice, occupying sites normally occupied by smaller ions. As conditions (pressure and temperature) change, ions that no longer fit into the spaces they occupy, place a strain on the lattice itself. As a reaction to strain, the minerals composition shifts (larger ions replaced by smaller ions) to relieve the strain. The system responds in various ways, with a single possible response resulting in the elements in a crystal moving from one chemical site to another via intra-crystalline diffusion (Otto, 2016).

According to Petrischeva and Abart (2012), exsolution is the subsequent separation of an initially homogenous solid solution into two distinct minerals without changing the bulk chemistry of the system. Titaniferous-magnetite exsolution generally occurs as spinodal decomposition, although other possibilities include nucleation, cellular decomposition or continuous decomposition (Yund and McAllister, 1970). The exsolution microstructures coarsen, and the volume of the magnetite-rich regions increase, with their shape changing from cubic to plate-like (Price, 1980). The mechanism of exsolution for ilmenite is reported as an oxidative reaction from the originally homogenous magnetite as seen previously in reaction 1. When the reaction essentially reaches equilibrium, the ilmenite component no longer leaves the titaniferous-magnetite grain, presenting ilmenite as internal granular exsolution seen within the microstructures. According to Mogensen (1946), a two-phase intergrowth of magnetite-rich and ulvöspinel-rich oxides exist. Further studies noted that titaniferous-magnetite exsolution is a common feature in rocks occurring in plutonic and hyperbassal environments (Otto, 2016).

According to Cawthorn and Walraven (1998), the Bushveld Igneous Complex emplacement occurred through a series of magma pulses, the last of which occurred after the Pyroxenite Marker formed, at an estimated temperature of 1150ºC. This suggests an initially high temperature within the Upper Zone, with a constant drop in temperature due to the lack of further injections of magma. As mentioned previously titaniferous-magnetite forms a solid solution between ulvöspinel and magnetite, but this is only present at high temperatures. Therefore, the pulse of magma into the Upper Zone consists of the bulk composition, later differentiated into the various layers. Moreover, long periods of Fe-Ti enrichment are required within the system before precipitation of magnetite can occur. Achieving the required level of enrichment occurs through the process of magma differentiation as according to Reynolds (1985b). Various conditions such as changes in pressure, temperature, and a decrease in oxygen fugacity during crystallisation, affect magma differentiation. The unmixing of ilmenite from the titaniferous magnetite occurs through spinodal decomposition as a mechanism of exsolution. Spinodal decomposition depends on various factors such as temperature as well as the cooling rate of the magma and occurs due to a rapid loss of temperature, even if the initial temperature is very high. The spinodal decomposition mechanism is limited to the field within the chemical spinodal. Spinodal decomposition is thus limited to oxides where the compositions are near the centre of the ulvöspinel-magnetite solid solution as seen throughout the results of the various samples within this study.

Considering the above, this would suggest the following for the formation of the magnetite layers, and their microstructures: (1) Pulses of Fe-Ti rich magmas occur, injecting large amounts of liquid into the Upper Zone. Dense immiscible droplets form and settle out of suspension, accumulating and forming stratified layers. An initial temperature of the liquid is approximately 1150ºC. (2) Upon cooling, titaniferous-magnetite precipitation occurs at around 865ºC, with low oxygen fugacity across the chamber. At this stage, ilmenite is not abundant, due to the presence of Ti as a component of ulvöspinel at high temperatures, rather than ilmenite. (3) At some point during cooling of the solid solution, spinodal decomposition occurs. This starts to produce ulvöspinel lamellae within magnetite grains. At the same time, the stratified layers begin to oxidise, forming ilmenite as a product of ulvöspinel decomposition. (4) External granular diffusion results in ilmenite constituents diffusing across the grain boundary. When the rates of diffusion decrease, the ilmenite cannot leave the titaniferous-magnetite grain and exsolve. Ilmenite is dependent on the ulvöspinel content, which in turn is dependent on the temperature and oxygen fugacity during cooling. This would indicate why some polished sections showed ilmenite exsolution while others do not. (5) The layers cool to a point where spinodal decomposition is no longer favoured and the system shifts from cloth-texture exsolution to trellis-exsolution. The ilmenite component begins to form thin, multi-directional lenses often surrounded by box structures. (6) During oxidation, some magnetite subjected to martitization is subsequently replaced by martite. The replacement involves expansion and fracturing of martitized grains. During expansion, syntaxial veins form along grain boundaries, subsequently filled by surrounding Fe-Ti liquid. Depending on the growth rate of the crystals within the vein, either blocky syntaxial veins or blade-like syntaxial veins form. (7) During continued cooling, annealing of euhedral magnetite grains occurs. The annealing process runs concurrently with other processes occurring within the magnetite layers.

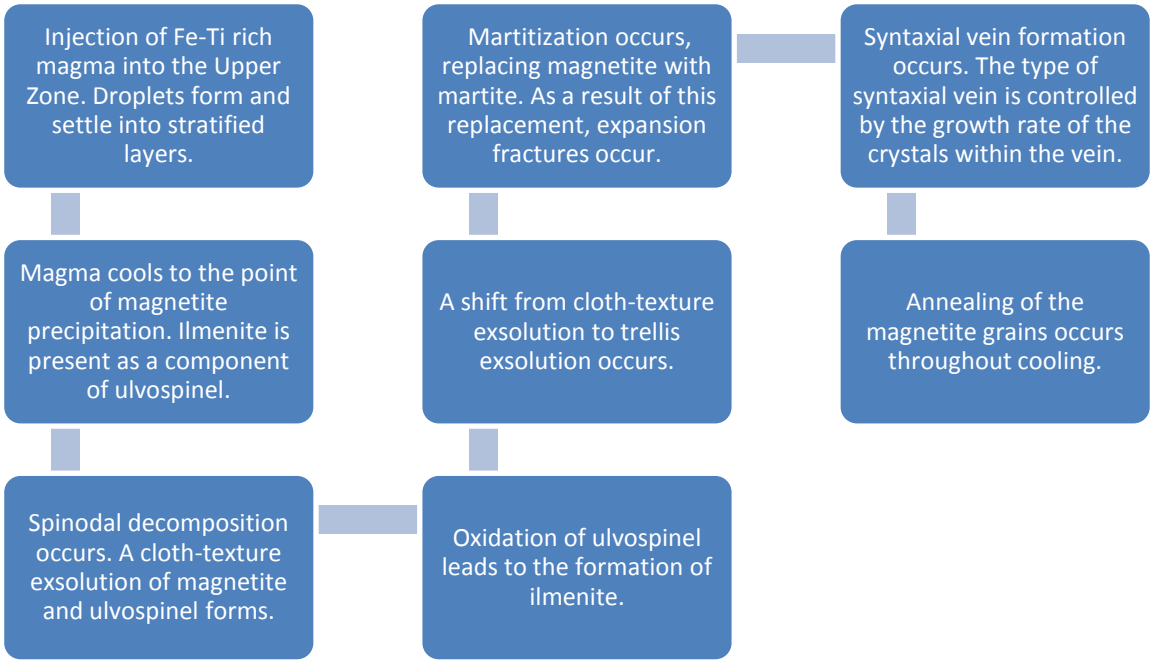

Figure 55. A flow chart showing the expected processes over time in the formation of the magnetite layers and their respective microstructures.

Chapter 6: Summary and Conclusion

The purpose of this study was to gain an insight into the formational conditions present during the formation of the various sampled magnetite layers and their respective microstructures. The primary focus was on the Upper Zone magnetite within the eastern limb of the Bushveld Igneous Complex. Comparisons of the investigated results showed the relevance of investigating exsolution textures, especially those seen within the titaniferous-magnetites. The collected qualitative data, SEM images, and photomicrographs contributed to building a suggestive model and providing evidence for the presented and discussed topics throughout this dissertation.

Upon investigation, the various magnetite samples showed varying degrees and types of textures as well as evidence of secondary processes. All of the magnetite samples showed evidence of the cloth-texture exsolution. Samples MML1, MML2 and MP1 exhibited the spinel trellis-exsolution texture, whereas samples UZ8/17, UZ21 and UZ21B showed the unknown fibrous texture. All samples showed syntaxial veins with varying types of crystallisation, variations between blocky- and blade-like crystal growths. Martitization occurred within the MP1, UZ8/17 and UZ21 samples. All samples showed varying degrees of oxidation, related to the ternary diagrams for each sample, the degree of which determined the extent of the texture formation.

Intergrowths of ilmenite occur within magnetite and exist between two extremes, which include the cloth microtexture and the trellis microtexture (with a "sandwich" variant). The cloth intergrowth is also characteristic of the ulvöspinel exsolutions in the magnetite. These lamellae usually lie on {100}, with inter-lamellar magnetite-rich blocks. The exsolution microstructure only develops on a small scale, due to the slow rate of the kinetic processes involved in unmixing at the solvus temperature. Within the ulvöspinel cloth microtexture, it is the coarse {100} lamellae pattern which gives the grain the appearance of cloth. The {100} lamellae of the cloth microtexture generated by exsolution of ulvöspinel occur at a temperature below the magnetite-ulvöspinel solvus. The ulvöspinel completely transforms into ilmenite micro-lamellae through in situ oxidation. Different modes of oxidation of ulvöspinel may account for the diversity of the microtextures observed.

Martitization occurs under moderate-temperature, hydrothermal oxidation, resulting in a volume change when hematite replaces magnetite. The calculated volume change increase is around 1.7%; this volume change results in expansion fractures throughout the replaced grains. The magnetite grains are preferentially martitized along grain boundaries and octahedral planes {111} leaving unaltered cores except in few places where it is martitized throughout the grain. The shift may be due to a temperature change, i.e. the sample cooled below the ulvöspinel window, thereby promoting martitization. Another possibility may be infilling of a Fe-Ti rich fluid, occurring within the various cooling fractures. The introduction of many veins and fracture infilling suggests that the respective samples underwent low-grade hydrothermal alteration, producing the martitized magnetite.

The resulting formational model involves: (1) Pulses of Fe-Ti rich magmas occur, injecting large amounts of liquid into the Upper Zone. Dense immiscible droplets form and settle out of suspension, accumulating and forming stratified layers. An initial temperature of the liquid is approximately 1150ºC. (2) Upon cooling, titaniferous-magnetite precipitation

occurs at around 865ºC, with low oxygen fugacity across the chamber. At this stage, ilmenite is not abundant, due to the presence of Ti as a component of ulvöspinel at high temperatures, rather than ilmenite. (3) At some point during cooling of the solid solution, spinodal decomposition occurs. This starts to produce ulvöspinel lamellae within magnetite grains. At the same time, the stratified layers begin to oxidise, forming ilmenite as a product of ulvöspinel decomposition. (4) External granular diffusion results in ilmenite constituents diffusing across the grain boundary. When the rates of diffusion decrease, the ilmenite cannot leave the titaniferous-magnetite grain and exsolve. Ilmenite is dependent on the ulvöspinel content, which in turn is dependent on the temperature and oxygen fugacity during cooling. This would indicate why some polished sections showed ilmenite exsolution while others do not. (5) The layers cool to a point where spinodal decomposition is no longer favoured and the system shifts from cloth-texture exsolution to trellis-exsolution. The ilmenite component begins to form thin, multi-directional lenses often surrounded by box structures. (6) During oxidation, some magnetite subjected to martitization is subsequently replaced by martite. The replacement involves expansion and fracturing of martitized grains. During expansion, syntaxial veins form along grain boundaries, subsequently filled by surrounding Fe-Ti liquid. Depending on the growth rate of the crystals within the vein, either blocky syntaxial veins or blade-like syntaxial veins form. (7) During continued cooling, annealing of euhedral magnetite grains occurs. The annealing process runs concurrently with other processes occurring within the magnetite layers.

Possible advancements in this study could include the use of the microprobe. Microprobe data would provide a clearer indication of the phases present and their respective compositions. This would assist in determining the origin of the fibrous texture. Although useful, the qualitative data acquired in this study merely indicated possible phases with low accuracy. The data is an amalgamation of multiple phases depending on the size of the texture used in point analysis. To achieve a greater understanding of the unknown fibrous texture and possible formational conditions, further research is required.

References

ANDERSON, A. 1968. Oxidation of the LaBlache Lake titaniferous magnetite deposit, Quebec. *The Journal of Geology,* 76**,** 528-547.

ATKINS, F. 1969. Pyroxenes of the Bushveld intrusion, South Africa. *Journal of Petrology,* 10**,** 222-249.

BASTA, E. Z., 1960. — Natural and synthetic titanomagnetites (the system Ee3O4-Fe2TiO4-FeTiO3). N. Jb. Min. Abh., 94, 1017-1048

BONS, P. D., ELBURG, M. A. & GOMEZ-RIVAS, E. 2012. A review of the formation of tectonic veins and their microstructures. *Journal of Structural Geology,* 43**,** 33-62.

BUDDINGTON, A. & LINDSLEY, D. 1964. Iron-titanium oxide minerals and synthetic equivalents. *Journal of Petrology,* 5**,** 310-357.

BUICK, I. S., MAAS, R. & GIBSON, R. 2001. Precise U–Pb titanite age constraints on the emplacement of the Bushveld Complex, South Africa. *Journal of the Geological Society,* 158**,** 3-6.

BUTCHER, A. R. & MERKLE, R. K. 1987. Postcumulus modification of magnetite grains in the upper zone of the Bushveld Complex, South Africa. *Lithos,* 20**,** 247-260.

CAWTHORN, R. G. & ASHWAL, L. D. 2009. Origin of anorthosite and magnetitite layers in the Bushveld Complex, constrained by major element compositions of plagioclase. *Journal of Petrology,* 50**,** 1607-1637.

CAWTHORN, R. G. & MCCARTHY, T. 1980. Variations in Cr content of magnetite from the Upper Zone of the Bushveld Complex—evidence for heterogeneity and convection currents in magma chambers. *Earth and Planetary Science Letters,* 46**,** 335-343.

CAWTHORN, R. G. & WALRAVEN, F. 1998. Emplacement and crystallisation time for the Bushveld Complex. *Journal of Petrology,* 39**,** 1669-1687.

CAWTHORN, R. & WEBB, S. 2001. Connectivity between the western and eastern limbs of the Bushveld Complex. *Tectonophysics,* 330**,** 195-209.

CLARKE, B., UKEN, R. & REINHARDT, J. 2009. Structural and compositional constraints on the emplacement of the Bushveld Complex, South Africa. *Lithos,* 111**,** 21-36.

DARE, S. A., BARNES, S.-J., BEAUDOIN, G., MÉRIC, J., BOUTROY, E. & POTVIN-DOUCET, C. 2014. Trace elements in magnetite as petrogenetic indicators. *Mineralium Deposita,* 49**,** 785-796.

DUCHESNE, J.-C. 1970. Microtextures of Fe-Ti oxide minerals in the South-Rogaland anorthositic complex (Norway). *Annales de la Société Géologique de Belgique,* 935**,** 527-544.

FISHER, D.M., BRANTLEY, S.L., EVERETT, M., DZVONIK, J., 1995. Cyclic fluid-flow through a regionally extensive fracture network within the Kodiak accretionary prism. *Journal of Geophysical Research-Solid Earth* 100 (B7), 12881e12894.

HARNEY, D. M. & VON GRUENEWALDT, G. 1995. Ore-forming processes in the upper part of the Bushveld complex, South Africa. *Journal of African Earth Sciences,* 20**,** 77-89.

HARNEY, D., VON GRUENEWALDT, G. & MERKLE, R. 1996. The use of plagioclase composition as an indicator of magmatic processes in the Upper Zone of the Bushveld Complex. *Mineralogy and Petrology,* 56**,** 91-103.

HOFFMAN, J. W. & DE BEER, F. Characteristics of the micro-focus X-ray tomography facility (MIXRAD) at Necsa in South Africa. 18th World Conference on Nondestructive Testing, 2012. 16-20.

KRUGER, F., CAWTHORN, R. & WALSH, K. 1987. Strontium isotopic evidence against magma addition in the Upper Zone of the Bushveld Complex. *Earth and Planetary Science Letters,* 84**,** 51-58.

LINDSLEY, D. H., 1962. — Investigations in the system FeO-Fe2O3-TiO2. Yb. Carnegie Instn. Wash., 61, 100-106

MATHEZ, E., VANTONGEREN, J. & SCHWEITZER, J. 2013. On the relationships between the Bushveld Complex and its felsic roof rocks, part 1: petrogenesis of Rooiberg and related felsites. *Contributions to Mineralogy and Petrology,* 166**,** 435-449.

MAILA, R. P. 2015. *Geochemistry of magnetite layers in the upper zone of the Bushveld Complex, South Africa.*

MOLYNEUX, T. 1974. A geological investigation of the Bushveld Complex in Sekhukhuneland and part of the Steelpoort valley. *South African Journal of Geology,* 77**,** 329-338.

MONDAL, R. & BAIDYA, T. K. 2015. Titaniferous Magnetite Deposits Associated with Archean Greenstone Belt in the East Indian Sheild. *Earth,* 4**,** 15-30.

MÜCKE, A. & CABRAL, A. R. 2005. Redox and non-redox reactions of magnetite and hematite in rocks. *Chemie der Erde-Geochemistry,* 65**,** 271-278.

OHMOTO, H. 2003. Nonredox transformations of magnetite-hematite in hydrothermal systems. *Economic Geology,* 98**,** 157-161.

OTTO, T. 2016. Texture development in titaniferous magnetites found in Layer 21 in the Bushveld Igneous Complex, South Africa. University of Pretoria.

PEARCE, C. I., HENDERSON, C. M. B., TELLING, N. D., PATTRICK, R. A., CHARNOCK, J. M., COKER, V. S., ARENHOLZ, E., TUNA, F. & VAN DER LAAN, G. 2010. Fe site occupancy in magnetite-ulvospinel solid solutions: A new approach using X-ray magnetic circular dichroism. *American Mineralogist,* 95**,** 425-439.

PETRISHCHEVA, E. & ABART, R. 2012. Exsolution by spinodal decomposition in multicomponent mineral solutions. 60**,** 5481-5493.

PRICE, G. D. 1980. Exsolution microstructures in titanomagnetites, and their magnetic significance. *Physics of the Earth Planetary Interiors* 23, pp 2-12.

RAMDOHR, P. 1953. Ulvöspinel and its significance in titaniferous iron ores. *Economic Geology,* 48**,** 677-688.

REYNOLDS, I. M. 1985a. The nature and origin of titaniferous magnetite-rich layers in the upper zone of the Bushveld Complex; a review and synthesis. *Economic Geology,* 80**,** 1089-1108.

REYNOLDS, I. M. 1985b. Contrasted mineralogy and textural relationships in the uppermost titaniferous magnetite layers of the Bushveld Complex in the Bierkraal area north of Rustenburg. *Economic Geology,* 80**,** 1027-1048.

SCOON, R. N. & MITCHELL, A. A. 1994. Discordant iron-rich ultramafic pegmatites in the Bushveld Complex and their relationship to iron-rich intercumulus and residual liquids. *Journal of Petrology,* 35**,** 881-917.

SCOON, R. & MITCHELL, A. 2012. The Upper Zone of the Bushveld Complex at Roossenekal, South Africa: geochemical stratigraphy and evidence of multiple episodes of magma replenishment. *South African Journal of Geology,* 115**,** 515-534.

STRECKEISEN, A. L. The IUGS systematics of igneous rocks. Jour. Geol. Soc. Lond. V, 1991. Citeseer.

TEGNER, C., CAWTHORN, R. G. & KRUGER, F. J. 2006. Cyclicity in the Main and Upper Zones of the Bushveld Complex, South Africa: crystallisation from a zoned magma sheet. *Journal of Petrology,* 47**,** 2257-2279.

VON GRUENEWALDT, G. 1973. The main and upper zones of the Bushveld Complex in the Roossenekal area, eastern Transvaal. *Transactions of the Geological Society of South Africa,* 76**,** 207-227.

VON GRUENEWALDT, G., KLEMM, D., HENCKEL, J. & DEHM, R. 1985. Exsolution features in titanomagnetites from massive magnetite layers and their host rocks of the Upper Zone, Eastern Bushveld Complex. *Economic Geology,* 80**,** 1049-1061.

VANTONGEREN, J. & MATHEZ, E. 2013. Incoming magma composition and style of recharge below the Pyroxenite Marker, Eastern Bushveld Complex, South Africa. *Journal of Petrology,* 54**,** 1585-1605.

VANTONGEREN, J. A., MATHEZ, E. A. & KELEMEN, P. B. 2010. A felsic end to Bushveld differentiation. *Journal of Petrology,* 51**,** 1891-1912.

VANTONGEREN, J., ZIRAKPARVAR, N. & MATHEZ, E. 2016. Hf isotopic evidence for a cogenetic magma source for the Bushveld Complex and associated felsic magmas. *Lithos,* 248**,** 469-477.

VERHOOGEN, J., 1962. — Oxidation of iron-titanium oxides in igneous rocks. J. Geol., 70, 168-181.

VINCENT, E., WRIGHT, J., CHEVALLIER, R. & MATHIEU, S. 1957. Heating experiments on some natural titaniferous magnetites. *Mineral. Mag,* 31**,** 624-655.

VOORDOUW, R., GUTZMER, J. & BEUKES, N. J. 2009. Intrusive origin for upper group (UG1, UG2) stratiform chromitite seams in the Dwars River area, Bushveld Complex, South Africa. *Mineralogy and Petrology,* 97**,** 75.

WALRAVEN, F. 1997. *Geochronology of the Rooiberg Group, Transvaal Supergroup, South Africa*, Economic Geology Research Unit, University of the Witwatersrand.

WILLEMSE, J. 1969. The vanadiferous magnetic iron ore of the Bushveld Igneous Complex. *Econ Geol Monogr,* 4**,** 137-208.

WILLIAMS, P.F., URAI, J.L., 1989. Curved vein fibres: an alternative explanation. Tectonophysics 158, 311-333.

WILSON, C.J.L., 1994. Crystal growth during a single-stage opening event and its implications for syntectonic veins. *Journal of Structural Geology* 16, 1283-1296.

YUND, R. A. & MCCALLISTER, R. H. 1970. Kinetics and mechanisms of exsolution. *Chemical Geology,* 6, 5-30.

ZHANG, X.-Q., SONG, X.-Y., CHEN, L.-M., XIE, W., YU, S.-Y., ZHENG, W.-Q., DENG, Y.-F., ZHANG, J.-F. & GUI, S.-G. 2012. Fractional crystallization and the formation of thick Fe–Ti–V oxide layers in the Baima layered intrusion, SW China. *Ore Geology Reviews,* 49**,** 96-108.

Appendix A: Sample Locations

Sample	Latitude	Longitude
Magnetite Plug (MP-1)	25° 12' 54.18" S	29° 56' 14.71" E
Main Magnetite Layer (MML1 and MML2) – 30m apart	24° 52' 09.18" S	29° 58' 35.50" E
Layer 8 (UZ8/17)	25° 06' 00.23" S	29° 50' 14.42" E
Layer 21 North of Steelpoort Fault (UZ-15)	24° 48' 31.03" S	29° 56' 52.96" E
Layer 21 South of Steelpoort Fault (UZ21B)	25° 10' 01.57" S	29° 49' 22.86" E

Appendix B: Data Analyses